

การปลูกผลึกควอนตัมคือตโมเลกุลชนิดแบบจัดเรียงตัวเอง  
ด้วยการปลูกผลึกแบบลำโมเลกุลและศักยภาพในการประยุกต์



นางสาวสุวารี สุรประภาพิชย์

สถาบันวิทยบริการ

วิทยานิพนธ์นี้เป็นส่วนหนึ่งของการศึกษาตามหลักสูตรปริญญาวิศวกรรมศาสตรดุษฎีบัณฑิต

สาขาวิชาวิศวกรรมไฟฟ้า ภาควิชาวิศวกรรมไฟฟ้า

คณะวิศวกรรมศาสตร์ จุฬาลงกรณ์มหาวิทยาลัย

ปีการศึกษา 2549

ลิขสิทธิ์ของจุฬาลงกรณ์มหาวิทยาลัย

SELF-ASSEMBLED QUANTUM DOT MOLECULES BY  
MOLECULAR BEAM EPITAXY AND THEIR POTENTIAL  
APPLICATIONS



Miss Suwaree Suraprapapich

สถาบันวิทยบริการ  
จุฬาลงกรณ์มหาวิทยาลัย

A Dissertation Submitted in Partial Fulfillment of the Requirements  
for the Degree of Doctor of Philosophy Program in Electrical Engineering

Department of Electrical Engineering

Faculty of Engineering

Chulalongkorn University

Academic year 2006

Copyright of Chulalongkorn University

Thesis Title                    SELF-ASSEMBLED QUANTUM DOT MOLECULES  
   BY MOLECULAR BEAM EPITAXY AND THEIR  
   POTENTIAL APPLICATIONS

By                                    Miss Suwaree Suraprapapich

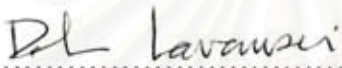
Field of Study                  Electrical Engineering

Thesis Advisor                Professor Somsak Panyakeow, D.Eng.

Thesis Co-advisor            Professor Charles W. Tu, Ph.D.

---


Accepted by the Faculty of Engineering, Chulalongkorn University in  
Partial Fulfillment of the Requirements for the Doctoral Degree

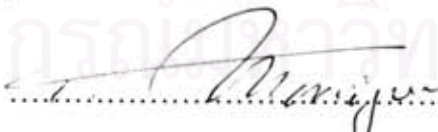
  
..... Dean of the Faculty of Engineering  
( Professor Direk Lavansiri, Ph.D. )


THESIS COMMITTEE

  
..... Chairman  
( Professor Virulh Sa-yakanit , Ph.D. )

  
..... Thesis Advisor  
( Professor Somsak Panyakeow , D.Eng. )

  
..... Thesis Co-advisor  
( Professor Charles W. Tu , Ph.D. )

  
..... Member  
( Professor Toyosaka Morizumi, D.Eng )

  
..... Member  
( Associate Professor Montri Sawadsaringkarn , D.Ing. )

ศุวารี สุรประภาพิชัย : การปลูกผลึกควอนตัมคือดโมเลกุลชนิดแบบจัดเรียงตัวเองด้วยการปลูกผลึกแบบ  
 ลำโมเลกุลและศึกษาภาพในการประยุกต์. (SELF-ASSEMBLED QUANTUM DOT MOLECULES BY  
 MOLECULAR BEAM EPITAXY AND THEIR POTENTIAL APPLICATIONS) อ. ที่ปรึกษา : ศ.ดร.  
 สมศักดิ์ ปัญญาแก้ว, อ. ที่ปรึกษาร่วม Prof. Charles W. Tu, 131 หน้า.

วัตถุประสงค์หลักของวิทยานิพนธ์นี้คือ เพื่อศึกษากลไกการเกิดผลึกโครงสร้างในระดับนาโนเมตร  
 โดยเฉพาะจะเน้นเรื่องโครงสร้างควอนตัมคือดโมเลกุล ด้วยการใช้เครื่องปลูกผลึกแบบลำโมเลกุล 2 ชนิดที่มี  
 ความแตกต่างกันที่ชนิดของอาร์เซนิกที่ใช้ ซึ่งมีทั้งชนิดของแข็ง และ ก๊าซ โดยใช้เทคนิคการปลูกแบบการปลูก  
 กลบคือดแบบบางๆด้วยชั้นแกเลียมอาร์เซไนด์แล้วทำการปลูกชั้นอินเดียมอาร์เซไนด์ควอนตัมคือดทับซ้ำอีก  
 รอบ วิธีวิเคราะห์ตัวอย่างชิ้นงานในการทดลองได้แก่ การวัดด้วยแรงอะตอม (Atomic Force Microscopy) และ  
 การวัดโฟโตลูมิเนสเซนซ์ (Photoluminescence)

เมื่อพิจารณาตัวอย่างชิ้นงานที่ปลูกด้วยเครื่องปลูกผลึกชนิดที่มีแหล่งกำเนิดอาร์เซนิกแบบของแข็ง  
 โครงสร้างควอนตัมคือดจะเปลี่ยนรูปร่างเป็นโครงสร้างคล้ายหลังอูฐ (Camel-like nanostructure) หลังจากผ่าน  
 การปลูกกลบด้วยชั้นแกเลียมอาร์เซไนด์แบบบางๆ โดยมีโครงสร้างนาโนโฮล (nanohole) อยู่ที่ด้านบน  
 ของควอนตัมคือด หลังจากนั้น เมื่อทำการปลูกชั้นอินเดียมอาร์เซไนด์ควอนตัมคือดทับซ้ำอีกรอบ โครงสร้างเดิม  
 จะเปลี่ยนแปลงเป็น โครงสร้างควอนตัมคือดแบบคล้ายใบพัด (nanopropeller) ที่ความหนาของชั้นอินเดียมอาร์เซ  
 ไนด์ควอนตัมคือด 0.6 โมโนเลเยอร์ และจะเปลี่ยนเป็น โครงสร้างควอนตัมคือดโมเลกุลที่มีจำนวนควอนตัมคือด  
 10-12 คือคือด 1 โมเลกุล เมื่อทำการเพิ่มความหนาของชั้นอินเดียมอาร์เซไนด์ควอนตัมคือดไปยัง 1.2 โมโนเลเยอร์  
 การควบคุมจำนวนของควอนตัมคือดต่อ โมเลกุลสามารถทำได้โดยเปลี่ยนอุณหภูมิที่ใช้ปลูกกลบ ที่อุณหภูมิปลูก  
 กลบที่ต่ำลง ทำให้จำนวนของควอนตัมคือดต่อ โมเลกุลลดลงหลังจากการปลูกชั้นอินเดียมอาร์เซไนด์  
 ควอนตัมคือดซ้ำ

ส่วนตัวอย่างชิ้นงานที่ปลูกด้วยเครื่องปลูกผลึกชนิดที่มีแหล่งกำเนิดอาร์เซนิกแบบก๊าซ หลังจากผ่านการ  
 ปลูกกลบด้วยชั้นแกเลียมอาร์เซไนด์แบบบางๆ โครงสร้างควอนตัมคือดจะเปลี่ยนรูปร่างเป็น โครงสร้างควอนตัม  
 ริง (quantum ring) และโครงสร้างเปลี่ยนเป็น โครงสร้างควอนตัมคือดคู่ที่ความหนาของชั้นอินเดียมอาร์เซไนด์  
 ควอนตัมคือด 0.6 โมโนเลเยอร์ เมื่อเปลี่ยนเงื่อนไขการปลูก โดยเพิ่มอุณหภูมิของแผ่นฐานระหว่างการปลูกชั้น  
 อินเดียมอาร์เซไนด์ควอนตัมคือด พร้อมทั้งทำการปลูกชั้นควอนตัมคือดนี้ไปด้วย พบว่าเกิดการก่อตัวของ  
 โครงสร้างควอนตัมคือดริง (quantum-dot ring) หลังจากนั้น เปรียบเทียบโครงสร้างที่เกิดขึ้น เมื่อเปลี่ยนเครื่องที่  
 ใช้ปลูกผลึกทั้งแบบชนิดของแข็งและก๊าซ พบว่า ระยะการเคลื่อนที่ของอะตอมกลุ่มที่ 3 ภายใต้บรรยากาศของอาร์  
 เซนิกที่ต่างกัน ( $As_2$  และ  $As_4$ ) เป็นสาเหตุหลักที่ทำให้เกิดการก่อตัวของ โครงสร้างผลึกที่แตกต่างกันไปในระดับ  
 นาโนเมตร

ภาควิชา ..... วิศวกรรมไฟฟ้า .....ลายมือชื่อนิสิต Sunaree Surapapojich  
 สาขาวิชา ..... วิศวกรรมไฟฟ้า .....ลายมือชื่ออาจารย์ที่ปรึกษา Nue  
 ปีการศึกษา ..... 2549 .....ลายมือชื่ออาจารย์ที่ปรึกษาร่วม Chabun



## 4570620121 : MAJOR ELECTRICAL ENGINEERING  
 KEY WORD: SELF-ASSEMBLY QUANTUM DOT MOLECULES /  
 INAS/GAAS / MOLECULAR BEAM EPITAXY

SUWAREE SURAPRAPAPICH: SELF-ASSEMBLED QUANTUM DOT  
 MOLECULES BY MOLECULAR BEAM EPITAXY AND THEIR  
 POTENTIAL APPLICATIONS. THESIS ADVISOR : PROF. SOMSAK  
 PANYAKEOW, D. Eng., THESIS CO-ADVISOR : PROF. CHARLES W.  
 TU, Ph.D. 131 pp.

The aim of this thesis is to investigate the formation mechanism of nanostructures, especially lateral quantum dot molecules (QDMs) using partial-capping-and-regrowth technique with both solid-source molecular beam epitaxy (MBE) and gas-source MBE. The physical and optical properties of all nanostructures are measured by *ex-situ* atomic force microscopy (AFM) and photoluminescence (PL).

With solid-source MBE under an  $As_4$  ambient, as-grown quantum dots (QDs) change to a camel-like nanostructure after being partially overgrown with GaAs (partial capping). When additional InAs is deposited (regrowth), QDMs with 10-12 dots per QDM are obtained. During the partial GaAs capping of InAs QDs, if the capping temperature is varied, the length of the nanopropellers can be controlled. The lowering of the capping temperature leads to smaller dot per QDM after regrowth process.

With gas-source MBE where  $As_2$  is generated by thermally cracked arsine, as-grown QDs are transformed into quantum rings after partial capping with GaAs. After the regrowth process, QD pairs or double QDs are obtained. At higher regrowth temperature, QD rings with 5-7 dots per ring are formed.

Surface morphologies of self-assembled (Ga)InAs nanostructures and QDMs grown by partial-capping-and-regrowth technique using gas-source MBE and solid-source MBE are compared. The difference in the migration length of group III adatoms under different arsenic species,  $As_2$  in gas-source MBE and  $As_4$  in solid-source MBE, is the origin of respective outcomes of nanostructures and QDMs.

Department ... Electrical Engineering ...

Student's signature ... *Suwaree Suraprapapich* ...

Field of study ... Electrical Engineering ...

Advisor's signature ... *Somsak Panyakeow* ...

Academic year ... 2006 ...

Co-advisor's signature ... *Charles W. Tu* ...

## Acknowledgements

I am deeply indebted to Prof. Dr. Somsak Panyakeow for guiding me with enthusiasm, encouraging me to continue doing the research, mentoring me on all aspects, and also giving me an opportunity to do the research in University of California, San Diego (UCSD), USA.

The experience in UCSD is the most rewarding one for me. I would like to express my sincere gratitude to Prof. Charles W. Tu for a chance to have an exciting experience both research and life in San Diego, USA.

I gratefully acknowledge all those who provided invaluable help during the research time at the Semiconductor Device Research Laboratory (SDRL), Department of Electrical Engineering, Faculty of Engineering, Chulalongkorn University. I appreciate the opportunity to be in one of the foremost research group in Thailand for semiconductor research. In particular, I am very grateful to Associate Professor Dr. Montri Sawadsaringkarn, Associate Professor Dr. Choopol Antarasena, Associate Professor Dr. Somchai Ratanathamphan, Associate Professor Dr. Songphol Kanjanachuchai and Dr. Chanin Wissawinthanon.

As always, this thesis could not have been completed without special help of colleagues and members the SDRL and the Department of Electrical and Computer Engineering (ECE), UCSD. These are colleagues at Chulalongkorn University: Mr. Supachok Thainoi, Dr. Suwat Sopitpan, Dr. Suwit Kiravittaya, Dr. Rudeesun Songmuang, Mrs. Kwanruan Thainoi, and colleagues at ECE, UCSD: Dr. Vladimiar Odnoblyudov, Mr. Yaoming Shen and Mr. Xiaotian Zhou.

Most of all, I am profoundly indebted to my parents for their encouragement and endless spiritual support during the time of difficulty. I would also like to thank my close friends who have shared the ups and downs and joyful times with me.

Finally, I would like to acknowledge the Royal Golden Jubilee (RGJ) scholarship for the research fund which made this work possible and also Prof. Charles W. Tu again for funding of a short research program at UC, San Diego, USA.

## CONTENTS

		Page
Abstract (Thai) .....		iv
Abstract (English) .....		v
Acknowledgements .....		vi
Contents .....		vii
List of Tables .....		x
List of Figures .....		xi
List of Symbols .....		xix
Chapter I	Introduction .....	1
1.1	Background .....	1
1.2	Objective .....	5
1.3	Overview .....	5
Chapter II	Low-dimensional nanostructures .....	7
2.1	Basic concepts of low-dimensional nanostructures .....	7
2.1.1	Bulk materials .....	9
2.1.2	Quantum wells .....	9
2.1.3	Quantum wires .....	10
2.1.4	Quantum dots .....	10
2.2	Formation of quantum dots and strain effects on island nucleation .....	15
2.2.1	Lattice mismatch stress and Stranski Krastanow growth mode .....	15
2.2.2	Thermodynamically approach .....	16
2.2.3	Kinetic approach .....	20
2.3	Spontaneous lateral alignment of QDs .....	22
2.4	Quantum dot self-alignment using vertical stacking .....	23
2.5	Quantum Dot Molecules .....	26

	Page
Chapter III	Experimental details ..... 31
3.1	Molecular beam Epitaxy ..... 31
3.1.1	Solid-source molecular beam Epitaxy ..... 31
3.1.2	Gas-source molecular beam Epitaxy ..... 33
3.2	Reflection high-energy electron diffraction in molecular beam Epitaxy ..... 34
3.3	Photoluminescence ..... 40
3.4	Atomic force microscopy ..... 42
3.5	Sample preparation ..... 43
Chapter IV	Partial-capping-and-regrowth technique with solid-source molecular beam Epitaxy ..... 45
4.1	Self-assembled InAs quantum dots ..... 45
4.2	Partial-capping-and-regrowth process ..... 47
4.2.1	Capping Process ..... 47
4.2.2	Regrowth Process ..... 53
4.2.3	The regrowth thickness: the formation of quantum dot molecules ..... 54
4.2.4	Capped temperature: controlled the number of QDs in QDMs ..... 58
4.2.5	Regrowth temperature ..... 60
4.2.6	Multi-cycles of partial-capping-and-regrowth technique ..... 61
4.2.7	Self-assembled elongated nanostructure ..... 65
4.2.8	Modified growth technique for high dot density ..... 68
Chapter V	Partial-capping-and-regrowth technique with gas-source molecular beam Epitaxy ..... 71
5.1	Double QDs ..... 72
5.1.1	Optical properties of DQDs ..... 74



	Page
5.2 The formation of QD rings .....	79
Chapter VI Comparison of nanostructures grown by solid-source MBE and gas-source MBE .....	81
Chapter VII Conclusion .....	88
References .....	90
Appendix .....	98
List of Publications .....	99
List of Presentations .....	103
Vitae .....	109



สถาบันวิทยบริการ  
จุฬาลงกรณ์มหาวิทยาลัย

**LIST OF TABLES**

Page

Table 5.1	The parameters from Vashni equation of as-grown DQDs and annealed DQDs at 650°C, 750°C and 850°C comparing with InAs and GaAs.....	78
-----------	--	----



สถาบันวิทยบริการ  
จุฬาลงกรณ์มหาวิทยาลัย

## LIST OF FIGURES

		Page
Figure 2.1	(a) Schematic views and graphs of (a) bulk, (b) quantum wells, (c) quantum wires, and (d) QD and their density of states (D.O.S.). (Sugawara, 1999).....	8
Figure 2.2	Illustrated of (a) density of states, (b) – (d) energy spreading under the low-carrier-limit condition in bulk material (b), QW (c) and QD (d). (Masumoto and Takagahara, 2002).....	12
Figure 2.3	Schematic representation of the three crystal growth modes (a) Layer-by-layer or Frank-van der Merve; (b) island or Volmer-Weber; (c) layer-plus-island or Stranski-Krastanow mode. (Herman and Sitter., 1989) .....	13
Figure 2.4	Energy of an array of 3D coherently strained islands per one atom versus island size $L$ . The control parameter $\alpha$ depends on the contribution from the surface energy and the edge energy. ....	18
Figure 2.5	Equilibrium phase diagram as a function of the coverage $H$ and misfit $\epsilon$ . The small panels on the top and the bottom illustrate the morphology of the surface in the six growth modes. The small empty islands indicate the presence of stable islands, while the large shaded one refers to ripened islands. (Daruka and Barabási, 1997).....	19
Figure 2.6	Schematic represent the local strain energy density in and around the QD. The energy barrier for the adatoms' diffusion to the QD has a maximum at the edge of the QD. (Seifert et al., 1996) .....	21

Figure 2.7	(a), (b) The AFM images of (a) multi-atomic steps on GaAs layer sample A grown on a vicinal (111B) GaAs, (b) InGaAs islands sample B prepared by depositing a nominally 3-nm-thick $\text{In}_{0.3}\text{Ga}_{0.7}\text{As}$ layer onto multi-atomic steps of GaAs. (Akiyama and Sakaki, 2006).....	22
Figure 2.8	Typical $g = (400)$ bright field TEM pictures taken along [011] azimuth for the samples with two sets of islands separated by (a) 46 and (b) 92 ML spacer layers, respectively. Arrows point to the island positions indicated by the strain contrast. (c) A typical $g = (200)$ dark field TEM picture for a sample with five sets of islands separated by 36 ML spacer layers. (Xie et al., 1995) .....	23
Figure 2.9	Experimentally observed pairing probabilities (open squares) as a function of the spacer thickness $z_s$ , shown on a log-log plot for samples with two sets of islands (a) [011] cross section, and (b) $[01\bar{1}]$ cross section. (Xie et al., 1995) .....	24
Figure 2.10	A schematic representation shows the two major processes for the In adatom migration on the stressed surface: (1) directional diffusion under mechanochemical potential gradient contributing towards vertical self-organization and (2) largely symmetric thermal migration in regions from the islands contributing to initiation of new islands not vertically aligned with islands below. (Xie et al., 1995) .....	26



Figure 2.11	(a) Cross-sectional STEM image of the CQD sample with $d=7$ nm. (b) PL spectra of a single pair of CQD with different barrier thicknesses at a low excitation intensity, where the excitation energy is 1.41 eV absorption band of wetting layer. The barrier thickness, bonding state, and antibonding state are labeled $d$ , $X^+$ , and $X^-$ , respectively. $E$ indicates the energy separation between the $X^+$ and $X^-$ PL groups. The PL spectrum of a single layer QD sample is also shown at the top of figure for reference. (Yamauchi et al. 2005).....	27
Figure 2.12	(a) QDM PL spectra at 4 K, and (b) the PL peak energy of $X1$ and $X2$ as a function of applied voltage along the QDM axis under pulsed excitation at 818 nm (1.52 eV) and a PD of 200 W/cm <sup>2</sup> . A redshift is apparent at the alignment bias (dashed vertical line) indicating that the electron ground states of the two QDs are in resonance. The dashed curves are guides to the eye indicating the expected behavior without coupling. (Beirne et al., 2006) .....	28
Figure 2.13	Schematic diagrams illustrating the predictions of the 1D model used to qualitatively describe the coupling mechanism and its control using an $E$ field. (Beirne et al., 2006).....	29
Figure 3.1	Schematic drawing of solid-source MBE growth chamber. ....	32
Figure 3.2	Schematic drawing of gas-source MBE growth chamber. ....	33
Figure 3.3	The Ewald sphere and reciprocal lattice rods for a simple square net. (Masumoto and Takagahara, 2002).....	35
Figure 3.4	Observed RHEED patterns of GaAs(100)-(2×4) surface Reconstruction. ....	36
Figure 3.5	Schematic crystal arrangement of surface reconstruction on GaAs (100) surface. (Masumoto and Takagahara, 2002).....	37

Figure 3.6	RHEED pattern to observe transition temperature from (2×4) to c(4×4). .....	38
Figure 3.7	Intensity oscillations of the specular beam in the RHEED pattern from a GaAs(100)-(2×4) reconstructed surface, [011] azimuth. (Masumoto and Takagahara, 2002).....	38
Figure 3.8	Observed RHEED patterns during InAs growth. ....	39
Figure 3.9	Two typical oblique streaks starting from the same reciprocal lattice point. (Masumoto and Takagahara, 2002).....	39
Figure 3.10	Schematic of the PL experimental set up. ....	40
Figure 3.11	Simple interpretation of the PL data obtained from a QD structure. In case of small QD (a): the PL peak energy position is higher compared with large QD (b). (Kiravittaya, 2002) .....	41
Figure 3.12	Simple interpretation of the PL spectrum obtained from the QD structure. In (a) the PL spectrum is very narrow due to the delta-function like density of states; and in (b) the average dot size corresponds to the PL peak energy position and the PL linewidth corresponds to the size distribution of the array. (Kiravittaya, 2002) .....	42
Figure 3.13	A schematic of AFM system when operated in tapping-mode. ....	43
Figure 3.14	Schematic of sample structure. ....	44
Figure 4.1	Schematic representation of atomic processes occurring during GI. The curves correspond to the local surface strain energy density. (a) the InAs cluster is less stable, hence leading to the detachment of indium atoms from the clusters to the smaller InAs QD. (b) The diffusion process improves the size homogeneity of QD ensembles. (b) Indium atoms from the QDs start to desorb when the GI time is increased. (Kiravittaya, 2002) .....	47

- Figure 4.2 Planview (left) and oblique angle (right) AFM images of camel-like nanostructures with a nanohole on top of the dot. ....48
- Figure 4.3 Schematic illustration of a QD capped at low temperature.  
 (a) A free-standing InAs QD. (b) The QD collapses during capping with thin GaAs. The indium atoms detach from the QD and diffuse to intermix with GaAs on the flat GaAs surface. Due to less intermixing with the low temperature capping, the indium compositional profile induces non-preferential growth on the top of the QD (c). The effects of the compositional profile are less pronounced for thick capping layer thicknesses (d) and (e). (Kiravittaya, 2002) .....48
- Figure 4.4 (a)-(e) Schematic of the transformation from a large InAs island partially overgrown by a GaAs capping layer to a hole in five steps. (f) The energetics in the case of partially covered three-dimensional islands with a density of  $4.4 \times 10^9 \text{ cm}^{-2}$ . The calculated total energy (*solid line*) and its contributions (*dashed lines*) for the various stages of island dissolution are shown. (g) The energetics for a density of  $4.4 \times 10^9 \text{ cm}^{-2}$  (*solid lines*) compared with those for a density of  $10^{10} \text{ cm}^{-2}$  (*dashed lines*). (Wang et al., 2001) .....50
- Figure 4.5 Schematic illustrations of the term  $\Omega E_s(\mathbf{r}) - \frac{\zeta \Omega g(\mathbf{r})}{a}$  for  
 (a) free-standing (b) partially capped InAs QDs with thin GaAs. (c) The chemical potential of Ga atoms during the overgrowth process. (Songmuang, 2003) .....52

Figure 4.6	Planview (left) and oblique angle (right) AFM images of nanopropeller-like QDs. ....	53
Figure 4.7	AFM images of the samples with regrowth thickness of (a) 0.6 ML, (b) 0.9 ML, (c) 1.2 ML, and (d) 1.5 ML. ....	55
Figure 4.8	Histograms of (a) nanopropeller type quantum dots, (b) QDMs (center dots), and (c) QDMs (satellited dots). ....	55
Figure 4.9	Room temperature PL spectra of QDs regrown on the nanoholes template where the regrown thicknesses are 0.6, 0.9, 1.2 and 1.5 ML. ....	56
Figure 4.10	AFM images of nanopropeller QDs (a)-(c) at the regrowth thickness of 0.6 ML with their span lengths of the propeller blades (g)-(i) and QDMs (d)-(f) with the regrowth thickness of 1.2 ML at the capping temperature of 470°C, 450°C and 430°C, respectively. ....	59
Figure 4.11	AFM image of showing the evolution of self-assembled lateral QDM. ....	60
Figure 4.12	Histogram of the number of QDs per molecule when increasing the growth temperature from 430°C to 500°C during the regrowth process. ....	61
Figure 4.13	The AFM images of regrown QDs by multi-cycle of thin-capping-and-regrowth MBE process at (a) 1 (b) 3 (c) 5 (d) 7 and (e) 10 cycles, respectively. ....	63
Figure 4.14	Room temperature PL spectra of QDs grown by 1, 3, 7 and 10 cycles. ....	64
Figure 4.15	QDM (b) originated from as-grown QD (a) by the partial-capping-and-regrowth MBE process. Aligned QDMs (d) are grown from aligned QDs (c) using the partial-capping-and-regrowth process. ....	65
Figure 4.16	AFM images of inhomogeneously self-assembled InAs nanostructure. ....	66



Figure 4.17	AFM images of uniformly self-assembled InAs nanostructure with an average length of 0.5 $\mu\text{m}$ . .....	67
Figure 4.18	RHEED and AFM images at different growth steps. ....	67
Figure 4.19	The transformation from self-assembled quantum dots to self-assembled elongated nanostructure through thin capping, regrowth of quantum dots on templated nanoholes and annealing process. ....	68
Figure 4.20	AFM image of high dot density QDMs grown by 5 cycles of thin-capping-and-regrowth process with regrowth thickness of 0.6 ML in the first 4 cycles and 1.5 ML in the last cycle. ....	69
Figure 4.21	PL spectrum of high dot density QDMs from modified growth technique. ....	70
Figure 5.1	(a) AFM image and (b) dot height histogram with Gaussian fit of as-grown QDs; (c) AFM image of QRs, (d) and AFM image and (e) dot height histogram with a Gaussian fit of DQDs. ....	73
Figure 5.2	Center-to-center width histogram of DQDs with Gaussian fit. ....	74
Figure 5.3	PL spectra of as-grown QDs and DQDs at 9 K. The dotted curves for DQDS are the Gaussian components. ....	75
Figure 5.4	The temperature dependent peak emission energy of as-grown QDs and DQDs. The solid lines are calculations from the Varshni equation. ....	76
Figure 5.5	The temperature dependence of PL intensity of as-grown QDs and DQDs. ....	77
Figure 5.6	Planview (a) and oblique view (b) AFM image of a QD ring. ....	80
Figure 5.7	The histogram of number of dots per ring. ....	80

Figure 6.1	AFM images of (a) as-grown QDs, (b) camel-like nanostructures, (c) nanopropeller-like QDs with the regrowth thickness of 0.6 ML and (d) QDMs with the regrowth thickness of 1.2 ML grown under $As_4$ overpressure in solid-source MBE. ....	83
Figure 6.2	AFM images of (a) as-grown QDs, (b) QRs and (c) DQDs with the regrowth thickness of 0.6 ML, grown under $As_2$ overpressure in gas-source MBE. In case of DQDs sample (c), at point A where initial merging starts, at point B where a DQD is merging into a single dot, and at point C where a completely merged QD is obtained. ....	85
Figure 6.3	Close-up AFM images of (a) an as-grown QD, (b) QR, (c) DQD, (d) initial merging of a DQD and (e) merging into single dot. ....	85
Figure 6.4	Photoluminescence spectra of nanopropeller QDs by solid-source MBE and QRs, DQDs by gas-source MBE at 9 K. ....	86

## LIST OF SYMBOLS

$\nabla^2$	Laplacian operator
$\alpha$	control parameter
$a$	hydrostatic deformation potential
$a_L$	lattice constant of deposited material
$a_S$	lattice constant of substrate material
$A$	surface area
Al	Aluminium
As	arsenic
AFM	atomic force microscopy
AsH <sub>3</sub>	Arsine
Be	beryllium
CB	conduction band
CQD	coupled quantum dots
$\delta$	delta function
$\Delta\gamma$	change of surface free energy
$\Delta E_g$	shift of conduction band minimum due to strain
$D_{\text{bulk}}(E)$	bulk density of state
$D_{\text{QW}}(E)$	quantum well density of state
$D_{\text{QWR}}(E)$	quantum wire density of state
$D_{\text{QD}}(E)$	quantum dot density of state
D.O.S.	density of state
DQD	double quantum dots
$\varepsilon$	misfit
$\varepsilon_0$	lattice mismatch
$\varepsilon_{\text{ax}}$	uniaxial strain component
$\varepsilon_{\text{vol}}$	hydrostatic strain component
$\varepsilon_{\text{xx}}$	axial strain in $x$ -direction
$\varepsilon_{\text{yy}}$	axial strain in $y$ -direction
$\varepsilon_{\text{zz}}$	axial strain in $z$ -direction

$\epsilon_{xz}$	shear strain on $x$ -plane directed through $z$ -direction
$\epsilon_{yz}$	shear strain on $y$ -plane directed through $z$ -direction
$\epsilon_{//}$	in-plane strain
$\epsilon_{\perp}$	strain in perpendicular to the growth direction
$E$	carrier energy or total energy per unit cell
$E_0$	characteristic energy
$E_g$	band gap energy
$E_{l,x}$	quantized energy in $x$ -direction
$E_{m,y}$	quantized energy in $y$ -direction
$E_{n,z}$	quantized energy in $z$ -direction
$E(\text{el})$	elastic strain energy
$E_{\text{WL}}$	energy of wetting layer
$E_{\text{rip}}$	energy of ripened island
$E_{\text{island}}$	energy of single island
$E_{\text{elastic}}$	elastic strain energy
$E_{\text{surface}}$	island surface energy
$E_{\text{edge}}$	island edge energy
$F(\mathbf{r})$	envelope wave function
FM	Frank-van der Merve
FWHM	full width at half maximum
$\gamma_e$	surface free energy of the epilayer/vacuum interface
$\gamma_i$	surface free energy of epilayer/substrate interface
$\gamma_s$	surface free energy of the substrate/vacuum interface
$\mathbf{G}$	reciprocal lattice vector
GaAs	gallium arsenide
GeSi	germanium silicon
$h$	Planck's constant or height of pyramidal quantum dot
$\hbar$	reduced Planck's constant
$h_c$	critical thickness of strained layer



$i$	critical island size
InAs	indium arsenide
InGaAs	indium gallium arsenide
$\kappa(\mathbf{r})$	surface curvature
$k$	amplitude of wave vector
$k_B$	Boltzmann's constant
$k_{//}$	amplitude of in-plane ( $y$ - $z$ ) wave vector
$k_{\perp}$	amplitude of wave vector in $x$ -direction
$\mathbf{k} = (k_x, k_y, k_z)$	carrier wave vector
$\mathbf{k}_{in}$	wave vectors of incident electron
$\mathbf{k}_{diff}$	wave vectors of diffraction electron
$\lambda$	elastic modulus
$\lambda_{de\ Broglie}$	de Broglie wavelength
$l$	quantum number in $x$ -direction
$L$	macroscopic length scale or base size of pyramidal quantum dot
$L_0$	characteristic length
$L_{opt}$	optimal island size
$L_x$	nanometer length scale in $x$ direction
$L_y$	nanometer length scale in $y$ direction
$L_z$	nanometer length scale in $z$ direction
$m$	quantum number in $y$ -direction
$m^*$	effective mass
$m_{eff}$	carrier effective mass
MBE	molecular beam epitaxial or molecular beam epitaxy
MFC	mass flow controller
ML	monolayer
Mo	molybdenum
$n$	quantum number in $z$ -direction
$N_D$	volume density of quantum dot

$N_e$	number of state per unit surface
$N_{wi}$	area density of quantum wire
$p$	carrier momentum
P	phosphorus
PBN	pyrolytic boron nitride
PH <sub>3</sub>	phosphine
PL	photoluminescence
$Q$	total deposited material (monolayer)
QW	quantum well
QWR	quantum wire
QD	quantum dot
$\mathbf{r} = (x, y, z)$	carrier position vector
RHEED	reflection high-electron energy diffraction
Re	rhenium
RF	radio frequency
RT	room temperature
$\sigma$	Poisson's ratio
Si	silicon
SiGe	silicon germanium
SK	Stranski-Krastranow
STM	scanning tunneling microscopy
$\Theta$	Heaviside's unit step function
$t$	film thickness
$T$	temperature
TEM	transmission electron microscopy
$\mu_0$	chemical potential
$V(\mathbf{r})$	confinement potential
VW	Volmer-Weber
W	tungsten
WL	wetting layer
$X^+$	bonding state
$X$	antibonding state

# CHAPTER I

## INTRODUCTION

### 1.1 Background

Recent developments in crystal growth techniques have made semiconductors even more versatile. In low-dimensional semiconductor systems, the carriers are confined in small regions formed by potential barriers. The success of semiconductor quantum wells is from the study of two dimensional (2D) optical and electronic effects of carriers due to lateral confinement. Several research works have also been carried out in quasi-one-dimensional quantum wires (1D) and zero-dimensional (0D) quantum dots (QDs). Especially, in semiconductor QDs, the quantum nature of QDs has quantized energy states with zero degree of freedom of carrier (Arakawa and Sakaki, 1982; Grundmann, 2002); therefore, excitons are confined in all spatial directions on a length scale comparable to the exciton Bohr radius. Many interesting phenomena are expected, such as discrete energy structure,  $\delta$ - function like density of states, and high optical nonlinearity (Woggor, 1997). These characteristic properties of semiconductor QDs have attracted an enormous amount of interest for opto-electronic device applications.

Many experimental results have been reported in literature about the QD applications. One of them is for quantum computing. In digital computers information is represented in classical 'bits' by either 0 or 1. Whereas, quantum information is represented in "quantum bits" (qubits) with wavefunctions  $\Psi = \alpha|0\rangle + \beta|1\rangle$ . These bits contain much more information. Quantum information technology can form the basis for powerful encryption schemes and secure communications for ultra-powerful computation. The physical implementations of qubits are the key requirement for these technologies, particularly of the coupled qubits for quantum gates. Two qubits gates are the bases for manipulation of information in quantum

computing. Solid state quantum dots with their sharp optical lines behave like artificial atoms and are of great interest as qubits. Although quantum dot implementations for qubits have been widely studied, appropriately coupled quantum dots for two qubit gates have not been achieved well to date. Nevertheless, there are several research groups (Pfannkuche et al., 1998; Craig et al., 2004; Hatano et al., 2005) which have demonstrated coupled quantum dots for gates and also studied their electronic properties, such as the dependence of the energies on separation from overlap of the electrons and holes wavefunctions in the two dots, and coulomb interactions between the electron and hole. One of the implementation for quantum computing is based on quantum dot cellular automata (QCA). Lateral QDMs with 4 dots per cell have the potential to be a building block of QCA. Lent et al. (1993) proposed the principle of QCA, which is based on charge control in a square cell with 4 dots at its vertices. When the cell contains two excess electrons, they will arrange themselves into the most stable states; the electrons will be located in the diagonal QDs, due to Coulombic repulsion of like charges. When inter-dot barriers are high, two excess electrons tend to align along either one diagonal, representing either a “1” or “0” state. The interaction between cells is purely Coulombic: no net current flows along the cells, leading to extremely low power consumption (Timler and Lent, 2002). As a consequence, 4-5 dots per molecule could be achieved using appropriate a nano-template.

There are two main approaches that have been used to grow QDs. First is “top-down” approach: QDs are fabricated by patterning using several techniques such as chemical etching, selective growth or lithography techniques (i.e., X-ray lithography, electron beam (EB) lithography and focused ion beam lithography, etc.). The attractive advantages of these techniques are controllable QD size and spatial arrangement. However, these techniques are complicated and create material defects leading to degradation of their electronic and photonic properties. In another approach, “bottom-up”, or self-assembly, which has been used to fabricate QDs in this research work, occurs by the formation of highly strained structure of heteroepitaxial growth. The evolution of an initially two-dimensional (2D) growth of a few monolayers (MLs) thick wetting layer into a three dimensional (3D) island growth is referred to as **Stranski-Krastanow (SK)** growth mode (Herman and Sitter,



1989; Seifert et al., 1996; Cullis et al., 2002). There are in-depth studies on the growth mechanism in order to understand 3D QD formation. Leonard et al. (1993) found that quantum-sized island structures having dislocation-free and acting as three-dimensional carrier confinement structure were obtained during the transition of the initial stage of growth of highly strained material on the substrate. The elastic strain relaxation on facet edges and island interaction via the strained substrate are the driving forces for the uniformity of self-assembled ordered arrays that are coherently strained island on crystal surface (Shchukin et al., 1995). Wang et al. (2001) investigated that controlling the growth conditions and the amount of deposited material can select island size and shape. Moreover, a theoretical study using density functional theory of the formation of self-assembled coherent islands in SK growth mode is presented by calculating the surface energies for both the island facets and the wetting layer. Both thermodynamic and kinetic ordering mechanisms together can create unique 3D patterns of islands within the matrix in various strained semiconductor systems in the SK growth mode, including  $\text{In}_x\text{Ga}_{1-x}\text{As}/\text{GaAs}$  (Zhan et al., 2003; Jacobi, 2003; Miao et al., 2005; Mi and Bhattacharya, 2005),  $\text{Ge}_{1-x}\text{Si}_x/\text{Si}$  (Voigtlander, 2001; Fitting et al., 2005), and others (Medeiros-Ribeiro et al., 2001; Lee et al., 2005). For this thesis,  $\text{In}_{1-x}\text{Ga}_x\text{As}/\text{GaAs}$  having 7% lattice mismatches has been used for the investigation. This material combination appears to be the most promising candidate for immediate device application. The growth of InAs QDs on GaAs substrate results in dots of varying dimensions randomly distributed across the substrate. The randomness of QD sizes gives rise to devices with varied electrical and optical characteristics (Joyce et al., 2000).

When the QDs are used for device applications, they must be embedded in the matrix, in this case, GaAs. Many experimental results have been studied on the effects of GaAs overgrowth on the structural of InAs QDs. Joyce et al. used *in-situ* scanning tunneling microscopy (STM) to investigate the evolution of surface morphology during the overgrowth of large InAs QDs. Due to the different initial strain states of the QDs, the development of the surface morphology of larger QDs is very different than that of smaller QDs under the same conditions (Joyce et al., 2001). While Songmuang et al. (2003) proposed that the observation of the surface evolution could be explained by the effects of elastic energy and surface energy included in the

surface chemical potential. Increasing the elastic energy of QDs and surface energy of the cap induces In atoms to migrate from InAs QDs to the GaAs surface. As the shape of InAs QDs changes dramatically during the initial stage of GaAs overgrowth, the precise thickness is used to control the shape of the QDs during the overgrowth process (Pistol et al., 1995; Joyce et al., 2001).

Recently, several attempts, have succeeded to fabricate quantum dot molecules (QDMs) having both lateral and vertical arrangement. QDMs are groups of closely spaced QDs formed on the surface of a substrate. *Vertically* stacked QDs are sometimes referred to as QDMs due to the closely spaced nature of the structure (Austing et al., 1998; Paskov et al., 2000; Jaskoski et al., 2003). Successful lateral QDM results use a combination of pre-patterned substrate and self-assembling technique; for example, AsBr<sub>3</sub> *in situ* etching and molecular beam epitaxy (MBE) can be combined to create *lateral* QDMs (Kiravittaya et al., 2003; Songmuang et al., 2003). The *in situ* etching leads to fabricating of nanoholes in nano-sized resolution. This is followed by MBE growth process to deposit InAs QDs on the nanoholes forming *lateral* QDMs. The second technique, Lippen et al., (2004) reveals the technique using self-organized anisotropic strain engineering of an In(Ga)As/GaAs superlattice (SL) template on GaAs to create an ordered lattice of *lateral* InAs QDMs (Mano et al., 2002; Lippen et al., 2005). Furthermore, Lee et al. (2006) adopted a hybrid growth approach utilizing both droplet epitaxy and self-assembling technique on a planar GaAs substrate. Droplet homoepitaxy technique is used to grow nanoscale-sized GaAs mound as templates for growing InGaAs QDMs. The number of QDs per molecule varies from two to six dots depending on the specific InAs monolayer coverage.

In this research work, the partial-capping-and-regrowth technique is intentionally used to fabricate *lateral* QDMs. With solid-source MBE in which As<sub>4</sub> is used, partial-capping process at the *low* temperatures gives rise to camel-like nanostructures having nanoholes on top of the nanostructures. Additionally, changing of QD capping thickness can precisely tune the structural properties of the nanoholes. Subsequently, groups of lateral closely spaced QDs, referred as *lateral* QDMs, are formed by regrowth. Self-assembled *lateral* QDMs have a specific pattern of dot sets

and dot alignment along the  $[1\bar{1}0]$  crystallographic direction with 5-12 dots per molecule.

When  $\text{As}_2$  is used as in gas-source MBE, different nanostructures are formed. We found that, after the partial capping process, the QD shape changes to a quantum ring structure. When additional InAs is deposited, double QDs (DQDs) are formed. Moreover, with an increase in the regrowth temperature, QD rings with 5-7 dots per ring are formed.

## 1.2 Objective

The objective of this work is to study the formation of nanostructures, especially lateral quantum dot molecules (QDMs). Surface morphologies and dot ensembles of QDMs grown by the partial-capping-and-regrowth technique using solid-source molecular beam epitaxy (MBE) and gas-source MBE are observed, and the effect of arsenic species on the formation of nanostructures and QDMs is discussed.

## 1.3 Overview

This thesis is composed of two major parts. The first part is a study of the formation of nanostructures and lateral QDMs with solid-source MBE using partial-capping-and-regrowth. Different nanostructures are formed with modified growth parameters. Physical and optical properties are observed by atomic force microscopy (AFM) and photoluminescence (PL), respectively.

The second part is dealing with the investigation of the lateral QDMs using partial-capping-and-regrowth by gas-source MBE. Surface morphologies and optical properties of these structures are also observed in this part.

The thesis is organized as follows. Chapter 1 is the introduction and review of quantum dot research. Chapter 2 provides the basic concept of low-dimensional semiconductor nanostructures with theories of self-assembled QDs. Chapter 3 provides experimental details including sample preparation and characterization process. Chapter 4 gives experimental results of physical and optical properties when

changing the growth conditions with partial-capping-and-regrowth using solid-source MBE. Chapter 5 reveals experimental data with the same growth process with Chapter 4 but using gas-source MBE. In addition, the surface morphologies of nanostructures grown under different arsenic species are compared in this chapter. Finally, Chapter 6 is the conclusion of this work.



สถาบันวิทยบริการ  
จุฬาลงกรณ์มหาวิทยาลัย

## CHAPTER II

### LOW-DIMENSIONAL NANOSTRUCTURES

For several decades, spontaneous formation of periodic structure is a general phenomenon in solid state. In recent years, the theoretical concepts and experimental results on the formation of ordered nanometer-scale structures on a crystal surface have been intensely interested and dramatically investigated. The reliable and accurate investigation of surface structures has been progressed in precise experimental techniques such as atomic force microscopy (AFM), scanning tunneling microscopy (STM) and transmission electron microscopy (TEM). Therefore, study on nanometer-scale semiconductor can be profoundly analyzed.

The self-assembled QDs grown by Stranski-Krastanow (S-K) growth mode are widely investigated. Several groups have tried to explain the formation of QDs and strain effects on island nucleation. In this chapter, techniques for spontaneous laterally aligned QDs and vertical stacking are discussed.

#### 2.1 Basic concepts of low-dimensional nanostructures

When the size of the crystal is reduced from the centimeter to the nanometer scale of the order of the de Broglie wavelength of an electron, as shown in equation 2.1, the reduction of the dimensionality gives rise to confinement of electron movement in the respective direction. As illustrated in figure 2.1, the carriers in quantum wells (QWs) are localized in the direction perpendicular to the layer but move freely in the layer plane (x-y plane), while those in quantum wires (QWRs) are localized in two directions and can move along the wire axis (x-direction). In quantum dots (QDs), the carriers are completely confined in all three directions. This confinement leads to discrete quantized energy levels to the variation of carrier density of states. A totally discrete energy spectrum in QDs is illustrated in figure 2.1(d).



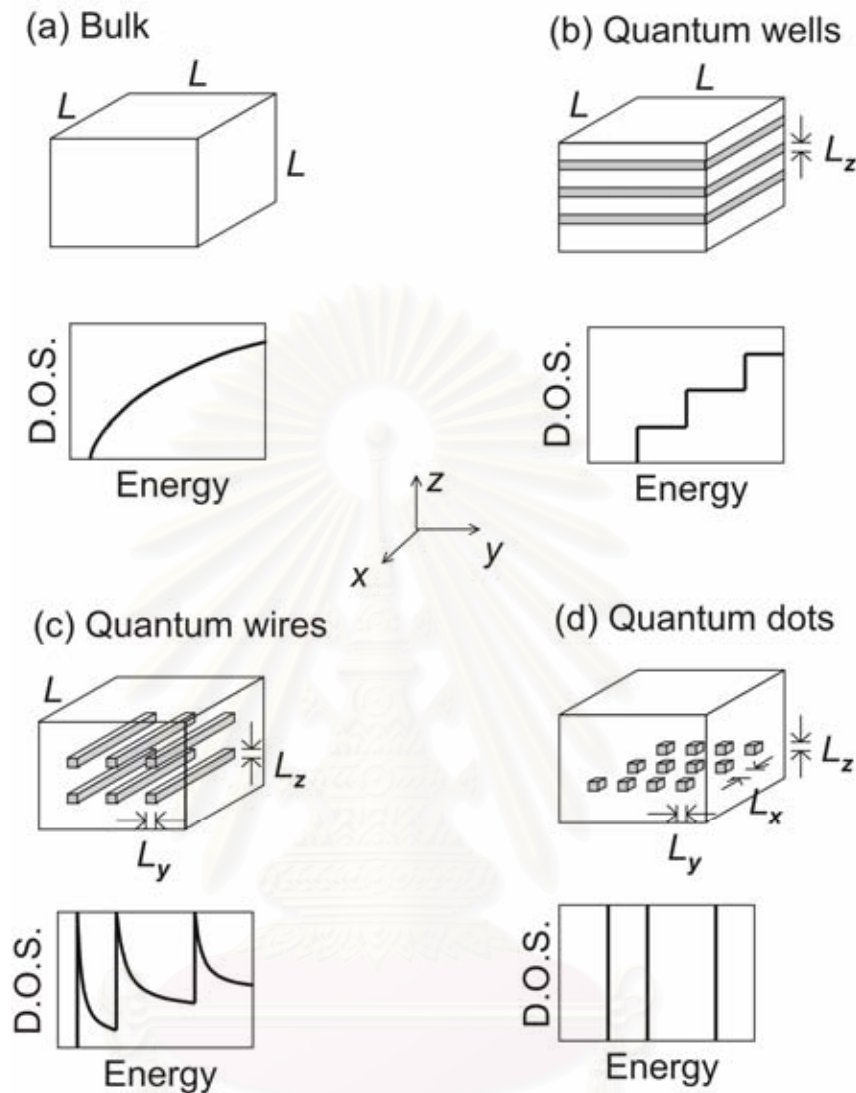


Figure 2.1 Schematic view and graphs of (a) bulk, (b) quantum wells, (c) quantum wires, and (d) QDs and their density of states (D.O.S.). (Sugawara, 1999).

$$\lambda_{\text{de Broglie}} = \frac{h}{p} = \frac{h}{\sqrt{3m_{\text{eff}}k_B T}} \quad (2.1)$$

An elementary quantum-mechanical approach is used to calculate the energy, the wave function and the density of states, which depend on the dimensionality of quantum nanostructures. The electronic state of a bulk semiconductor can be effectively described by the effective-mass approximation, as can quantum energy

shift as a function of the well-layer width for semiconductor QWs. Assuming parabolic band dispersion, one can describe band-edge electron states of semiconductors by the Schrödinger equation (effective-mass equation) as

$$\left[ -\frac{\hbar^2}{2m^*} \nabla^2 + V(\mathbf{r}) \right] F_k(\mathbf{r}) = EF_k(\mathbf{r}) \quad (2.2)$$

where  $m^*$  is the effective mass;  $\hbar$  is the Planck's constant divided by  $2\pi$ ;  $\mathbf{r} = (x, y, z)$  is the electron position vector;  $V(\mathbf{r})$  is the confinement potential,  $F_k(\mathbf{r})$  is the envelope wave function; and  $E$  is the carrier energy. (Sugawara, 1999)

From equation (2.2), if there is no potential barrier, the eigenenergy ( $E_{bulk}$ ), and density of states  $D_{bulk}(E)$  are given as follows.

### 2.1.1 Bulk materials

$$E_{bulk}(k) = \frac{\hbar^2 k^2}{2m^*} \quad (2.3)$$

$$D_{bulk}(E) = \frac{1}{2\pi^2} \left( \frac{2m^*}{\hbar^2} \right)^{3/2} E^{1/2} \quad (2.4)$$

where  $\mathbf{k} = (k_x, k_y, k_z)$  is the wave vector as  $k^2 = k_x^2 + k_y^2 + k_z^2$ .

### 2.1.2 Quantum wells

If one assumes that the confinement potential for a square quantum well is infinite in the  $z$  direction, the eigenenergy  $E_{QW}$  is

$$E_{QW}(k) = \frac{\hbar^2 k_{\parallel}^2}{2m^*} + E_{n,z} \quad (2.5)$$

and the density of state is

$$D_{QW}(E) = \frac{m^*}{\pi \hbar^2 L_{QW}} \sum_{n_z} \Theta(E - E_{n_z}) \quad (2.6)$$

where  $k_{\parallel}^2 = k_x^2 + k_y^2$ ,  $\Theta$  is the Heaviside's unit step function,  $n_z = 1, 2, 3, \dots$   $L_{QW}$  is the sum of the well and barrier thicknesses. The minimum energy and the energy separation between each quantized state increase as the well width is decreased.

### 2.1.3 Quantum wires

If one assumes that the confinement potential barriers for a square quantum wire are infinite in the  $y, z$  direction, one obtains

$$E_{QWR} = \frac{\hbar^2}{2m^*} \left[ k_x^2 + \left( \frac{n_y \pi}{L_y} \right)^2 + \left( \frac{n_z \pi}{L_z} \right)^2 \right] \quad (2.7)$$

$$D_{QWR}(E) = \frac{N_{wi}}{\pi} \frac{\sqrt{2m^*}}{\hbar} \sum_{m, n} \frac{1}{\sqrt{E - E_{m,y} - E_{n,z}}} \quad (2.8)$$

where  $n_y, n_z = 1, 2, 3, \dots$ ,  $L$  is the length of the quantum wire and  $N_{wi}$  is the area density of the quantum wire (the number of quantum wires divided by the quantum-wire region area in the  $y-z$  plane).

### 2.1.4 Quantum dots

If one assumes that the confinement potential barrier has infinite potential height for all directions,

$$E_{QD} = \frac{\hbar^2}{2m^*} \left[ \left( \frac{n_x \pi}{L_x} \right)^2 + \left( \frac{n_y \pi}{L_y} \right)^2 + \left( \frac{n_z \pi}{L_z} \right)^2 \right] \quad (2.9)$$

$$D_{\text{QD}}(E) = 2N_D \sum_{l, m, n} \delta(E - E_{l,x} - E_{m,y} - E_{n,z}) \quad (2.10)$$

where  $N_D$  is the volume density of QD and  $\delta$  is the delta function.

The energy distributions of electrons in bulk, QW, and QD structures under a low carrier-density limit condition, where electrons obey Boltzmann's distribution, are illustrated in figure 2.2 (a). In the bulk structure, from equation (2.4) as the density of states is proportional to the square root of electron energy, the energy distribution of electrons has a width of about 1.8 kT, where k is Boltzmann's constant and T is temperature, as shown in figure 2.2 (b). In QWs, where electrons are one-dimensionally localized into a thin layer that forms a quantum mechanical potential well, the density of states which is proportional to the Heaviside step function in equation (2.6), becomes like a staircase. Hence, the density of states becomes constant and independent of energy at the band edge. The energy distribution of electrons becomes about 0.7 kT, which is less than half that in the bulk structure, as illustrated in figure 2.2(c). A concentration of electrons into a narrower energy distribution is enabled from this reduction. When the electrons are injected into such structures, consequently, a narrower emission linewidth can be expected. In the QWRs, the density of states is inversely proportional to the square root of energy, as shown in figure 2.2 (a), according to equation (2.8). In the case of QDs, the electronic states can be understood as confined states in atoms or molecules where electrons are bounded in discrete energy levels formed in a three-dimensional confinement potential. It should be noted that due to Pauli's principle, only two electrons with different spins can occupy the same energy level. Therefore, in a QD, the density of state can be expressed like a delta-function, as illustrated in figure 2.2 (d), and the integration of the electron density gives two electrons in a certain quantum level. Moreover, as each QD exists in a spatially different position, each wavefunction is localized, which enables electrons to occupy the same energy level when the localized positions are different, like the impurity levels in a bulk semiconductor.

As a result, the width of the electron energy distribution could be zero as a first approximation. It means that injected electrons into those structures are distributed in certain discrete energy levels. In addition, the energy distribution width

is fundamentally independent of temperature. However, in real semiconductors, due to many interaction processes such as electron-electron and electron-phonon scattering, certain widths in the energy distribution appear; but those widths are expected to be much smaller compared to the fundamental distribution width of bulk ( $1.8 kT$ ) and QW structure ( $0.7 kT$ ). The electronic states in QDs have been recognized as the main reason for the improvement of device performance in semiconductors. When band-to-band transition is considered, its transition is mainly determined from the energy distributions of electrons. Therefore, the spectrum width in QDs should be less temperature sensitive compared to bulk structures or QWs.

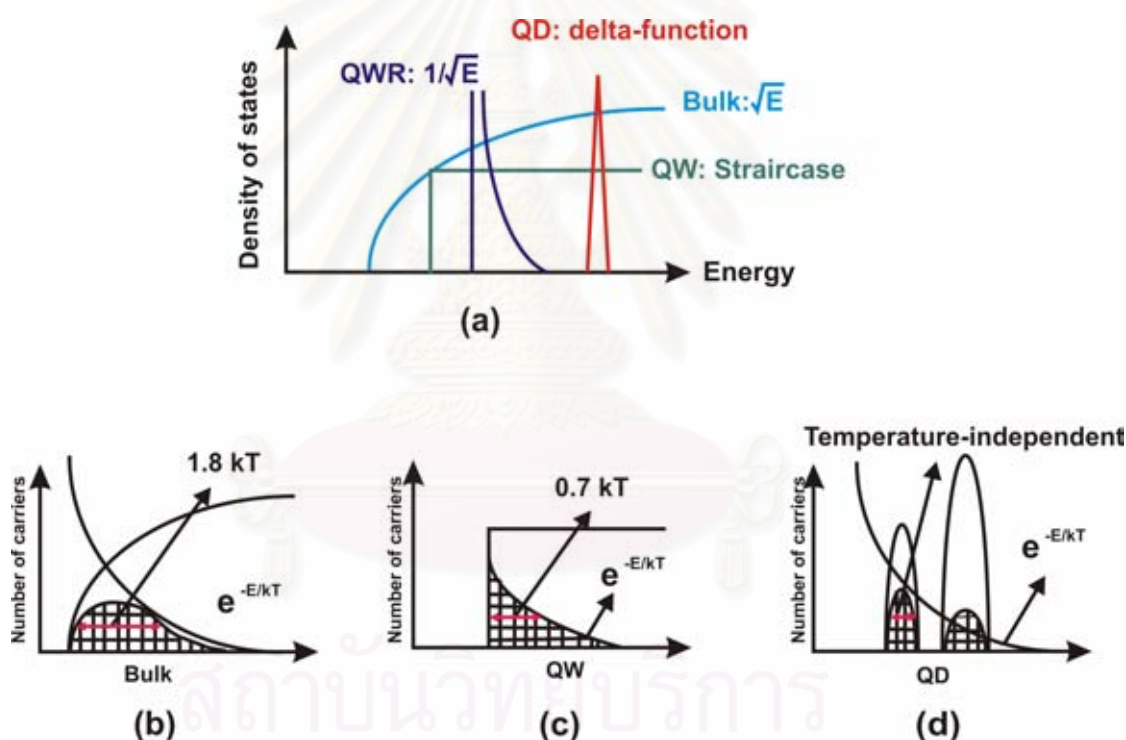


Figure 2.2 Illustrated of (a) density of states, (b) – (d) energy spreading under the low-carrier-limit condition in bulk material (b), QW (c) and QD (d). (Masumoto and Takagahara, 2002)

Significant quantum-size effects advantageous to optical devices appear when the size is less than the exciton Bohr radius, which controls how large a crystal must be treated as continuous. Therefore, the exciton Bohr radius can rightly be said to



define whether a crystal can be called a semiconductor QD, or simply a bulk semiconductor.

QDs are nanometer-scale semiconductor crystals with size-dependent optical, physical and electronic properties. One of techniques that can obtain dense packing with size uniformity on atomic scale is self-assembly, a novel way to fabricate QDs. The process exploits the three-dimensional island growth of highly lattice-mismatch heterostructure semiconductors. This thesis focuses on the growth of InAs on a GaAs substrate, where the lattice mismatch between InAs (larger lattice constant, 6.0584 Å) and GaAs (smaller lattice constant, 5.6533 Å) is about 7%. Dislocation-free high-density coherent islands of InAs having a dome or pyramid shape are self-assembled on the GaAs substrate, accompanied by a wetting layer (Seifert et al., 1996). InGaAs/GaAs islands grown via Stranski-Krastanow (SK) mode, as discussed below, were observed and evaluated by several groups in the mid-1980s (Schaffer, 1983; Lewis et al., 1984; Houzay et al., 1987). However, this topic did not attract broad interest until in the 1990s. Many groups, primarily researching on optical emission properties (Kamiya et al., 1998; Grundmann, 2000) have identified the islands as QDs with three-dimensional confinement.

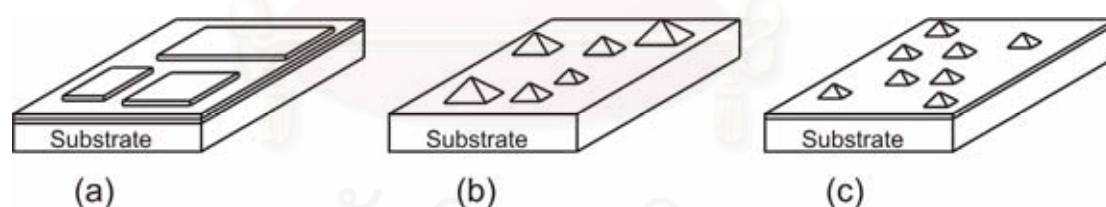


Figure 2.3 Schematic representation of the three crystal growth modes (a) Layer-by-layer or Frank-van der Merve; (b) island or Volmer-Weber; (c) layer-plus-island or Stranski-Krastanow mode. (Herman and Sitter., 1989)

It is generally known that there are three possible modes for crystal growth on the surfaces, schematically shown in figure 2.3. In lattice-matched heteroepitaxial systems, the energies of two surfaces and the interface energy are used to resolve the growth mode. If the sum of the surface energy  $\gamma_2$  of the epitaxial layer and the energy

of the interface  $\gamma_{12}$  is lower than the substrate surface energy  $\gamma_1$ ,  $\gamma_2 + \gamma_{12} < \gamma_1$ , 2D epitaxial layer-by-layer or Frank-van der Merve (FM) growth results, as illustrated in figure 2.3(a). Changing  $\gamma_2 + \gamma_{12}$  value more than  $\gamma_1$  may result in a transition from the FW to the Volmer-Weber (VW) mode where 3D islands are formed, as shown in figure 2.3(b). On the other hand, in a lattice mismatch heteroepitaxial system between the material being deposited and the substrate, a layer-by-layer growth mode is initially formed and followed by 3D islands. Because thicker 2D layer has a higher elastic energy, and the elastic energy tends to be reduced via formation of isolated islands due to the relaxation of elastic strain and decrease of elastic energy. This results in Stranski-Krastranow (SK) growth mode, as shown in figure 2.3(c).

In lattice-mismatched epitaxy, the formation of islands can be understood by a simple model of energy balance (Tu et al., 1992). The total energy between a coherently strained film on a substrate and strain-free islands made by the same number of atoms as in the film are compared. The total energy is supposed to consist of the strain energy due to lattice mismatch and the surface energy. For simplicity, the strain-free energy islands are assumed to be cubic shaped with a side length of  $X$ . Instead of releasing the strain energy, the cubic islands have greater surface energy due to the increased surface area. The island energy is lower than the film energy, when the island is larger than a critical value determined by the surface energy,  $\gamma$ , and the in-plane strain,  $\varepsilon$ , as

$$X > X_c \propto \gamma / \varepsilon^2 \quad (2.11)$$

When  $\varepsilon \neq 0$ , there is a value of  $X$  of the island which is in a lower energy state when the side length of the islands is greater than  $X_c$ , the island configuration will be favored. This is indicated that within sufficient growth temperature and time, islands are always formed in strained-layer epitaxy. From (2.11) equation, the critical size is inversely proportional to the square of the strain and as the lattice mismatch increases, the island size will be smaller.

Moreover, the strained-layer epitaxial growth using MBE enables us to obtain coherently strained layers over 1% lattice mismatch without dislocations under metastable conditions, which play an important role of surface kinetics.

## 2.2 Formation of quantum dots and strain effects on island nucleation

### 2.2.1 Lattice mismatch stress and Stranski Krastanow growth mode

In this section, the growth of heteroepitaxial lattice mismatched layer is considered. The dominant stress is associated with the lattice mismatch

$$\varepsilon = (a_L - a_S)/a_S \quad (2.12)$$

where  $a$  is the lattice constant and L and S denote layer and substrate, respectively. In that growth condition, for the first few monolayers, the deposited material will form in to 2D platelets which proceed in layer by layer mode until they merge with each other to complete 2-D epilayer. The accumulated elastic strain energy,  $E(el)$ , will increase linearly with the deposited volume, according to equation (2.12) (Seifert et al., 1996)

$$E(el) = \lambda \varepsilon^2 A t \quad (2.13)$$

where  $\lambda$  is the elastic modulus,  $\varepsilon$  is the dominant stress,  $A$  is the surface area and  $t$  is the film thickness. If the system keeps 2D growth, the energy will increase to be grater than the activation energy of dislocation process. On the other hand, if the growth conditions drive the system to the SK growth, the strain energy outweighs the surface energy. The system has to release the strain energy by change the growth mode from 2D to 3D growth mode, causing island formation (Srolovitz, 1989).

To discuss the nucleation and growth of self-assembled QDs, thermodynamics and kinetics are both involved.

### 2.2.2 Thermodynamically approach

An adequate description of self-assembled QDs formation should provide a detailed description of the equilibrium state supported by the dislocation-free strained system.

Considering the total energy of a single QD or island, the energy of a single islands,  $E_{\text{island}}$ , can be written as the sum of the elastic energy ( $E_{\text{elastic}}$ ), the surface energy of the island ( $E_{\text{surf}}$ ), and the island edge energy ( $E_{\text{edge}}$ ), as shown in Equation (2.14).

$$E_{\text{island}} = E_{\text{elastic}} + E_{\text{surf}} + E_{\text{edge}} \quad (2.14)$$

Shchukin et al. (1995) proposed a thermodynamic model which explains the narrow size distribution of the islands with an absence of Oswald ripening process by considering the energetics of an array of islands. The total energy change of the system due to the formation of a single island of a size  $L$  can be written as a sum of the following distributions (Shchukin et al., 2001)

$$\Delta E = -f_1 \lambda L^3 + (\Delta\Gamma)L^2 + f_2 \eta L - f_3 \frac{(\Delta\tau)^2}{\lambda} L \ln \frac{L}{a} \quad (2.15)$$

The first term is the energy of elastic relaxation,  $\lambda$  is a characteristic elastic modulus of the material; the second term is the change of the surface energy of the system; the third term is the short range contribution to the energy of the islands edges,  $\eta$  being the energy per unit length of the edge; and the fourth term is the energy of the elastic relaxation due to the surface stress discontinuity ( $\Delta\tau$ ) at the edges.  $a$  is lattice parameter;  $f_1$ ,  $f_2$  and  $f_3$  are geometrical factors depending on the island shape. The quantity  $\Delta\Gamma$  represents the energy change due to the appearance of the side facets, the disappearance of a certain area of the wetting layer, the appearance of the interface between the island and the substrate and the strain induced corrections to the surface energies; therefore,  $\Delta\Gamma$  can be positive or negative due to interplay between different

contributions. By assuming a fixed islands shape, the energy  $E(L)$  is given in figure 2.4. In the case of  $\Delta\Gamma > 0$ , the formation of a single island from a flat film causes an increase of the total surface energy, and the system has to reduce the energy to the minimum of  $E(L)$  which is located at  $L \rightarrow \infty$ , as shown in figure 2.4 indicating the ripening process. If  $\Delta\Gamma < 0$ , the formation of islands decreases the total surface energy and then causes the minimum energy  $E(L)$  located at a finite size of the island. There is no driving force for the ripening in this case, implying that there exists a stable island array with finite shape. This model is based on the scaling behavior of various contributions to the total energy, leading to a criterion for Oswald ripening or island formation.

Moreover, Shchukin et al. (1999) also found that either stable islands or ripening takes place in the system, depending on the material constants and misfit. However, by neglecting the existence of the wetting layer, their study could not predict the actual growth mode. Then, Daruka and Barabási (1997) proposed a model with free energy that considers  $Q$  monolayers (MLs) of atoms A with lattice constant  $a_A$  deposited on top of a substrate B with lattice constant  $a_B$ . Because of the lattice mismatch in equilibrium one expects that a certain fraction of atoms A forms a wetting film of  $Q_A$  MLs,  $Q_B$  monolayers are assembled in 3D coherently strained islands of a given pyramidal shape and volume, and the rest of the material ( $Q - Q_A$  MLs) is distributed in 3D coherently strain islands of a given pyramid-like shape and volume. And the rest of material B,  $(Q - Q_A - Q_B)$  MLs is assembled in ripen islands. The stability of the islands depends very sensitively on the coverage. For example, the misfit strain and coverage have to exceed a critical value for stable islands to exist, and that for any misfit there is a second critical coverage beyond which ripening occurs, as implied in equation (2.16) below.



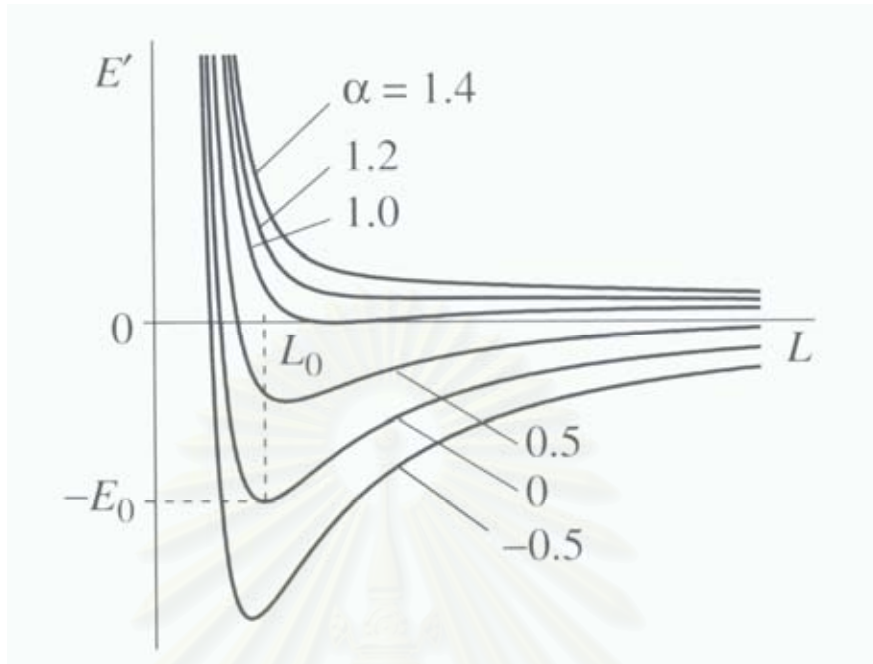


Figure 2.4 Energy of an array of 3D coherently strained islands per one atom versus island size  $L$ . The control parameter  $\alpha$  depends on the contribution from the surface energy and the edge energy (Bimberg et al., 1999).

By considering the possible coexistence of small islands of optimum size  $L_{opt}$  and of “ripened” islands considerably larger than  $L_{opt}$ , the total energy per unit cell of the substrate is

$$E = E_{WL}(Q_A) + Q_B E_{island}(Q_B) + (Q - Q_A - Q_B) E_{rip} \quad (2.16)$$

where  $E_{WL}(Q_A)$  is the energy of the wetting layer. Equation (2.16) defines the total energy of the wetting layer and 3D pyramidal islands, where the latter may exhibit *bimodal* behavior, i.e., both small islands of size  $L_{opt}$  and large islands considerably larger than  $L_{opt}$  may be presented in the system. By minimizing the energy from equation (2.16) with respect to  $Q_A$  and  $Q_B$ , Daruku and Barabási (1997) also obtain the equilibrium phase diagram of a lattice-mismatched heteroepitaxial system as a

function of the lattice mismatch  $\epsilon_0$  and of the total amount of the deposited material  $Q$ , as illustrated in figure 2.5.

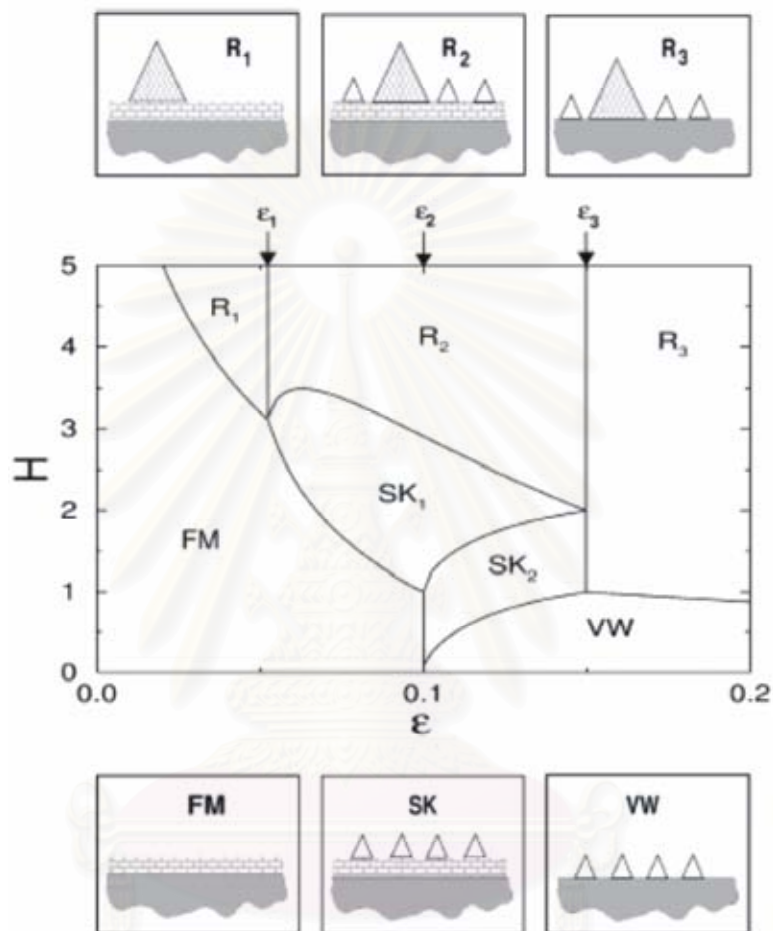


Figure 2.5 Equilibrium phase diagram as a function of the coverage  $H$  and misfit  $\epsilon$ . The small panels on the top and the bottom illustrate the morphology of the surface in the six growth modes. The small empty islands indicate the presence of stable islands, while the large shaded one refers to ripened islands. (Daruka and Barabási, 1997)

### 2.2.3 Kinetic approach

Several kinetic models of 3D island formation and of ordering have been proposed (Madhukar et al., 1994; Chen and Washburn, 1996, Barabási, 1997, Dobbs et al., 1997, Jesson et al., 1998). Such models take into account microscopic processes on the crystal surface like deposition, diffusion, attachment to islands, and detachment from islands.

Dobbs et al. (1997) formulated a mean-field theory for the density of adatoms in 2D and 3D islands. Three dimensional islands, as soon as they nucleate, act as traps for adatoms and atoms detaching from flat 2D islands. The increase in the density of 3D islands with increasing deposition of material is steep and saturates quickly. After this, additional material leads to no further increase in island density, but to an increase in the size of 3D islands. This model might be adequate for the initial stages of 3D island formation but does not predict any favored island size or narrow size distribution.

Seifert et al. (1996) proposed another kinetic aspect which can describe the limited size of QDs, the self-limiting growth. Figure 2.6 shows a schematic of the local strain energy density in and around a 3D island during the island formation. The change in the energy density due to the formation of 3D islands affects the chemical potential of the material at the surface. The minimum of the potential locates at the top of the island where the material partially relaxes, while the maximum is at the island edge, where the high compressive strain exists. The compressive strain at the edge propagates down to the substrate, increasing an inherent misfit between the substrate and the wetting layer around the island. Therefore, the high potential barrier around the island provides a zone, where the islands do not prefer to nucleate.

Madhukar et al. (1995) and Chen & Washburn (1996) pointed out the influence of strain fields created by islands on the motion of adatoms. Inhomogeneous strain fields in the vicinity of 3D islands act as repulsive forces, leading to the drift of adatoms away from existing islands and thus increasing the nucleation rate of new islands. In addition, smaller islands grow more rapidly than larger ones. Thus the above effects tend to equalize the sizes of the islands.

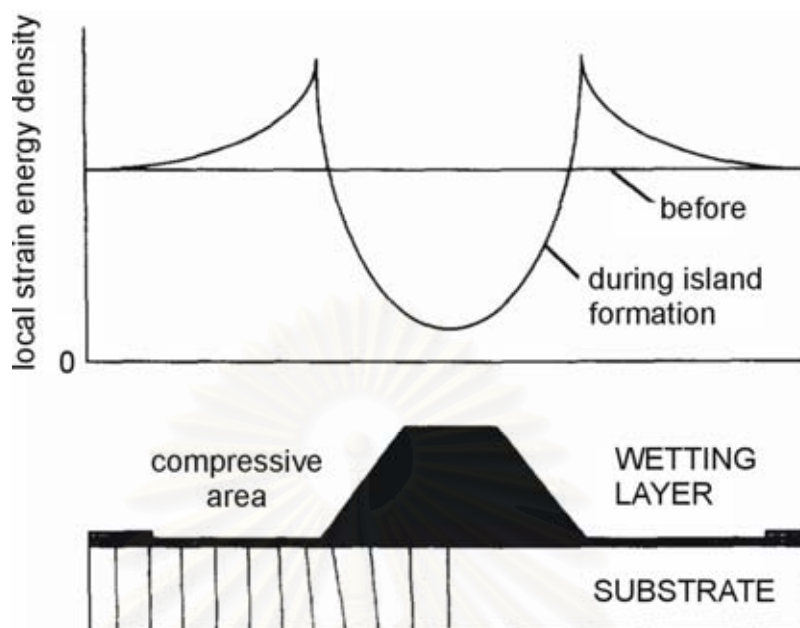


Figure 2.6 Schematic represent the local strain energy density in and around the QD. The energy barrier for the adatoms' diffusion to the QD has a maximum at the edge of the QD (Seifert et al., 1996).

Barabási (1997) has established a one-dimensional model using a Monte Carlo method including strain relaxation of the lattice at each step. This model takes into account the above impact of island-induced strain fields on the motion of adatoms, and eventually leads to a narrow size distribution for sufficiently large mismatch (5%). Increasing deposition leads mainly to a higher density of islands of the same size.

Jesson et al. (1998) emphasized the importance of nucleation of every new atomic layer in the growth of faceted islands. If an island has a shape with smooth facets which do not contain any steps or kinks, a new layer starts to nucleate at the edge between the island facet and the substrate, i.e., in a highly strained area. Strain provides a barrier for such nucleation, and the height of the barrier is larger for larger islands. This leads to self-limited growth and result in a narrow size distribution.

All of the above-mentioned kinetic theories imply that, in a system of 3D coherently strained islands, there is always a thermodynamic tendency towards Ostwald ripening but that it does not occur on an experimentally available time scale

due to various kinds of strain induced barriers. Such models seem to be relevant to particular experiments. However, there are experimental data on InAs/GaAs and GaInAs/GaAs islands which cannot be explained via kinetic concepts. At the same time, they can be described by the island formation with thermodynamic theory.

### 2.3 Spontaneous lateral alignment of QDs

Kitamura et al. (1995) demonstrated self-alignment of InGaAs QDs on GaAs multi-atomic step structure by MOVPE, as shown in figure 2.7. This technique gives rise to spontaneously aligned InGaAs QDs without any preprocessing techniques prior to growth. However, it is difficult for the (100)-misoriented surface to fabricate uniform and straight multi-atomic steps. On the other hand, a high-index surface is used for ordering of QDs due to decreasing the surface energy. Formation of straight QDs on (211)B and (111) substrates has been reported by Lee et al. (1998). Recently, Akiyama and Sakaki (2006) have reported the technique to grow dense and highly ordered arrays of self-assembled InGaAs quantum dots using molecular beam epitaxy along multiatomic steps on vicinal (111B) GaAs. By depositing a nominally 3-nm-

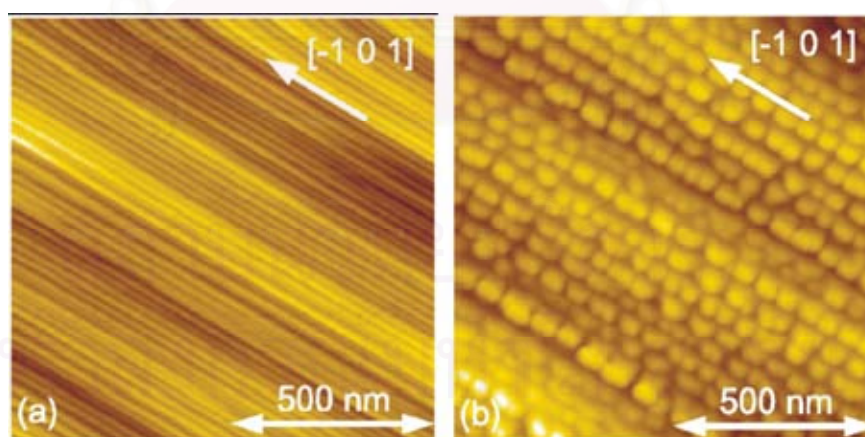


Figure 2.7 (a), (b) The AFM images of (a) multi-atomic steps on GaAs layer sample A grown on a vicinal (111B) GaAs, (b) InGaAs islands sample B prepared by depositing a nominally 3-nm-thick  $\text{In}_{0.3}\text{Ga}_{0.7}\text{As}$  layer onto multi-atomic steps of GaAs. (Akiyama and Sakaki, 2006)



thick  $\text{In}_{0.3}\text{Ga}_{0.7}\text{As}$  layer onto a periodically corrugated surface prepared on a GaAs substrate tilted  $8.5^\circ$  from (111B), QDs became aligned, as illustrated in figure 2.7(a) and 2.7(b), respectively.

## 2.4 Quantum dot self-alignment using vertical stacking

In order to increase the filling factor of QDs in a given sample, vertical stacking of layers containing QDs is important for most device applications. In addition, multi-stacking can be used to control initiation of islanding.

Upper islands tend to stack just on lower islands due to the strain field induced by the bottom islands that provides the stress on a crystal surface leading to the driving force for 3D island formation in lattice-mismatched growth. The first stack of islands produces a tensile stress in the capping layer above them, whereas a region having little or no stress may exist on the wetting layer. Another effect due to the integrated strain induced by repeated InGaAs/GaAs growth (superlattices, SLs), multi-stacking SLs enhances islanding. The strain is induced by lower-layer islands or In atom segregation from these islands affects subsequent islanding.

Figure 2.8 (Xie et al., 1995) shows a representative [011] cross-sectional TEM images of a five-stacked InAs QDs with GaAs spacers 36 ML thick. Figure 2.9 shows the experimentally observed pairing probabilities as a function of the spacer thickness. There are three regimes depending on the spacer thickness: (1) a regime for small spacer thickness, in which the probability is greater than 0.95, indicating a nearly completely correlated behavior; (2) a regime of gradual decrease in probability and (3) a regime for large spacer thickness, in which the probability saturates at a value corresponding to random overlapping of islands.

Based on the experimental data, Xie et al. (1995) have proposed a phenomenological model for vertical self-organization of InAs QDs separated by GaAs spacer layers. The kinetic process of vertically self-organized growth behavior is depicted in Figure 2.10. In the region I, QDs in the first stack produce tensile stress in the GaAs above the QDs. Whereas, region II, having little or no stress, may depend on the average separation  $l$  between the first stack of



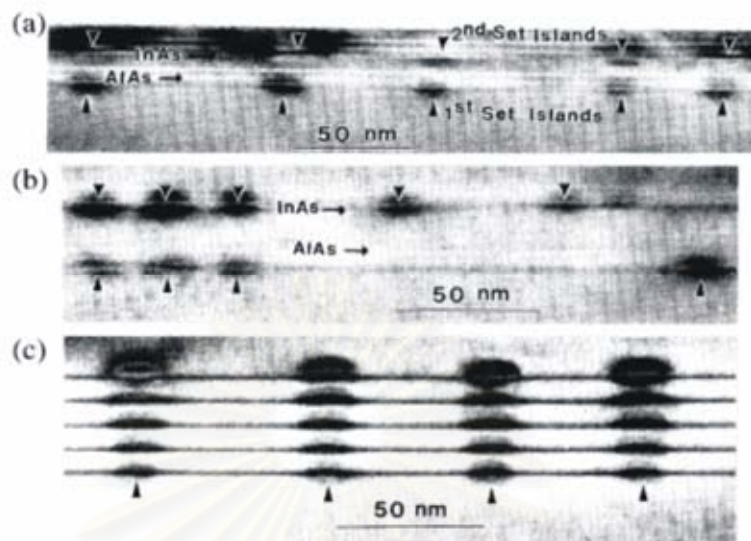


Figure 2.8 Typical  $g = (400)$  bright field TEM pictures taken along  $[011]$  azimuth for the samples with two sets of islands separated by (a) 46 and (b) 92 ML spacer layers, respectively. Arrows point to the island positions indicated by the strain contrast. (c) A typical  $g = (200)$  dark field TEM picture for a sample with five sets of islands separated by 36 ML spacer layers. (Xie et al., 1995)

QDs and the GaAs spacer layer thickness-dependent range of the surface strain field,  $l_s$ . The In atoms impinging in region I would be driven by the strain field to accumulate on top of the lower islands, where the atoms can also achieve a lower energy thermodynamic state due to lower lattice mismatch InAs with the GaAs in tension.

On the other hand, In atoms impinging in region II may initiate formation of QDs in region II, undesirable for achieving the most efficient vertical ordering. When the spacing layer is reduced, vertical self-assembly of QDs occurs. A characteristic spacer thickness for vertically self-assembled growth inferred from the model was found to be consistent with the experimental data.

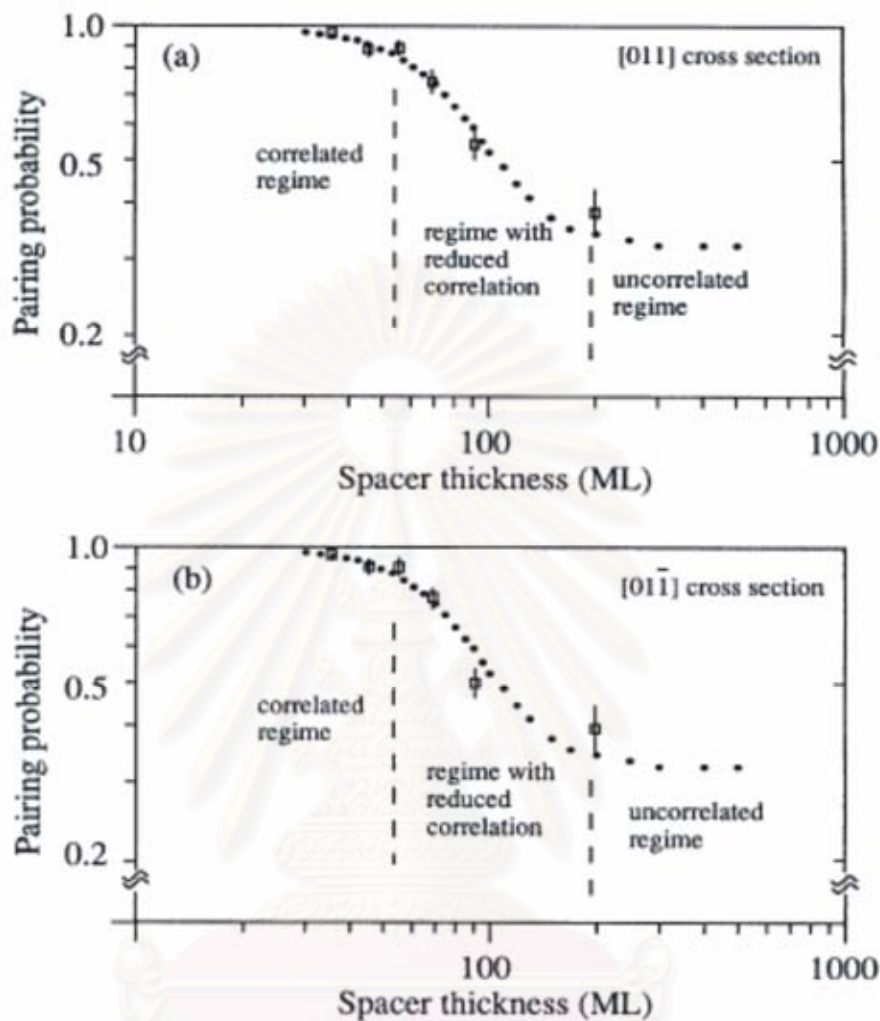


Figure 2.9 Experimentally observed pairing probabilities (open squares) as a function of the spacer thickness  $z_s$ , shown on a log-log plot for samples with two sets of islands (a) [011] cross section, and (b) [01 $\bar{1}$ ] cross section. (Xie et al., 1995)

Nakata et al. (1997) have reported the stacking of InAs QDs with GaAs intermediate layers of less than 3 nm thickness on (100) GaAs substrates by MBE. When QDs are closely stacked, the islands are electronically coupled and behave as a QDM. The wave function can be distributed along the vertical column.

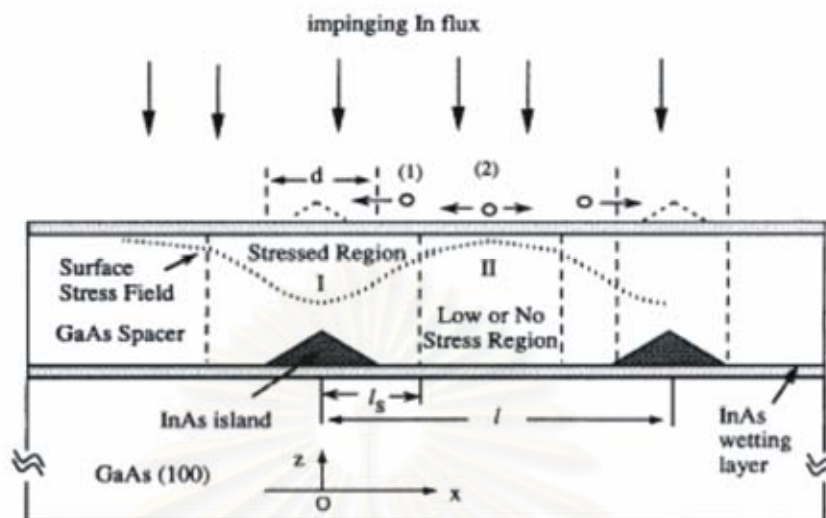


Figure 2.10 A schematic representation shows the two major processes for the In adatom migration on the stressed surface: (1) directional diffusion under mechanochemical potential gradient contributing towards vertical self-organization and (2) largely symmetric thermal migration in regions from the islands contributing to initiation of new islands not vertically aligned with islands below. (Xie et al., 1995)

## 2.5 Quantum Dot Molecules

Although a single QD has been demonstrated a quantum logic gate using the exciton-biexciton correlation, it has definite limitations for a large number of qubits. Consequently, a coupled QD system is essential for numerous qubits (Li et al., 2003). In coupled QD systems, there are two coupling mechanisms: quantum-mechanical coupling and electromagnetic coupling. In general, the quantum-mechanical coupling shows an exponential decay as a function of the interdot spacing. Whereas, the electromagnetic coupling exhibits at most a power-law dependence on the interdot spacing. Thus, electromagnetic coupling is more long ranged than quantum-mechanical coupling.

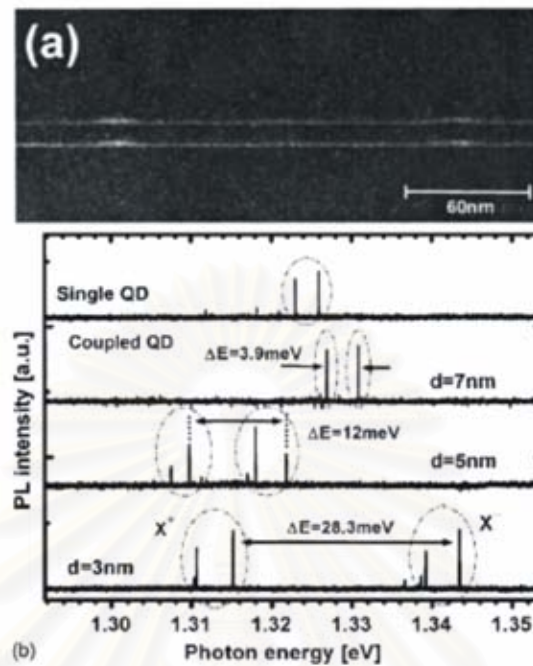


Figure 2.11 (a) Cross-sectional STEM image of the CQD sample with  $d=7$  nm. (b) PL spectra of a single pair of CQD with different barrier thicknesses at a low excitation intensity, where the excitation energy is 1.41 eV absorption band of wetting layer. The barrier thickness, bonding state, and antibonding state are labeled  $d$ ,  $X^+$ , and  $X^-$ , respectively.  $\Delta E$  indicates the energy separation between the  $X^+$  and  $X^-$  PL groups. The PL spectrum of a single layer QD sample is also shown at the top of figure for reference. (Yamauchi et al. 2005)

Yamauchi et al. (2005) have observed the interdot correlation in single pair of electromagnetically coupled QDs (CQD). Using the stacking growth technique, vertically coupled QDs with an arbitrary barrier thickness between two QDs have been observed as illustrated in figure 2.11(a). The notable feature of the CQD is that the energy separation between the two PL groups increases with reduction in the barrier thickness, as indicated by  $\Delta E$  in figure 2.11(b). This feature arises from the wave-function coupling of electrons between the upper and lower QDs, and these PL groups constitute the bonding  $X^+$  and antibonding  $X^-$  states, respectively. According to the arguments in the first paragraph at the beginning of this section, a QD pair with

a thicker barrier  $d=7$  nm is interpreted as being an electromagnetic, but weak quantum-mechanical, coupling system, because the electromagnetic coupling would be more relevant than the quantum-mechanical coupling for this interdot spacing. In addition, the reason why the  $d=7$  nm CQD does not have a pair of PL peaks could be that one of the pair of peaks is forbidden as a result of the strain distribution of the  $d=7$  nm CQD being different from those of other samples. An anomalous increase in the luminescence intensity has been observed when the two QDs are excited simultaneously. This remarkable finding can be interpreted in terms of the electromagnetic coupling between QDs with thick barrier layers.

In the case of quantum-mechanical coupling regime, quantum coupling in individual lateral CQDs or QDMs and its manipulation using static electric fields ( $E$  field) has been demonstrated. Vertical QDs along the growth direction were coupled in one dimension, whereas the lateral geometry enables coupling in two dimensions, and therefore, allows for an up-scaling to very large number of qubits. Figure 2.12(b) reveals the X1 and X2 peak emission energies plotted as a function of  $E$  field (Beirne et al., 2006). An anomalous redshift with respect to the interpolated peak energy expected from the shift on both the higher and the lower voltage side of each [dashed curves in figure 2.12(b)] have been observed. A similar anomalous Stark shift has been reported for vertically coupled QDs and is considered to provide strong evidence for the presence of quantum coupling between QDs (Oulton et al., 2005). This redshift is interpreted as a resonance between the electron ground states of the QDs and reflects the influence of tunneling processes that result in a redistribution of the electron wave function across both dots. Consequently, QDM can be used to create a wavelength-tunable single-photon emitter as described below. The prediction of the 1D model used to qualitatively describe the coupling mechanism is illustrated in figure 2.13. This model predicts that holes remain localized in the QDs, while electrons become almost entirely delocalized at the alignment bias, forming symmetric and antisymmetric states across the QDM. When applying more positive or negative  $E$  fields the model also predicts the observed switching behavior, i.e., the electronic ground state wave function can be transferred to either the larger or the smaller dot, enhancing the X1 or the X2 transition, respectively. Hence, the optical



transition rate of  $X1$  or  $X2$  can effectively be switched on or off, allowing for the deterministic emission of single photons at either the  $X1$  or the  $X2$  emission energy.

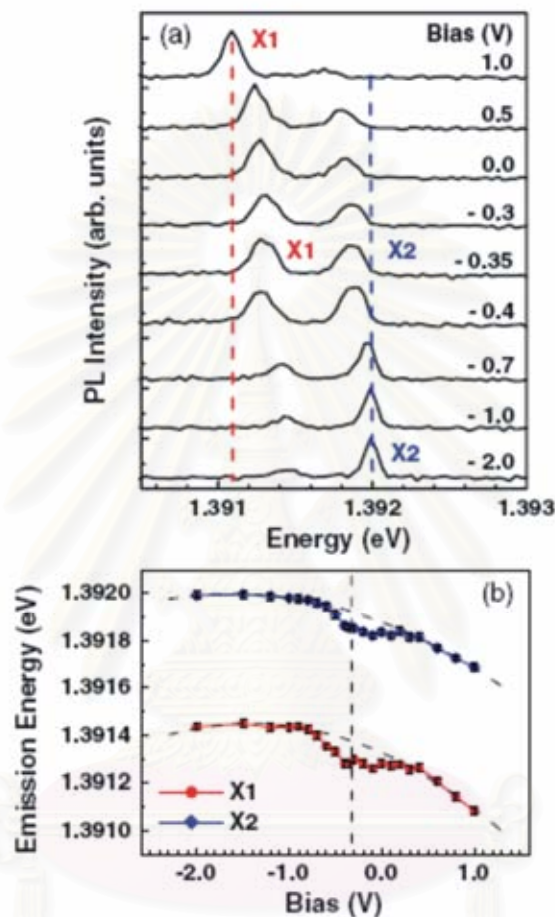


Figure 2.12 (a) QDM PL spectra at 4 K, and (b) the PL peak energy of  $X1$  and  $X2$  as a function of applied voltage along the QDM axis under pulsed excitation at 818 nm (1.52 eV) and a PD of  $200 \text{ W/cm}^2$ . A redshift is apparent at the alignment bias (dashed vertical line) indicating that the electron ground states of the two QDs are in resonance. The dashed curves are guides to the eye indicating the expected behavior without coupling. (Beirne et al., 2006)



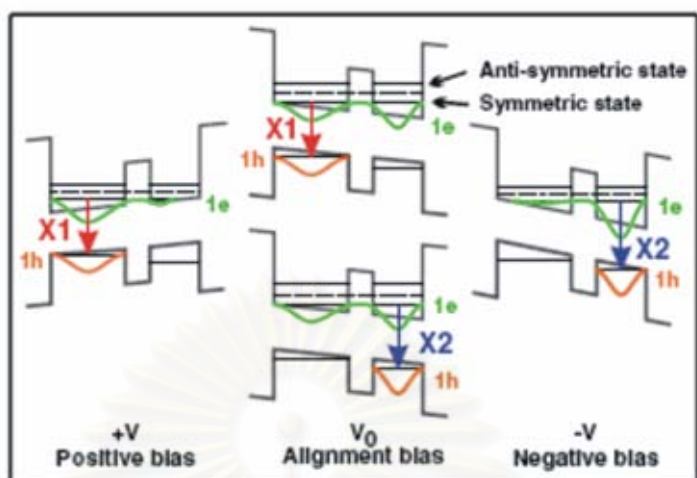


Figure 2.13 Schematic diagrams illustrating the predictions of the 1D model used to qualitatively describe the coupling mechanism and its control using an  $E$  field. (Beirne et al., 2006)

## CHAPTER III

### EXPERIMENTAL DETAILS

This chapter gives the experimental details of sample fabrication, which have been systematically conducted in this research work by molecular beam epitaxy (MBE). In-situ reflection high-electron energy diffraction (RHEED) has been used to monitor the epitaxial crystal layers during the growth process and to calibrate the growth rate and substrate temperature. The sample morphologies and their optical properties reflecting the crystal quality of their respective nanostructures were characterized by *ex-situ* atomic force microscopy (AFM) and photoluminescence (PL) spectroscopy.

#### 3.1 Molecular beam epitaxy

In this research work, both solid-source MBE and gas-source MBE have been used to fabricate samples having different quantum nanostructures. Hence, two MBE systems with different material sources and operations will be discussed in this chapter.

##### 3.1.1 Solid-source molecular beam epitaxy

Parts of samples were grown in a RIBER 32P solid-source MBE machine. This MBE system consists of four chambers: load-lock chamber, introduction chamber, transfer chamber and growth chamber. These chambers are separated by isolated gate valves and the samples are transferred from chamber to chamber by magnetic arm. In introduction chamber, there is heater used for heat treatment process (preheat) of the substrate in suitable conditions. A propose of preheat process is to remove contaminated substances, mostly water (H<sub>2</sub>O), from the substrate surface. The introduction chamber, transfer chamber and growth chamber are vacuumed by a titanium sublimation pump and an ion pump. The pressure is measured by ion gauge. After the preheat process, the sample is transferred to the manipulator in the growth

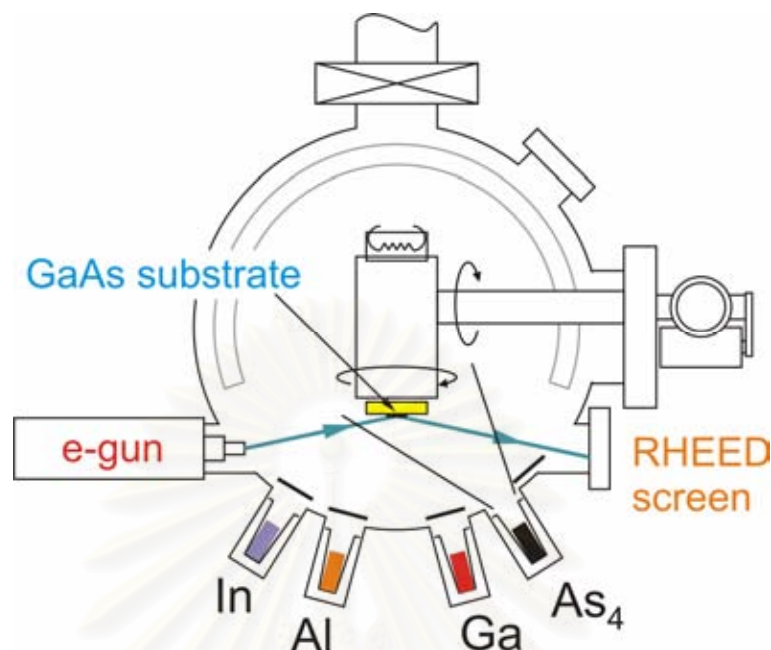


Figure 3.1 Schematic drawing of solid-source MBE growth chamber.

chamber via magnetic arm. A schematic drawing of the solid-source MBE growth chamber is shown in Figure 3.1.

The building blocks of this growth chamber composes of material source cells, substrate heater, monitoring equipment (for temperature, pressure, particle and surface analysis), and vacuum system.

The materials are contained in pyrolytic boron nitride (PBN) crucibles, installed in separated effusion cells, composing of In, Ga, Al as group III elemental sources and As<sub>4</sub> as a group V source. All cells were heated by heaters and the temperatures were measured by W-Re with 5% W or 26% Re thermocouples and controlled by computer via controller card (EUROTHERM<sup>TM</sup>). The beam flux is turned on and turned off by controlling of the molybdenum shutter position in front of each cell. The substrate is continuously rotated during the growth to provide uniform flux profile on the substrate surface. There are two ionization gauges in this chamber. The first one that located at equivalent substrate position behind the substrate heater is for beam flux measurement. Another one, which is installed in front of the ion pump, is for background pressure measurement. The quadrupole mass spectroscopy is used for the particles analysis in the growth chamber. The equipment for RHEED

investigation comprises a 20-kV electron gun, a fluorescent screen, a CCD camera, and a computer. The RHEED diffraction pattern generated by the sample surface is displayed on a phosphor screen and captured by CCD camera. A detail of the RHEED system will be presented in next section.

### 3.1.2 Gas-source molecular beam epitaxy

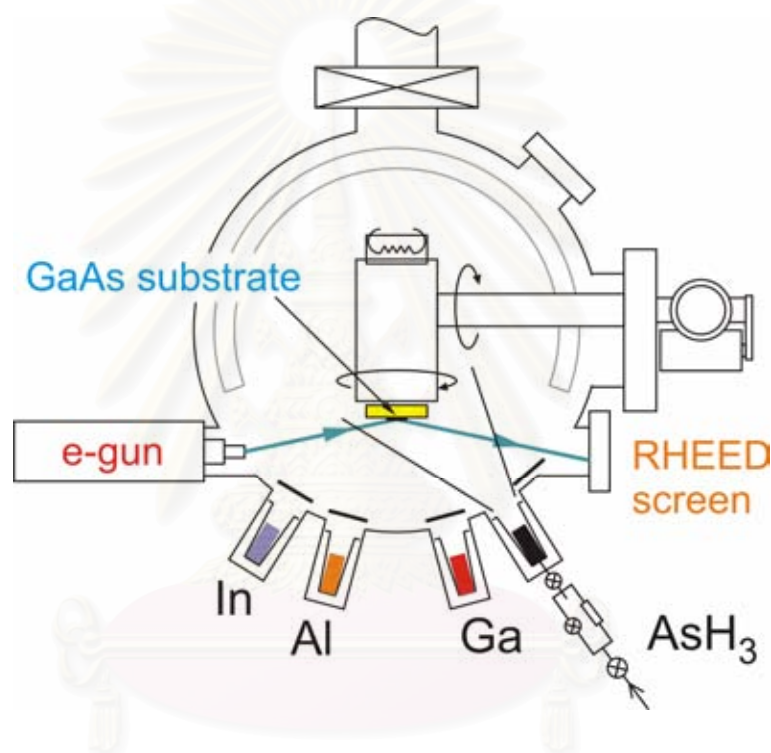


Figure 3.2 Schematic drawing of gas-source MBE growth chamber.

A schematic of the gas-source MBE system is shown in Figure 3.2. A Varian GEN-II MBE system was modified to handle group-V hydride gases. Two separate gas cabinets house  $\text{AsH}_3$  (100%) and  $\text{PH}_3$  (100%) as well as potassium permanganate ( $\text{KMnO}_4$ ) scrubbers. Both gases are introduced into the growth chamber through two cracking furnace around  $980^\circ\text{C}$ , and they are cracked into dimers and hydrogen before reaching the substrate. Besides the two gas crackers, there are five other furnace ports for solid Al, Ga, In, Si, and Be sources in the growth chamber. The fluxes of group-III sources (Al, Ga, and In) and dopant sources (Si and Be) are adjusted by the temperature of the effusion cells, and the fluxes of the group-V sources (As, P) are

controlled by mass flow controllers (MFCs). Pneumatic shutters in front of the furnaces are computer-controlled. All the sources and the rest of the growth chamber are surrounded by two liquid N<sub>2</sub> shrouds, for condensing background impurity molecules in the chamber in order to grow films with high purity. Two Ebara cryo-pumps with a pumping speed of 2200 l/s and one Pfeiffer TMU1600 model turbo-molecular drag pump with a pumping speed of 1500 l/s are used to pump the growth chamber. One cryo-pump and the turbo pump are used during growth, and the other cryo-pump is for idle status while the first one is being regenerated.

### **3.2 Reflection high-energy electron diffraction in molecular beam epitaxy**

Reflection High-Energy Electron Diffraction (RHEED) is a highly surface sensitive ultra-high vacuum technique used to monitor growth in MBE systems providing information on morphology and surface reconstruction.

Using the Ewald construction in the reciprocal lattice, the conditions for constructive interference of the elastically scattered electrons may be inferred. In the case where the electron beam essentially interacts with a 2D atomic net, the reciprocal lattice is composed of rods in reciprocal space in a direction normal to the real surface.

Figure 3.3 shows the Ewald sphere and reciprocal lattice rods for a simple square net. The reciprocal lattice rods have finite thickness due to lattice imperfections and thermal vibrations, and that the Ewald sphere also has finite thickness, in this case, due to electron energy spread and beam convergence. The radius of the Ewald sphere is very much larger than the separation of the rods. This can be verified from a simple calculation of electron wavelength.

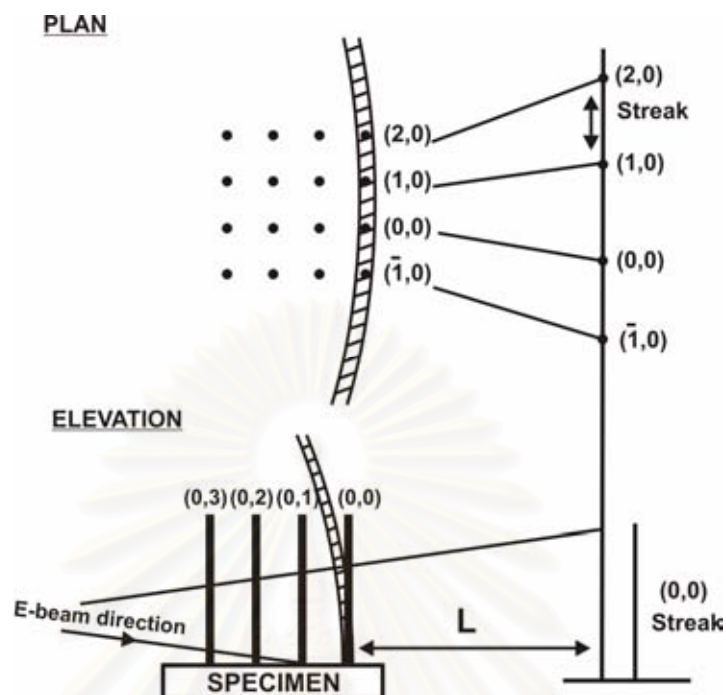


Figure 3.3 The Ewald sphere and reciprocal lattice rods for a simple square net. (Masumoto and Takagahara, 2002)

If the surface lattice net has a lattice constant of  $5.65 \text{ \AA}$  (unreconstructed) GaAs along the  $[100]$  direction, then the distance between adjacent rods in the reciprocal space ( $=2\pi/a$ ) will be  $1.1 \text{ \AA}$ . Electrons have a wavelength  $\lambda$  related to the potential difference  $V$  through which they have been accelerated by the equation

$$\lambda \sim \sqrt{\frac{150}{V(1+10^{-6}V)}} \quad [\text{\AA}] \quad (3.1)$$

From this equation,  $\lambda$  is  $0.12 \sim 0.06 \text{ \AA}$  when  $V$  is  $10 \sim 50 \text{ kV}$ .

Using this calculation, it follows that the radius of the Ewald sphere is  $36.3 \text{ \AA}$ . As a result, the interaction of the sphere and rods occurs some way along their length, resulting in a streaked rather than a spotty diffraction pattern, as shown in Figure 3.4.



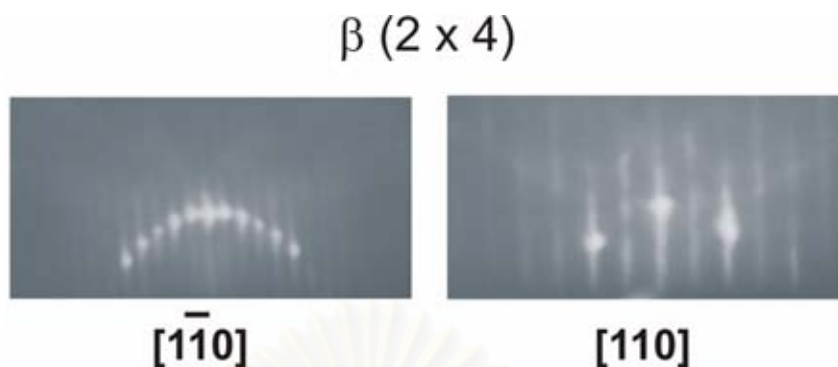


Figure 3.4 Observed RHEED patterns of GaAs(100)-(2×4) surface reconstruction.

Real semiconductor surfaces are more complex and their detailed structure must be inferred from diffraction patterns taken at different azimuths. The polar surfaces of GaAs such as the (100) and (111) planes have an excess of Ga or As atoms, depending on growth conditions or postgrowth treatment. The different reconstructions of this surface are related to its variable stoichiometry, and several attempts have been made to determine the effective As coverage as a function of the particular reconstruction. It is generally agreed that both the (2×4) and c(4×4) structures being As rich, with the latter having the higher As coverage, are stable on the GaAs (100) surface. For the (2×4) structure, a comparison between theoretical and experimental results gives strong evidence for the presence of asymmetric As dimers in the surface layer, as shown in Figure 3.5. An energy minimization approach for the c(4×4) surface based on the assumption that this surface is stoichiometrically As-terminated suggests an equal number of symmetric and asymmetric As dimers. It is immediately clear from the three low-index azimuth patterns that the surface has a c(4×4) structure and this symmetry is maintained over a wide range of as exposure. From these results, RHEED pattern has been used to calibrate the substrate temperature. Figure 3.6 shows the RHEED pattern that change from (2×4) to c(4×4) by ramping the substrate temperature down and up and then record the transition temperature  $T_1$ ,  $T_2$ ,  $T_3$ , and  $T_4$ . The average temperature of  $T_1$ ,  $T_2$ ,  $T_3$ , and  $T_4$  is defined as 500°C.

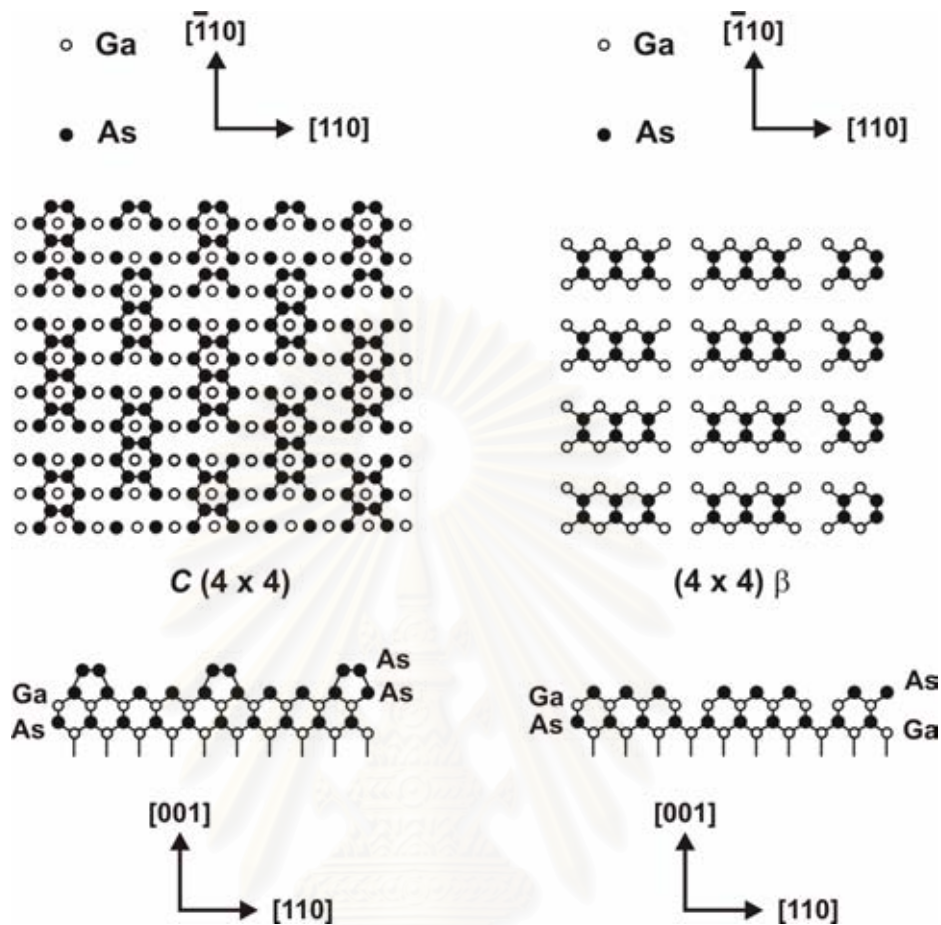


Figure 3.5 Schematic crystal arrangement of surface reconstruction on GaAs (100) surface. (Masumoto and Takagahara, 2002)

Moreover, the RHEED pattern has been used to calibrate the growth rate. Figure 3.7 reveals a real-space representation of the formation of a single complete layer, which illustrates how the oscillation in the intensity of the specular beam occurs (Reinhardt et al., 1994). There is a maximum in reflectivity for the initial and final smooth surfaces and a minimum for the intermediate stage when the growing layer is approximately half complete. In early stages, one layer is likely to be almost complete before the next layer starts so the reflectivity increases as the surface again becomes smooth on the atomic scale, but with subsequent surface roughening as the next layer develops. This repetitive process causes the oscillations in reflectivity gradually to be damped as the surface becomes statistically distributed over several incomplete atomic levels.

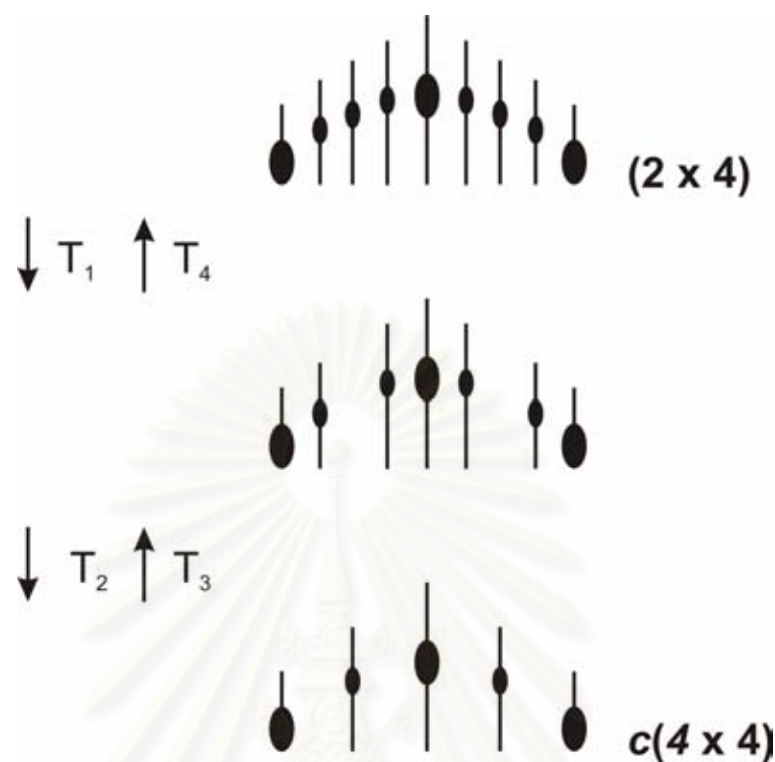


Figure 3.6 RHEED pattern to observe transition temperature from  $(2 \times 4)$  to  $c(4 \times 4)$ .

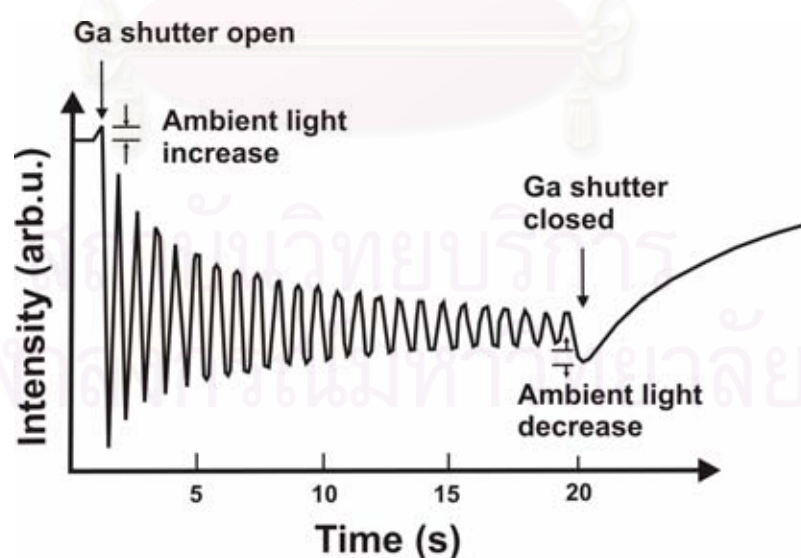


Figure 3.7 Intensity oscillations of the specular beam in the RHEED pattern from a GaAs(100)- $(2 \times 4)$  reconstructed surface,  $[011]$  azimuth. (Masumoto and Takagahara, 2002)

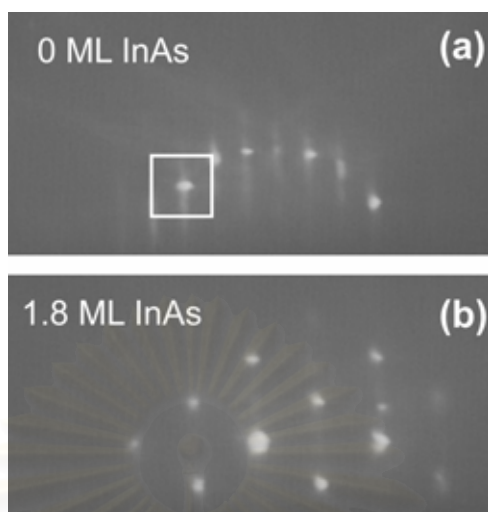


Figure 3.8 Observed RHEED patterns during InAs growth.



Figure 3.9 Two typical oblique streaks starting from the same reciprocal lattice point. (Masumoto and Takagahara, 2002)

In principle, the RHEED in MBE system enables the response of a growing surface to be monitored easily and continuously to provide information on morphology and structure. Upon transformation of an initially 2D ordered surface with monolayer-high islands into a corrugated structure, the RHEED pattern changes from streaky to spotty. Figure 3.8 shows the RHEED patterns observed during InAs growth. Since streak patterns can be seen in Figure 3.8 (a), the surface is flat before InAs growth. When 1 ML of InAs was grown, the streak patterns remained. However, when 2 ML of InAs were grown, the RHEED patterns changed from streaky to spotty, indicating that InAs grows three-dimensionally, as shown in chevron shape in  $[1\bar{1}0]$ . The angle between two streaks starting from same reciprocal lattice point is about  $55^\circ$ , as illustrated in Figure 3.9. On the other hand, no

specific facets can be observed with the incident electron beam along the [110] direction.

### 3.3 Photoluminescence

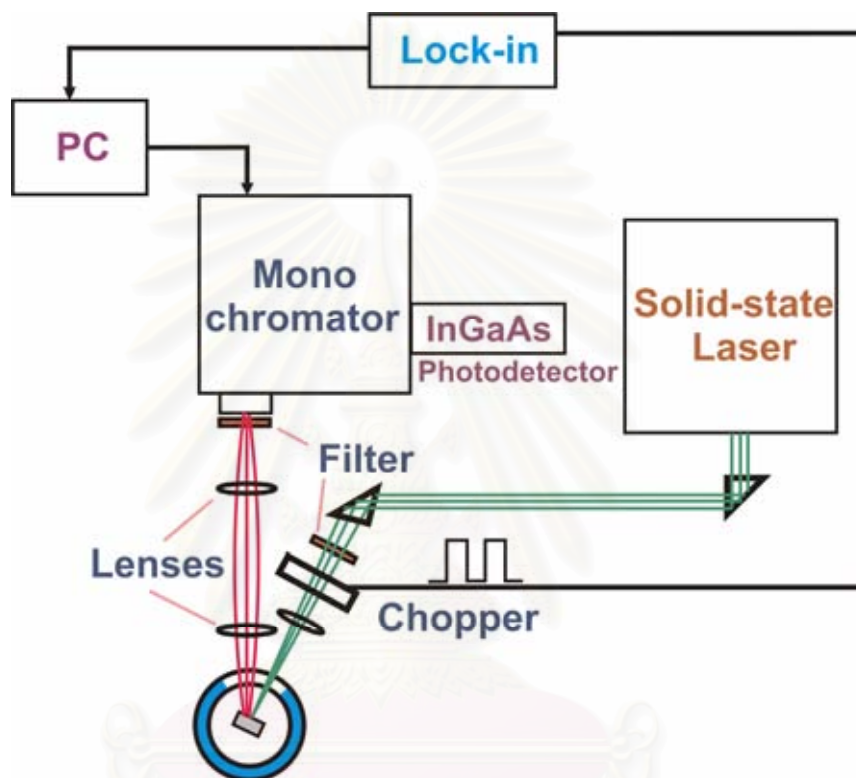


Figure 3.10 Schematic of the PL experimental set up.

The main tool for optical characterization in this research work is the photoluminescence (PL) spectroscopy. Photoluminescence is a sensitive way to characterize the optical properties of semiconductors. By observing the photon emission associated with transitions from the optically excited states, the bandgap energy of a material can be easily determined. A schematic of the PL experimental set up is shown in Figure 3.10. The samples were excited by the 514-nm line of an  $\text{Ar}^+$  laser. The light signal is resolved by a 1-m monochromator. Typically, the entrance and exit slit widths are 0.5 mm. The resolved light signal is detected by a liquid- $\text{N}_2$ -cooled InGaAs detector (Hamamatsu's G7754-01 with  $0.1\text{-mm}^2$  active area). A chopper and the lock-in amplifier are used to enhance the signal by the



standard lock-in technique. For low temperature measurement and temperature dependent, the sample was mounted on the cold finger of a closed-cycle cryostat.

The PL results attribute from the fact that the ground-state PL peak energy gives information about the size of QDs. Lower quantized energy levels of holes and electrons are obtained when increasing in QD size.

From the QD array, the shape of PL spectrum exists broadening which is measured in terms of a full width at half maximum (FWHM) related to the QD size uniformity, as illustrated in Figure 3.11. From the theory about single QD (see Figure 3.12) as discussed in chapter 2, the PL linewidth corresponds to the delta-function-like density of states. But in case of self-assembled QDs, there are large numbers of excited QDs having different sizes leading to broaden PL spectrum. The PL linewidth is inferred to determine the homogeneity of the QD.

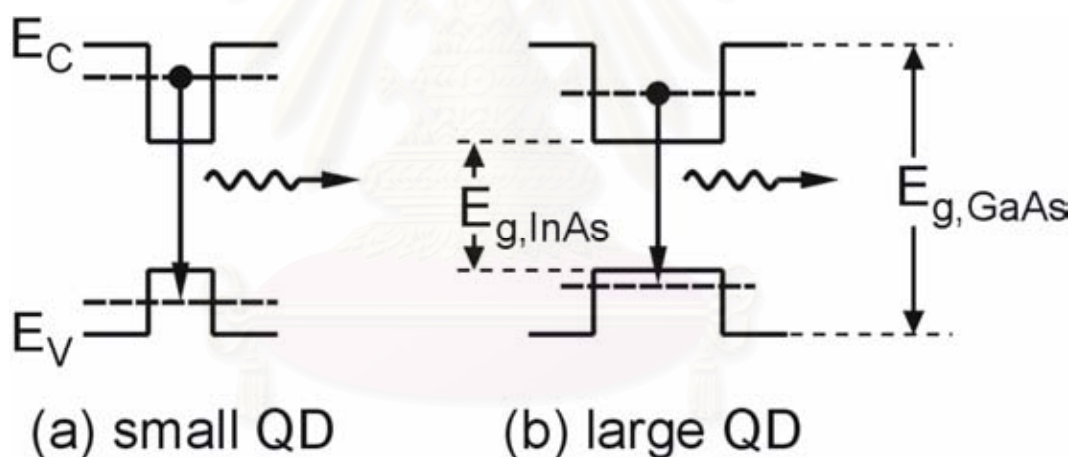


Figure 3.11 Simple interpretation of the PL data obtained from a QD structure. In case of small QD (a): the PL peak energy position is higher compared with large QD (b). (Kiravittaya, 2002).



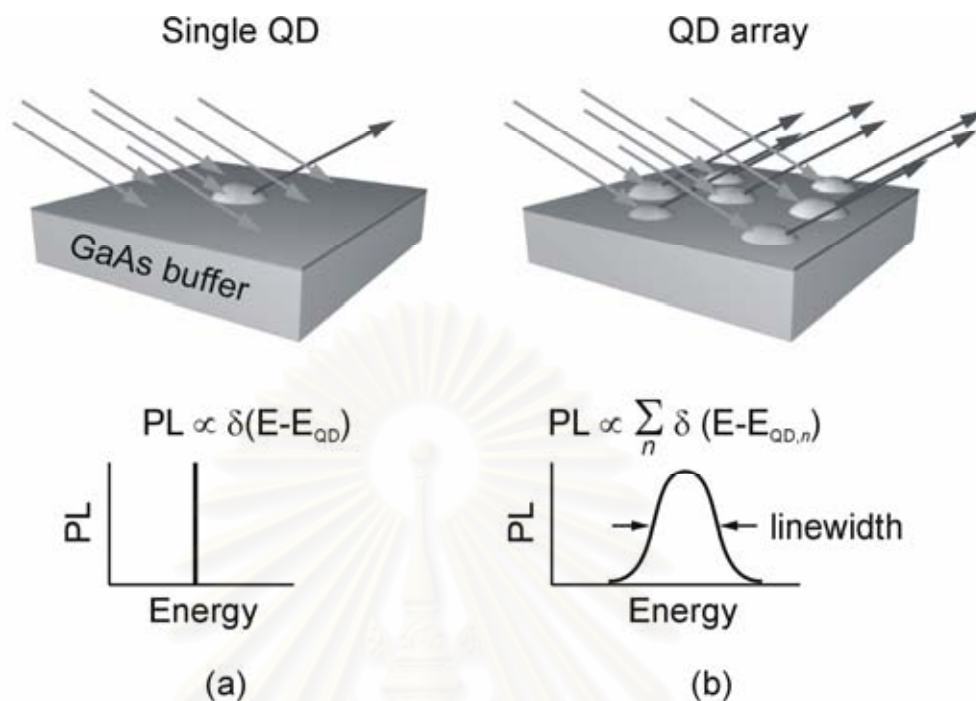


Figure 3.12 Simple interpretation of the PL spectrum obtained from the QD structure. In (a) the PL spectrum is very narrow due to the delta-function like density of states; and in (b) the average dot size corresponds to the PL peak energy position and the PL linewidth corresponds to the size distribution of the array. (Kiravittaya, 2002).

### 3.4 Atomic force microscopy

The surface morphologies of all samples were observed by Atomic force microscopy (AFM). The AFM is performed by using two brands of AFM machines. First one is SEIKO SPA 400 which is operated in the non-contact mode. Another one is DIGITAL INSTRUMENT (DI) Nanoscope IIIa using in the tapping mode. Figure 3.13 represents a schematic of AFM when operated in the tapping mode. As the cantilever bounces vertically, the reflected laser beam, which reveals information about the vertical height of the sample surface, is deflected in a regular pattern over a photodiode array, generating a sinusoidal electronic signal. The scan rate is around 0.8 Hz and the scan size is usually  $2 \times 2 \text{ um}^2$ . The number of data per scan line is 512. The vertical resolution of this measurement is usually in the subnanometer range.

Therefore, in this work we only use the height distribution of the QD arrays obtained from analysis of the AFM images to determine the size homogeneity of the QDs.

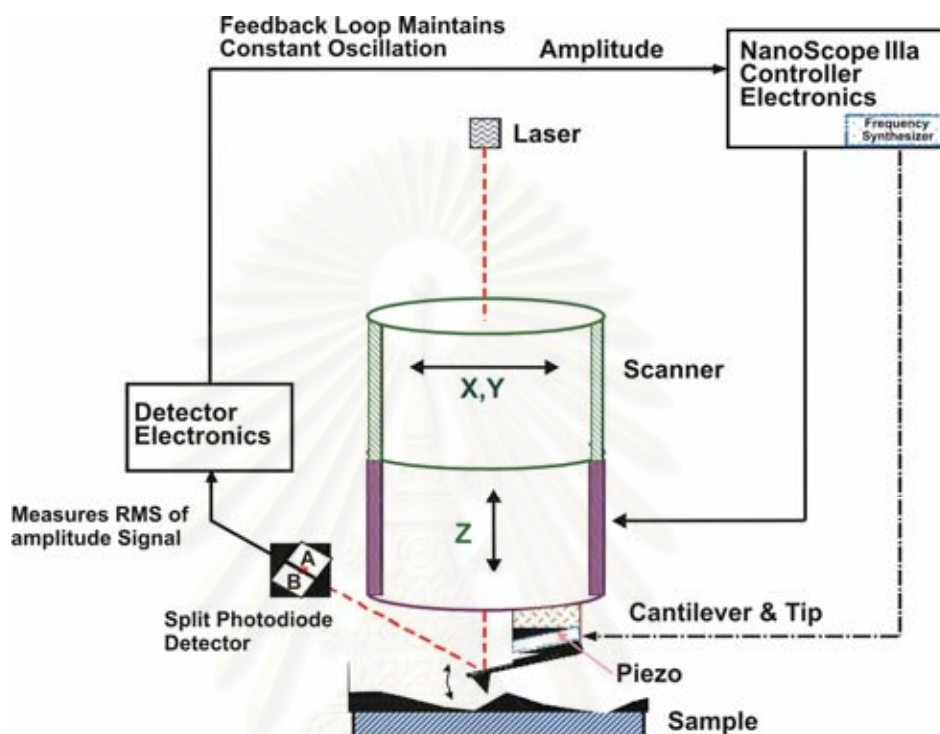


Figure 3.13 A schematic of AFM system when operated in tapping-mode.

### 3.5 Sample preparation

The details of investigated samples are as follow. All samples were grown on epi-ready semi-insulating (001) GaAs wafers. In the first step, the samples are preheated in the introduction chamber at the temperature ranging from 30°C to 450°C and are remained in this temperature for an hour in order to determinate the wafer from water (H<sub>2</sub>O) and other contamination. Then, the temperature of the samples is ramped down to 30°C before transferring the samples into the growth chamber. In the second step, the surface oxide layer is removed at 610°C for 15 min, under arsenic pressure, before the growth of buffer. Next, a 300-nm thick GaAs are grown at the temperature of 580°C for a buffer layer to flatten the surface. The growth rate of GaAs is 0.6 ML/s and 0.01 ML/s for InAs. After that, the desired structures are

grown. Then, a 20-nm thick GaAs are deposited at 500°C. And another 130-nm thick GaAs are grown and simultaneously the substrate temperature is ramped from 500°C to 580°C in order to minimize the effect of surface state for photoluminescence investigation. Finally, a similar structure is grown again on the surface and then the substrate temperature is cooled down immediately to room temperature to keep the surface structure for *ex-situ* AFM characterization. The schematic of sample structure grown for this work is shown in Figure 3.14.

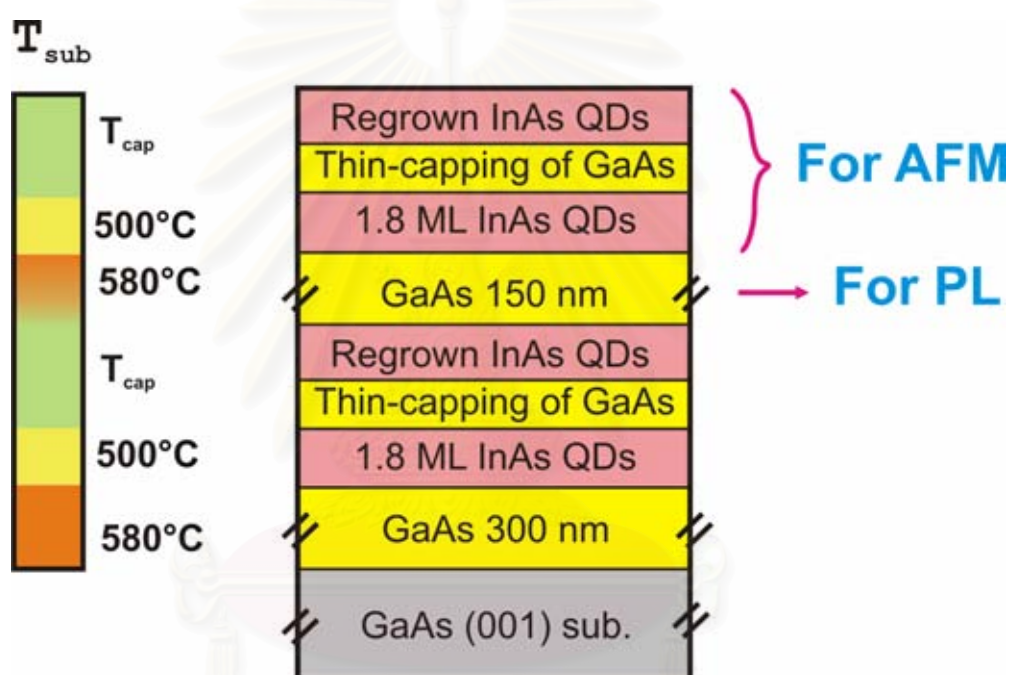


Figure 3.14 Schematic of sample structure.

## CHAPTER IV

### PARTIAL-CAPPING-AND-REGROWTH TECHNIQUE WITH SOLID-SOURCE MOLECULAR BEAM EPITAXY

Numerous challenges in QD fabrication have been reported during the last few decades. The most straightforward technique is to pattern the QD structures through a combination of high-resolution electron beam lithography and dry or wet etching. Other techniques exploit regrowth of epitaxial layers, such as fractional layer growth on a vicinal substrate, and cleaved-edge overgrowth. However, artificial structures fabricated in these ways did not take full advantage of engineered energy states and some had drawbacks to cause damage to the crystals, such as impurity contamination, defect formation, and poor interface quality. Therefore, self-assembly, a novel way to fabricate QDs is now the most promising approach in overcoming the various problems. Our growth technique, partial-capping-and-regrowth, is based on self-assembly technique used to grow In(Ga)As nanostructures. After being partially overgrown with GaAs (partial capping), as-grown QDs change to a camel-like nanostructure. Then, when additional InAs is deposited (regrowth), camel-like nanostructures turn into QDMs with 4-12 dots per QDM depending on the growth condition.

#### 4.1 Self-assembled InAs quantum dots

The technique exploits the three-dimensional island growth of highly lattice-mismatched semiconductors. The growth of InAs on a GaAs substrate has lattice mismatch between InAs and GaAs of about 7%. Dislocation-free, high-density coherent islands of InAs are self-assembled on the GaAs substrate, accompanied by a wetting layer with the Stranski-Krastranow (S-K) growth mode. Typical InAs self-assembled islands have a dome or pyramid shape with a base length of about 40 nm

and height of 10 nm for an InAs growth rate of 0.01 ML/s at the regrowth temperature of 500°C.

In Kirvittaya's thesis (Kiravittaya, 2002) and Songmuang's thesis (Songmuang, 2003), they report the effects of growth conditions of InAs QDs. First, the amount of deposited InAs is varied. For InAs thickness less than 1.0 ML, the formation of small 2D islands (called platelets) with a few ML height are obtained. A transformation of the 2D islands into 3D islands is observed when InAs thickness is further deposited to 1.7-1.8 ML and then QDs are formed. If the deposited InAs is more than 1.8 ML, some QDs are larger. The size homogeneity decreases and the Oswald ripening takes place. Next, the effects of varying the growth rate are observed. Increasing the growth rate, the dot density increases with reduced dot size. The effect of the growth rate on QD size can be explained by the different linear scale for island formation (Seifert et al, 1996). For a higher growth rate, a narrow time interval during the island formation results in less material diffusion as well as smaller diffusion length.

Furthermore, the effects of growth interruption after QD formation have been studied (Kiravittaya, 2002). From the PL spectra of 1.8 ML InAs QDs using low growth rate with 0, 30, 60, and 120 s growth interrupt, we find that the linewidth of 30 s growth interruption is the narrowest. By the local surface strain energy density contribution to the surface chemical potential (Seifert et al., 1999), the linewidth narrowing corresponds to and improvement in size homogeneity. Further depositing indium atoms after the InAs wetting layer formation causes nucleation of 2D islands. As shown in figure 4.1, 3D island formation that behaves like a material sink for indium adatoms is induced by increment in size to larger than the critical size of 2D islands. During the growth interruption, thermal activation causes indium atom detachment from the remaining InAs clusters. Then, In adatoms diffuse on the surface. Therefore, the InAs clusters disappear after early growth interruption. Moreover, due to the lower potential barrier of smaller QDs, the homogeneity of QDs is improved, as shown in figure 4.1(b). For further increase of the growth interruption time after the disappearance of InAs clusters leads to a decrease of dot homogeneity due to thermal activation energy. Some atoms may be desorbed giving rise to the broadening of the PL linewidth of the QDs with more than 30 s growth interruption,



as illustrated in figure 4.1(c). This desorption process causes the strain energy to decrease, and consequently In atoms from the QD can diffuse out of the QD. This desorption results in the decrease of the QD size leading to worsening of homogeneity.

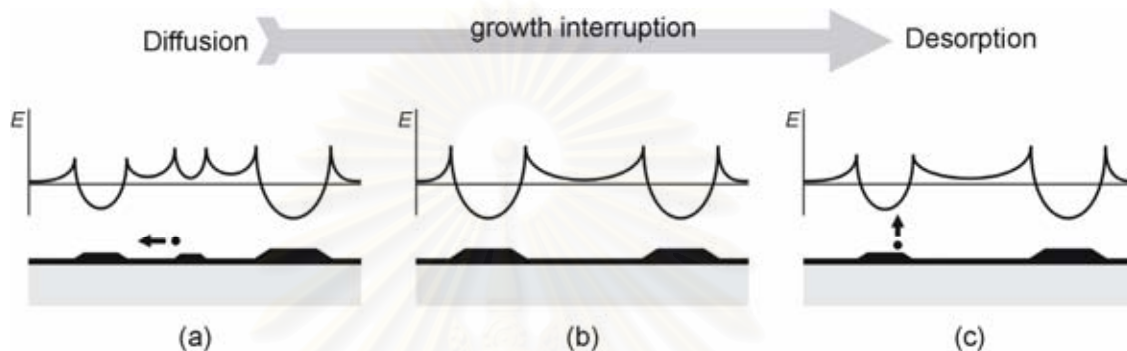


Figure 4.1 Schematic representation of atomic processes occurring during GI. The curves correspond to the local surface strain energy density. (a) the InAs cluster is less stable, hence leading to the detachment of indium atoms from the clusters to the smaller InAs QD. (b) The diffusion process improves the size homogeneity of QD ensembles. (c) Indium atoms from the QDs start to desorb when the GI time is increased. (Kiravittaya, 2002)

## 4.2 Partial-capping-and-regrowth process

### 4.2.1 Capping Process

In this thesis, as-grown QDs are partially capped at a relatively low temperature (470°C) with 6 ML of GaAs (1.67 nm) for the partial capping process. A camel-like nanostructure is observed with a nanohole on top of the dot as shown in figure 4.2. The nanohole has a depth of 0.7 nm with respect to the dot height level. The diameter of the nanostructure is around 190 nm in the  $\langle 1\bar{1}0 \rangle$  crystallographic direction, and approximately 50 nm in the  $\langle 110 \rangle$  direction.

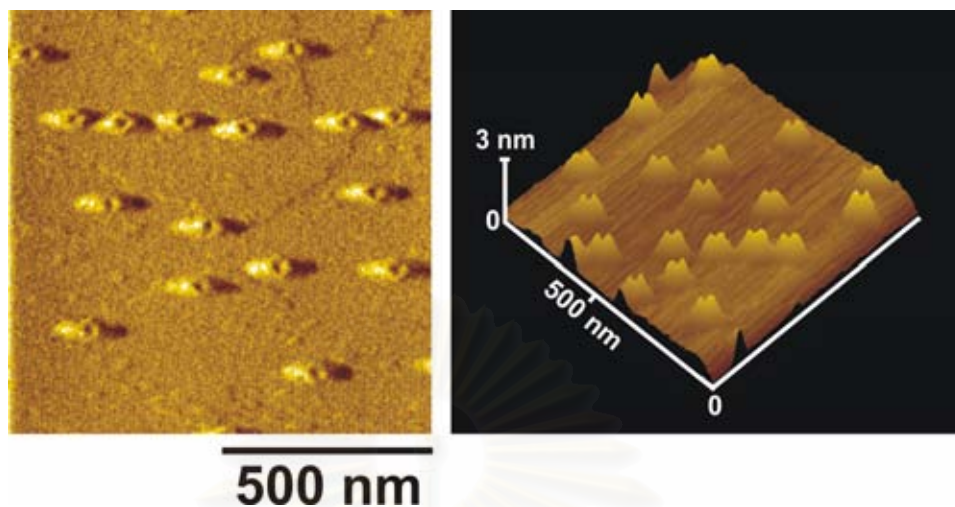


Figure 4.2 Planview (left) and oblique angle (right) AFM images of camel-like nanostructures with a nanohole on top of the dot.

Figure 4.3 represents a schematic of the evolution of the morphological features. 1.8 ML as-grown QDs are formed on the surface with 30 s growth interruption. After partially capped with GaAs at low temperature, intermixing of Ga and In forms a non-uniform InGaAs layer on both the wetting layer and the perimeter of QDs. Further depositing GaAs, the Ga adatoms prefer not to grow on top of the QDs due to highly relaxed InAs at these areas. Moreover, the surface curvature drives the Ga adatoms out of the convex surface. The relaxation of InAs on the QDs compresses the lattice spacing of the wetting layer around the QDs leading to preferential growth of GaAs around InAs QDs. Besides, the effect of anisotropic diffusion length of Ga adatoms gives rise to the formation of camel-like nanostructure with nanoholes on top, as shown in figure 4.2. For further deposition of GaAs, the strain field from the InAs QDs decreases, and the surface is flattened due to adatom diffusion.

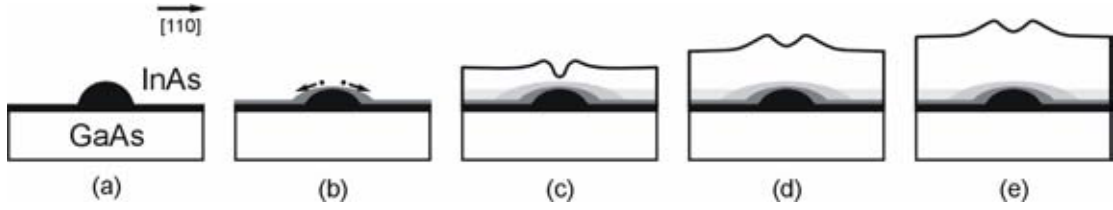


Figure 4.3 Schematic illustration of QD capping at low temperature. (a) A free-standing InAs QD. (b) The QD collapses during capping with thin GaAs. The indium atoms detach from the QD and diffuse to intermix with GaAs on the flat GaAs surface. Due to less intermixing with the low temperature capping, the indium compositional profile induces non-preferential growth on the top of the QD (c). The effects of the compositional profile are less pronounced for thick capping layer thicknesses (d) and (e). (Kiravittaya, 2002)

Moreover, Wang et al. (2001) have studied the redistribution of partially covered InAs islands into a second fractional wetting layer. Their study is based on a thermodynamic equilibrium consideration. The total energy ( $E^{tot}$ ) is calculated by decomposing it into contributions from elastic strain of the pseudomorphic island and the surrounding substrate and capping layer,  $E^{elast}$ ; from the surface energy of the facets of the island and the interior walls of the holes,  $E^{surf}$ , and from the second wetting layer,  $E^{wl}$ ;

$$E^{tot} = E^{elast} + E^{surf} + E^{wl} \quad (4.1)$$

The energetic of the transformation process from three-dimensional clusters to a wetting film of InAs is determined by both the elastic energy relief and the changes of the surface energy. The material gradually diffuses away from the island via surface diffusion and forms a homogeneous wetting layer with increasing thickness on the GaAs capping layer. Contributions to the energetic that drives the transformation process come from the elastic energy relief, as well as from changes in the surface and interface energy.

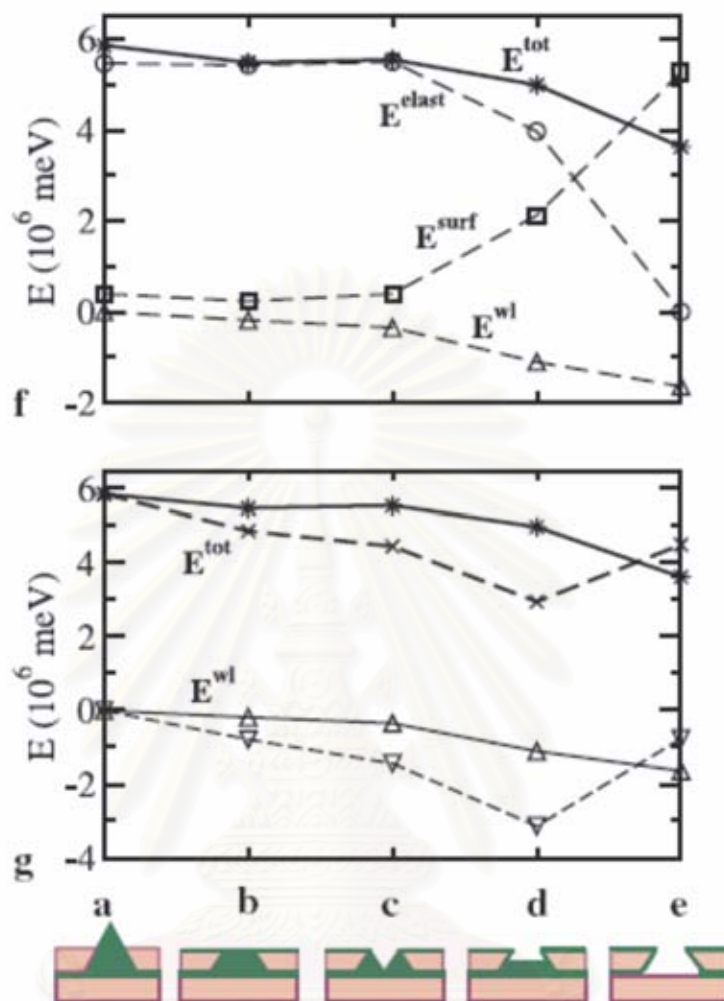


Figure 4.4 (a)-(e) Schematic of the transformation from a large InAs island partially overgrown by a GaAs capping layer to a hole in five steps. (f) The energetics in the case of a density of partially covered three-dimensional islands with a density of  $4.4 \times 10^9 \text{ cm}^{-2}$ . The calculated total energy (*solid line*) and its contributions (*dashed lines*) for the various stages of island dissolution are shown. (g) The energetics for a density of  $4.4 \times 10^9 \text{ cm}^{-2}$  (*solid lines*) compared with those for a density of  $10^{10} \text{ cm}^{-2}$  (*dashed lines*). (Wang et al., 2001)

Assuming the top of the island levels off (figure 4.4(b)), a truncated top surface with  $\{001\}$  orientation are forms before the deposition of the capping layer. In the next step as shown in figure 4.4(c), a crater is formed inside the island. In

figure 4.4(d), the hole formation process may end with a partially filled hole, or with the complete removal of the island material, apart from a thin wetting layer covering the interior walls of the hole as illustrated in figure 4.4(e). The overhanging walls in figure 4.4(d) and 4.4(e) are motivated by the experimental observation that the orifice of the holes is typically narrower when the capping layer growth is interrupted at a small layer thickness. The choice of the chemical potential which corresponds to the reported growth condition of the wetting layer of the InAs from the partially covered islands takes place. This is mainly driven by the lowering of the surface energy.

The influence of the GaAs cap layer on the In atom detachment from InAs QDs can be described by a position-dependent surface chemical potential. The modified chemical potential,  $\mu$ , of In atoms can be written as (Ledentsov et al., 1996)

$$\mu^{In}(\mathbf{r}) = \mu_0^{In} + \Omega E_s(\mathbf{r}) + \gamma \Omega \kappa(\mathbf{r}) - \frac{\zeta \Omega \mathcal{G}(\mathbf{r})}{a} \quad (4.2)$$

where  $\mu_0^{In}$  is the chemical potential of In adatoms on an unstressed surface. The second term describes the contribution of the surface elastic energy,  $E_s(\mathbf{r})$ , to the chemical potential, with  $\Omega$  being the atomic volume. The third term is the surface energy contribution, where  $\gamma$  is the surface energy per unit area and  $\kappa(\mathbf{r})$  is the surface curvature. The last term modifies the chemical potential due to a wetting process, where  $\zeta$  is the energy benefit due to the formation of a second wetting layer on the GaAs cap layer,  $a$  is the lattice parameter, and  $\mathcal{G}(\mathbf{r}) = 1$  on the GaAs surface and  $\mathcal{G}(\mathbf{r}) = 0$  on the InAs surface. By the calculation of the total free energy of partially capped InAs dots with GaAs, this concept reveals the cause of the reduction of the total free energy from the redistribution of InAs to form the second wetting layer (Wang et al., 2001).



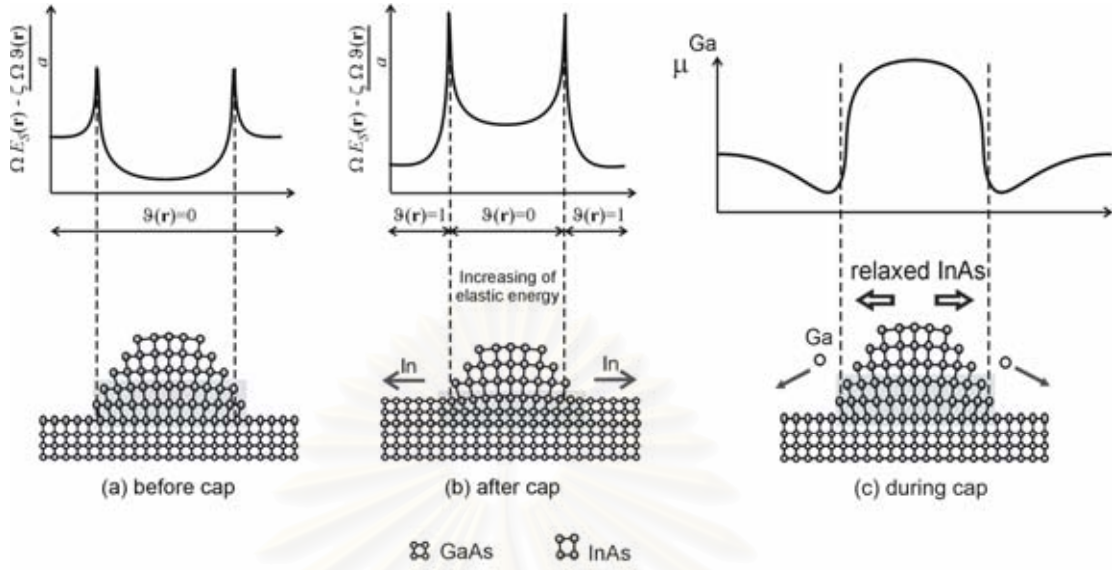


Figure 4.5 Schematic illustrations of the term  $\Omega E_s(\mathbf{r}) - \frac{\zeta \Omega \vartheta(\mathbf{r})}{a}$  for (a) free-standing (b) partially capped InAs QDs with thin GaAs. (c) The chemical potential of Ga atoms during the overgrowth process. (Songmuang, 2003)

Due to the wetting process on the chemical potential the effects of the cap layer on the elastic energy and the energy benefit are considered.  $\Omega E_s(\mathbf{r}) - \frac{\zeta \Omega \vartheta(\mathbf{r})}{a}$  is a free-standing InAs QD on an InAs wetting layer. The  $\vartheta(\mathbf{r}) = 0$  at every position and only the term  $\Omega E_s(\mathbf{r})$  needs to be considered. Strain energy at the QD edge is higher due to the elastic relaxation of the QD, as shown in figure 4.5(a). Figure 4.5(b) shows the overgrown InAs QDs with a thin GaAs layer. By the surrounding GaAs, the lower part of the dot becomes more compressed. Consequently, it increases the surface elastic energy that can cause In atom detachment. (Barabási, 1997) Then, the surrounding GaAs layer induces the detached In atoms to cover the thin GaAs cap layer surface. Therefore, the change of the elastic energy and the surface energy during the overgrowth process cause the dissolution and the collapse of InAs QDs. Moreover, due to strain and surface curvature, the gradient of the chemical potential can describe the preference of the deposited Ga atoms to migrate away from the top of

the dots. As the top of the QDs is partially relaxed, the lattice mismatch between GaAs and InAs at top of QDs is higher than that of between GaAs and InAs at the wetting layer where InAs is compressed by the GaAs substrate. Figure 4.5(c) shows the modified strain profile of the chemical potential of Ga adatoms on the surface which induces the migration from the top of the QDs to the wetting layer region. Therefore, it reduces the growth rate of GaAs at top of QD (Xie et al., 1994). Hence, the collapse of the dot is resulted from In atoms migrating away from QDs plus the unfavorable growth of GaAs on top of the InAs QDs.

#### 4.2.2 Regrowth Process

After the camel-like nanostructures are formed, then 0.6 ML InAs QDs are grown at the same temperature (470°C). The newly grown QDs nucleate and reside in the more energetically favorable nanoholes. Each regrown QD takes place between two blades, which make it look like a propeller of an aircraft, so called nanopropeller-like QDs, as shown in figure 4.6. The propeller's blades are oriented along the  $\langle 1\bar{1}0 \rangle$  crystallographic direction. Moreover, due to the templating effect of the nanoholes, the regrown 0.6 ML QDs are more uniform than the freely grown QDs.

Despite the fact that the original QDs are formed randomly, the subsequent capping stage is well controlled with atomic layer precision. At the regrown thickness of InAs is 0.6 ML, the RHEED pattern changes from streaky pattern to spotty pattern which is inferred the formation of QDs. After a QD is partially capped with GaAs, In adatoms diffuse out of the islands to form the second wetting layer (Wang et al., 2001), resulting in a smaller amount of InAs deposition during the regrowth process (0.6 ML) when compared with the amount of InAs grown on a flat surface (1.8 ML).

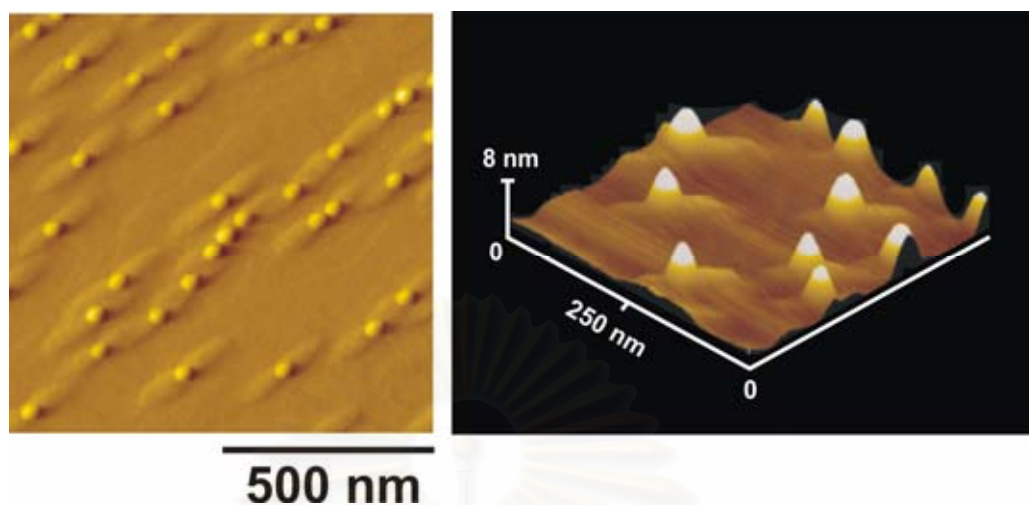


Figure 4.6 Planview (left) and oblique angle (right) AFM images of nanopropeller-like QDs.

#### 4.2.3 The regrowth thickness: the formation of quantum dot molecules

The AFM images of regrown QDs (0.6 ML) look like nanopropellers, where the remains of the initial structure serve as the propellers' blades on both sides as shown in figure 4.7(a). The dot density of nanopropeller QDs is  $2.8 \times 10^9 \text{ cm}^{-2}$ , which is nearly the same as that of initial as-grown QDs and camel-like nanostructures, i.e.,  $2.0 \times 10^9 \text{ cm}^{-2}$ . When the regrown QDs are 0.9 ML, they become bigger, exceeding the nanohole size. We begin to observe the creation of some satellite dots on both propellers' edges. When the regrowth of QDs continues to 1.2 ML, new sets of QDs appear at the propellers' edges, called quantum dot molecules (QDMs). The number of QDs increases to 10-12 dots surrounding the centered dots. The dot density of centered QDs at the regrown thicknesses of 0.9 ML and 1.2 ML are  $2.5 \times 10^9 \text{ cm}^{-2}$  and  $2.4 \times 10^9 \text{ cm}^{-2}$ , respectively. Therefore, we can conclude that the dot density of the centered dots does not change during our partial-capping and regrowth process. Due to time difference in dot formations, the center dots are bigger while the surrounding satellite dots are smaller. This is clearly seen in the AFM images for the 0.9-ML regrowth in figure 4.7(b). However, for the 1.2-ML regrowth in figure 4.7(c), the average sizes of the centered dots and the satellite dots are similar. This is probably

due to the saturation of the growth of center dots after which a proportionally greater numbers of atoms is incorporated into the satellite dots.

It is found that QDMs give a higher dot density due to increased number of satellite-dots. The dot density in figure 4.7(c) is  $3 \times 10^{10} \text{ cm}^{-2}$ , which is an order of magnitude increase from  $2 \times 10^9 \text{ cm}^{-2}$  in figure 4.7(a).

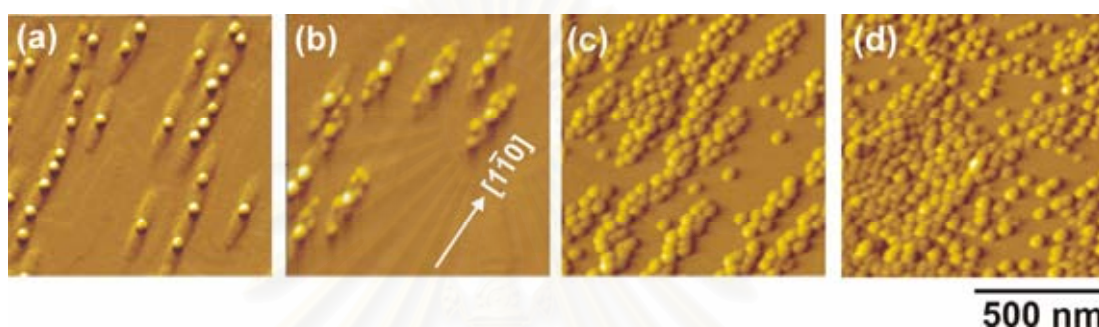


Figure 4.7 AFM images of the samples with regrowth thickness of (a) 0.6 ML, (b) 0.9 ML, (c) 1.2 ML, and (d) 1.5 ML.

The center dots in QDMs are bigger, due to their earlier dot formation. The satellite dots surrounding the center dot appear at a later stage and lose their uniformity as a result. The size distribution is determined by fitting the height histogram with a Gaussian function and measuring in terms of the FWHM. The percentage value is calculated by normalizing the FWHM to the average QD height.

A comparison between dot uniformity of 0.6 ML and 1.2 ML regrown InAs QDs is shown in the dot height histograms in figure 4.8. In the case of 1.2 ML InAs regrowth, the histograms of the center dots (figure 4.8 (b)) and of the satellited dots (figure 4.8 (c)) are separately shown for better analysis. It is clear from the figures that the center dots are more uniform than the satellite dots.



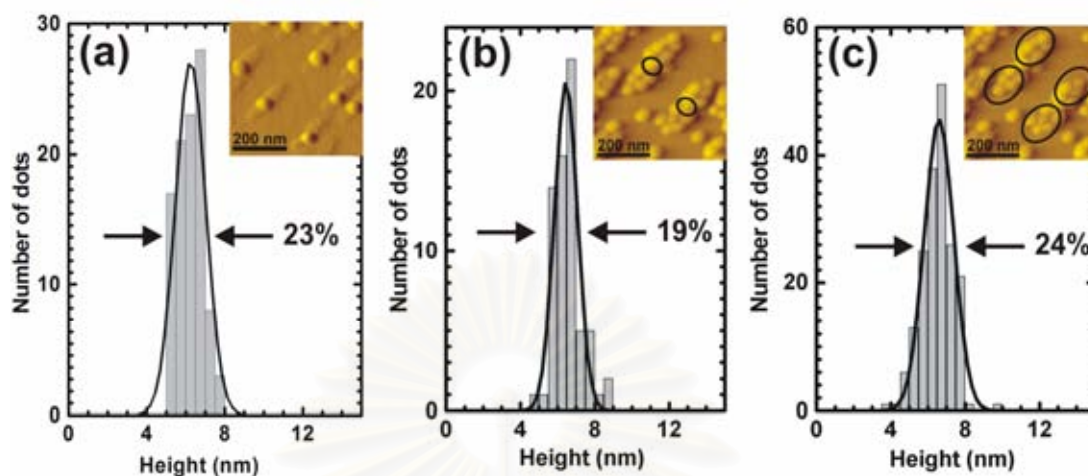


Figure 4.8 Histograms of (a) nanopropeller type quantum dots, (b) QDMs (center dots), and (c) QDMs (satellited dots).

The PL spectra of nanopropeller-like QDs (at 0.6 ML regrowth thickness), the beginning of formation of QDMs (at 0.9 ML regrowth thickness) and QDMs (at 1.2 ML regrowth thickness) are measured at room temperature using a high power  $\text{Ar}^+$  laser (200 mW) as the excitation source. In figure 4.9, the PL spectra of these four samples show the broadening of FWHMs from 24 meV to 31 meV to 46 meV and to 50 meV when the nano-propeller QDs are transformed to QDMs at the regrowth thicknesses of 0.6, 0.9, 1.2 and 1.5 ML, respectively. The shifting of PL peaks from 1.07 eV to 1.06 eV to 1.05 and to 1.04 eV observed in figure 4.9 implies the formation of larger dots at increasing regrown thicknesses.

The strain distribution in QD structure plays an important role for the formation of this structure. The strain profile of a free-standing QD is originated from a mechanism called self-regulation process leading to the narrow size distribution of self-assembled QDs. For the capping process, buried QDs cause the deformation of the matrix surround the QDs and produce the non-uniform strain distribution on the epitaxial surface. With a partially capped layer, the strain modulation in the cap layer is responsible for the preferential nucleation of the QD in the regrowth layer at the place where the local minima of the strain energy locates. There is evidence that the



strain profile after the capping process affects the position of QDs during the regrowth process.

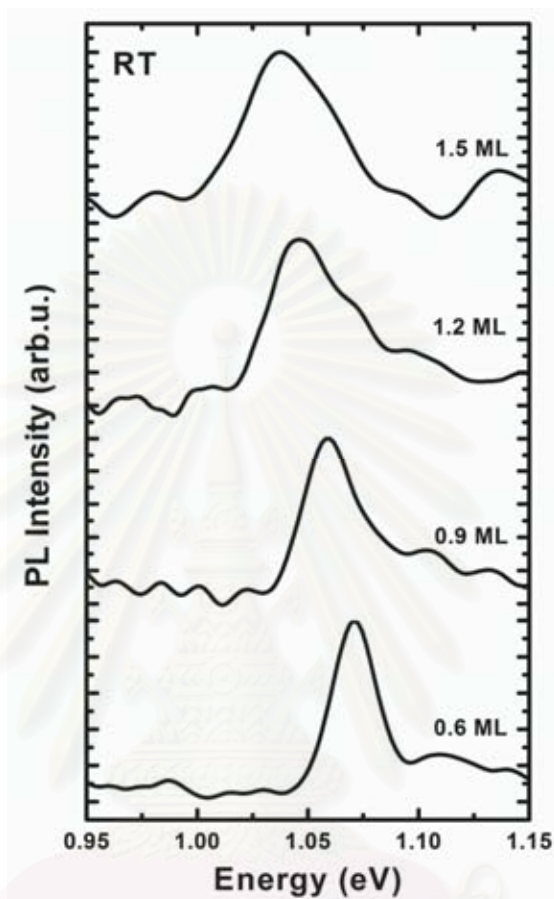


Figure 4.9 Room temperature PL spectra of QDs regrown on the nanoholes template where the regrown thicknesses are 0.6, 0.9, 1.2 and 1.5 ML.

The formation mechanism of the satellite dots can be described by two strain related effects with difference in the stressed system. (Barabási et al., 1997)

- (1) Strain lowers the energy barrier for diffusion; making diffusive hops more probable. As shown in figure 4.5 (b), it means that if atoms are deposited near the dot, strain bases their other random motion, generating a net surface current  $j = -\nabla\mu(x)$ , where  $\mu(x)$  is the local chemical potential. The only contribution to the current comes from the position dependence of the strain energy. Therefore, the strain field around dot generates a net current of adatoms away from the island.

- (2) For large dot size, the strain energy at the edge becomes comparable to the bonding energy of the edge atom, enhancing its detachment. This leads to a gradual dissolution of the island.

The simultaneous action of (1) and (2) gives rise to a kinetic mechanism stabilizing the dot size. As QDs grow, a strain field develops that helps to dissolve the edge atoms (effect (1)). In addition, the further deposited atoms also diffuse away from the larger dots (effect (2)). These combined effects slow the growth rate of large dots and increase the adatom density away from them, therefore, enhancing the nucleation of new dots. The newly nucleated dots are small with strain around them. Hence, they are formed at a much faster rate than the larger one. This eventually leads to a narrow island size distribution (size uniformity) in the system.

Therefore, it is ascribed that increasing in regrown coverage contributes to an increase in the dot density, and much less to the further increase in the size of the existing islands, as inferred in histogram in figure 4.8.

#### **4.2.4 Capped temperature: controlled the number of QDs in QDMs**

During the partial GaAs capping of InAs QDs, if the capping temperature ( $T_c$ ) is varied, the length of the nanopropellers can be controlled. The lowering of the capping temperature, the shorter the propellers' span. Consequently, the smaller the number of QDs per QDM after regrowth. Figures 4.10(a), (b) and (c) are the AFM images of nanopropeller QDs and QDMs grown on nanoholes templates obtained from partial capping the as-grown InAs QDs with GaAs layer at 470°C, 450°C and 430°C, respectively at a regrowth thickness of 0.6 ML.

At 470°C capping temperature, the typical number of QDs per QDM is 10-12 due to the relatively long span of the propeller blades of 275 nm, as shown in figure 10(g). When the capping temperature is reduced to 450°C, the number of QDs per QDM reduces to 6-7 (figure 10(e)) with the shorter span of 215 nm in figure 10(h). Our target of 4-5 dots per QDM is achieved at the capping temperature of 430°C (in figure 10(f)) where the blades' span is approximately 150 nm, as illustrated in figure

10(i). The shorter span at lower capping temperature is expected due to lower atomic mobility.

The correlation between the number of QDs per QDM and the length of the propellers' span is evident: as the span is shortened from 300 nm ( $T_c = 470^\circ\text{C}$ ) to 150 nm ( $T_c = 430^\circ\text{C}$ ), the average number of QDs per QDM decreases from 10-12 to 4-5. The locations of the four satellite dots surrounding the center dots as seen in figure 4.10(c) are not rectangular, but rhombic. We believe that the anisotropic strain fields along the blades' boundary play a major role in determining the nucleation sites. It is also attributed that due to lowering the substrate temperature, In and Ga adatom diffusion lengths are reduced. Therefore, the blades of nanopropellers are shortened leading to smaller QDs per QDMs.

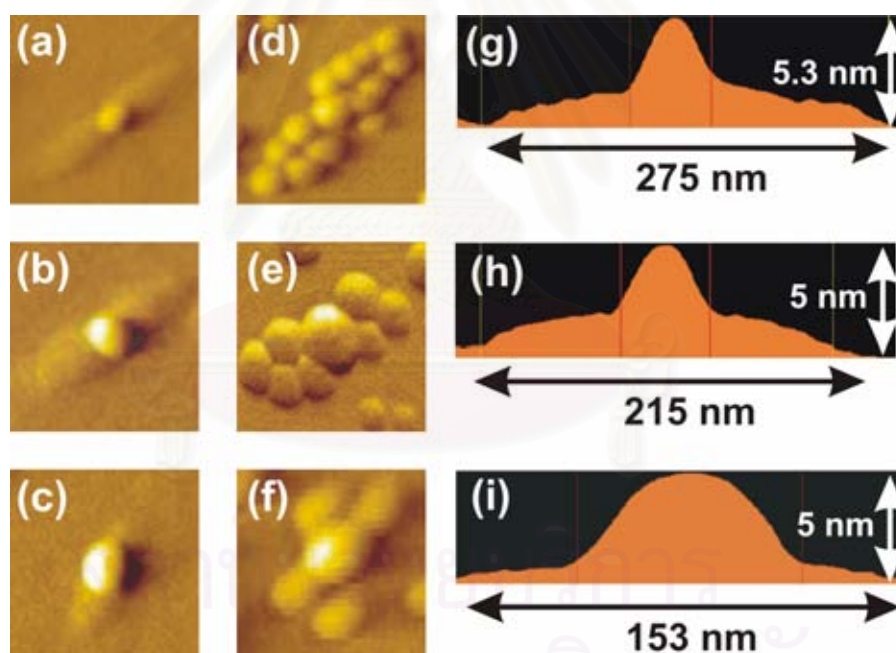


Figure 4.10 AFM images of nanopropeller QDs (a)-(c) at the regrowth thickness of 0.6 ML with their span lengths of the propeller blades (g)-(i) and QDMs (d)-(f) with the regrowth thickness of 1.2 ML at the capping temperature of  $470^\circ\text{C}$ ,  $450^\circ\text{C}$  and  $430^\circ\text{C}$ , respectively.

#### 4.2.5 Regrowth temperature

In order to understand the formation mechanism of QDMs, we conduct another well-defined experiment at the lowest capping temperature of 430°C. After the deposition of 6 ML of GaAs capping layer at 430°C, the regrowth process is started by ramping up the temperature to 500°C within 2 minutes while the In shutter is open under an As<sub>4</sub> pressure of 8x10<sup>-6</sup> torr. The process results in the formation of nanopropeller QDs at the beginning phases whereby satellited QDs are nucleating and growing along the propeller blades. The formation of satellite dots is investigated by studying the evolution of QDMs via a set of AFM images taken at different locations on the same sample. The different locations have been carefully selected to show the different stages of QD formation. When the regrowth temperature increases from 430 °C to 500 °C, the blades of the nanopropellers are longer because the increased thermal energy results in more adatoms movement. After the nanopropeller is formed, the rest of InAs will attach to the sides of the blade, particularly at the blade's boundaries. This gives rise to the first nucleation sites, when the thickness of InAs reached the critical thickness, and the QDM's rhombus configuration results from the asymmetrical strain fields along the  $\langle 1\bar{1}0 \rangle$  directions, as shown in figure 4.11. Figure 4.12 shows a histogram of the number of QDs per QDMs in this sample with an average number of 2-3 dots per molecule.

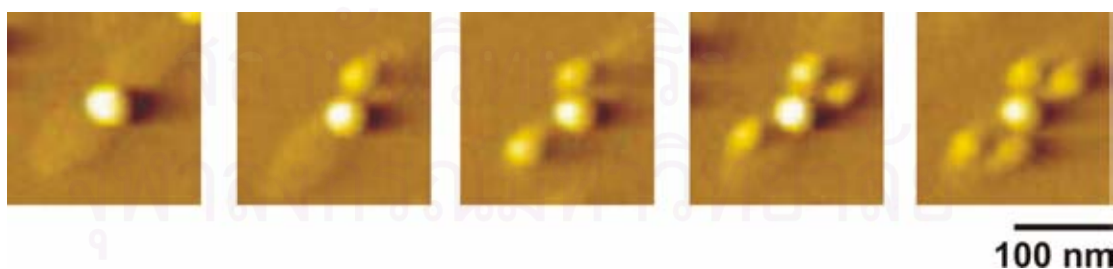


Figure 4.11 AFM image of showing the evolution of self-assembled lateral QDM.

#### 4.2.6 Multi-cycles of partial-capping-and-regrowth technique

Multi-cycles of the partial-capping-and-regrowth process of QDs is another way to fabricate self-assembled, aligned QDs. In addition, improved dot alignment up to a certain number of growth cycles has been investigated.

After the InAs QDs have been formed, the substrate temperature is ramped down to 470°C in order to cap the InAs QDs with 6 ML of GaAs. Then, InAs QDs are regrown at the same temperature with a thickness of 0.6 ML. This is a cycle for partial-capping-and-regrowth technique. The next cycle is started by partially capping with 6 ML of GaAs and subsequently, regrown with InAs QDs. In order to observe the evolution of QD alignment, we repeat our partial-capping-and-regrowth process for 1, 3, 5, 7 and 10 cycles using different samples, and the surface morphologies are compared.

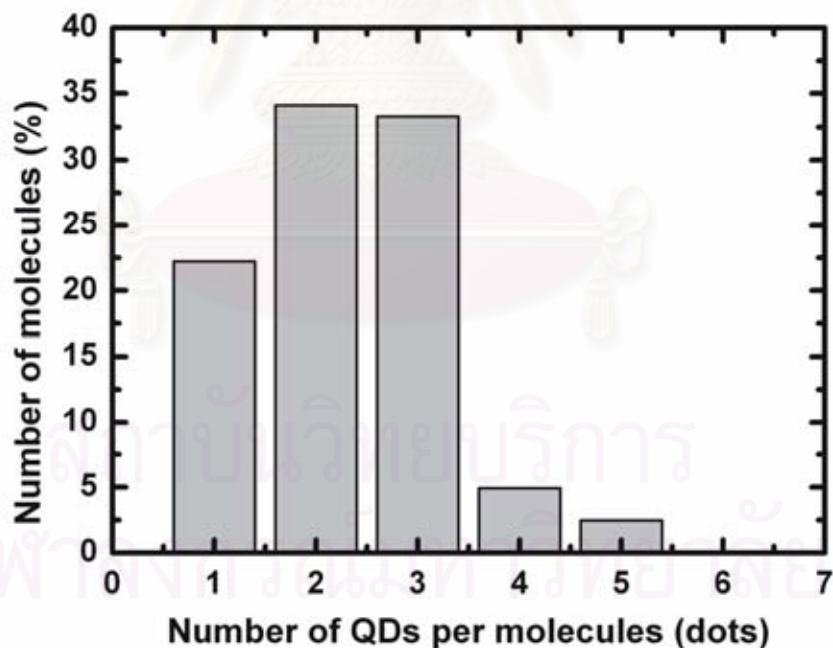


Figure 4.12 Histogram of the number of QDs per molecule when increasing the growth temperature from 430 °C to 500 °C during the regrowth process.



Figures 4.13 (a), (b), (c), (d) and (e) are the AFM images of regrown QDs at 1, 3, 5, 7 and 10 cycles of the partial-capping-and-regrowth process, respectively. A typical span of a nanopropeller QD, as shown in figure 4.13 (a), is 275 nm. When repeating the process for 3 cycles, nanopropeller QDs are linked along the  $\langle 1\bar{1}0 \rangle$  crystallographic direction, as shown in figure 4.13(b). However, as the partial-capping-and-regrowth process is repeated for 5 cycles, adjacent nanopropellers along the  $\langle 1\bar{1}0 \rangle$  direction start to merge, resulting in nanopropeller QDs with broad shoulders both along and across the  $\langle 1\bar{1}0 \rangle$  crystallographic directions, as shown in figure 4.13(c). At 7 cycles of partial-capping-and-regrowth, the underlying template is reshaped into a highly strained, elongated nanostructure because of the increasing volume of strained semiconducting materials. We find that at 7 cycles of partial-capping-and-regrowth of QDs, the best alignment of QDs is achieved. We attribute the result to the long range and the high percentage of strain at the center of the elongated nanostructures, as shown in figure 4.13(d). When we repeat the partial-capping-and-regrowth process beyond 7 cycles, QDs begin to lose their alignment. At 10 cycles, the QDs become random again due to the expansion of the nanopropellers in the  $\langle 1\bar{1}0 \rangle$  and  $\langle 110 \rangle$  crystallographic directions, as shown in figure 4.13(e). Despite the randomness of the 10-cycled sample, it is important to note that the dot density is  $8 \times 10^9 \text{ cm}^{-2}$ , which is much higher than those obtained from the as-grown QD layer. This high dot density provides a stronger PL signal than that of the initial QDs, as shown in figure 4.14. However, there is a small blue shift, indicating smaller dots, and the broadened FWHM of 61.6 meV reflects worsened dot uniformity.

As described in chapter 2, the regrowth process can be explained as growth of stacking QDs. Nanostructures in the first set produce a tensile stress in the GaAs above the nanostructures (region I in figure 2.10 in chapter 2), whereas, the region without nanostructures has little or no stress (region II). Then, the In atoms impinging in region I would be driven by the strain field to accumulate on top of the lower nanostructures, where they can also achieve a lower thermodynamic state energetically due to lower lattice mismatch of InAs with GaAs in tension.

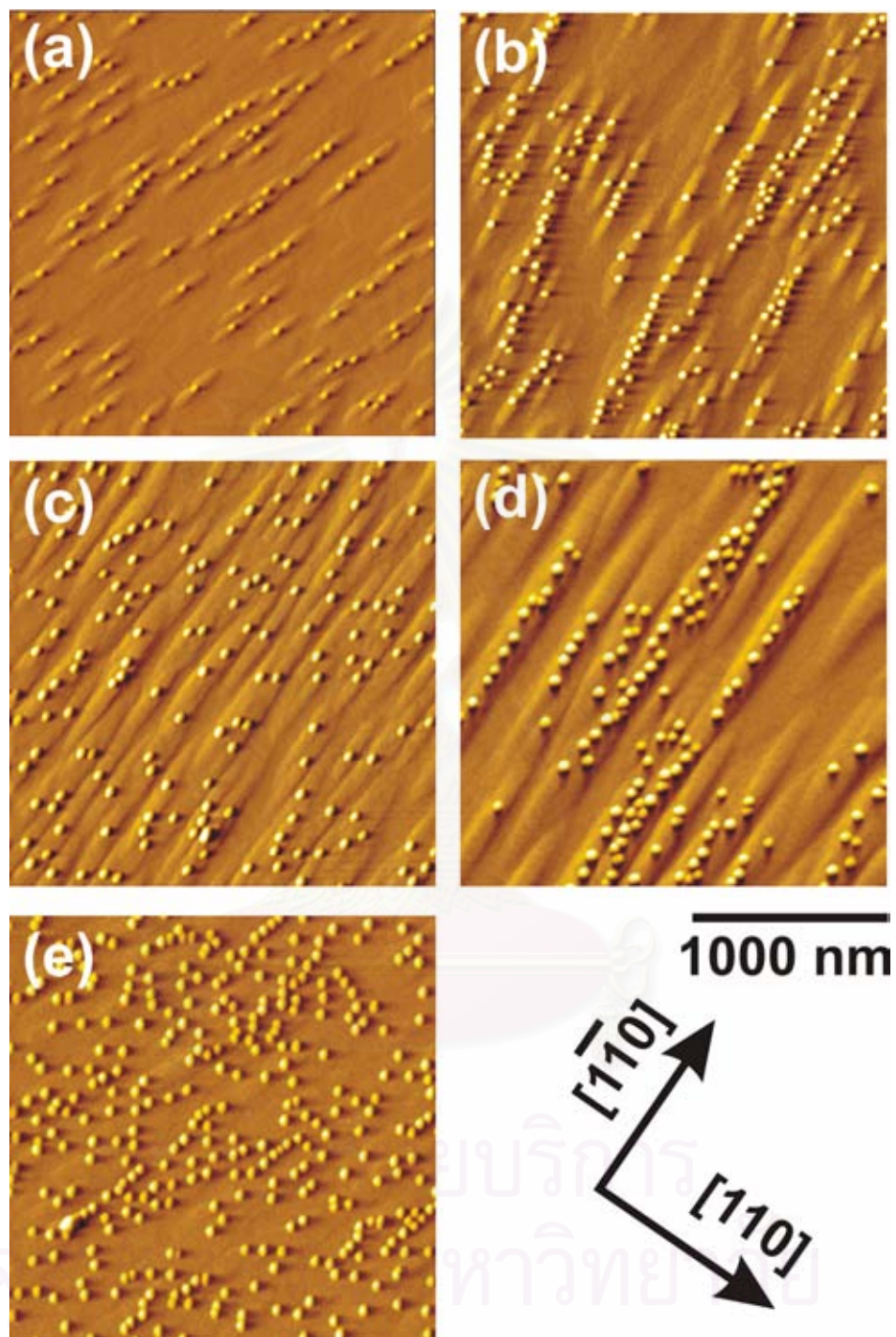


Figure 4.13 The AFM images of regrown QDs by multi-cycle of thin-capping-and-regrowth MBE process at (a) 1 (b) 3 (c) 5 (d) 7 and (e) 10 cycles, respectively.

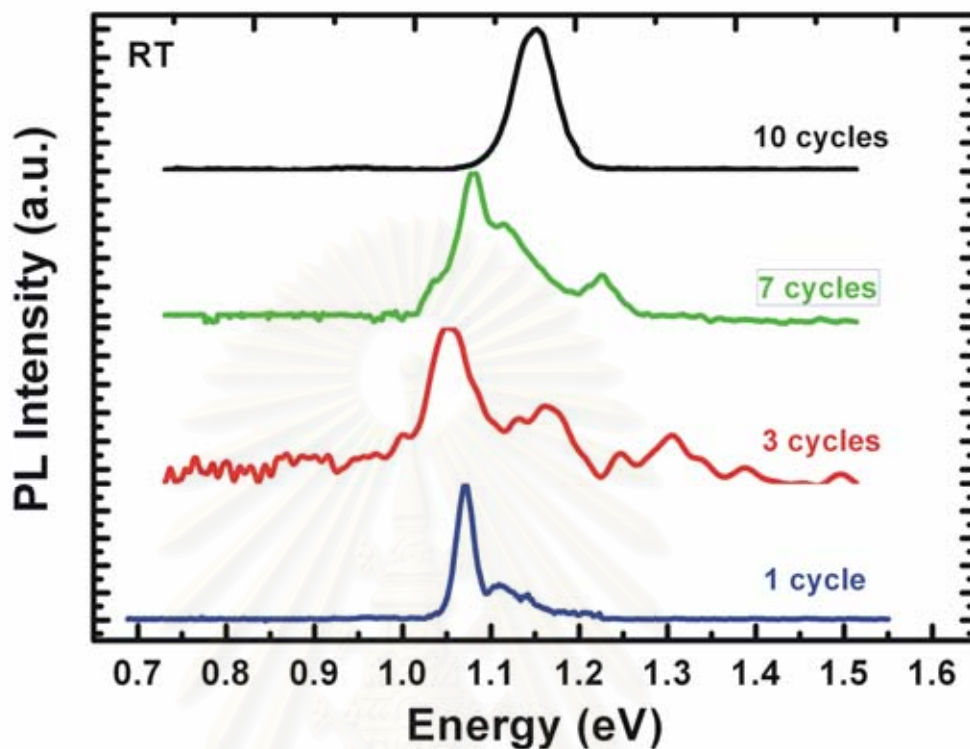


Figure 4.14 Room temperature PL spectra of QDs grown by 1, 3, 7 and 10 cycles.

It is important to note that the mechanism of QD alignment in this approach is not associated with the formation of misfit dislocations, different from QD alignment achieved on a strain-relaxed GaAs/InGaAs/GaAs layer.

Using the partial-capping-and-regrowth process, a single QD can be transformed into a QD set called QDM, as shown in figure 4.15 (a) and (b), respectively. Consequently, aligned QDs can be transformed into aligned QDMs via the same growth technique. We have demonstrated aligned QDMs (figure 4.15(c)) which result from the overlapping of dot sets (figure 4.15(d)).

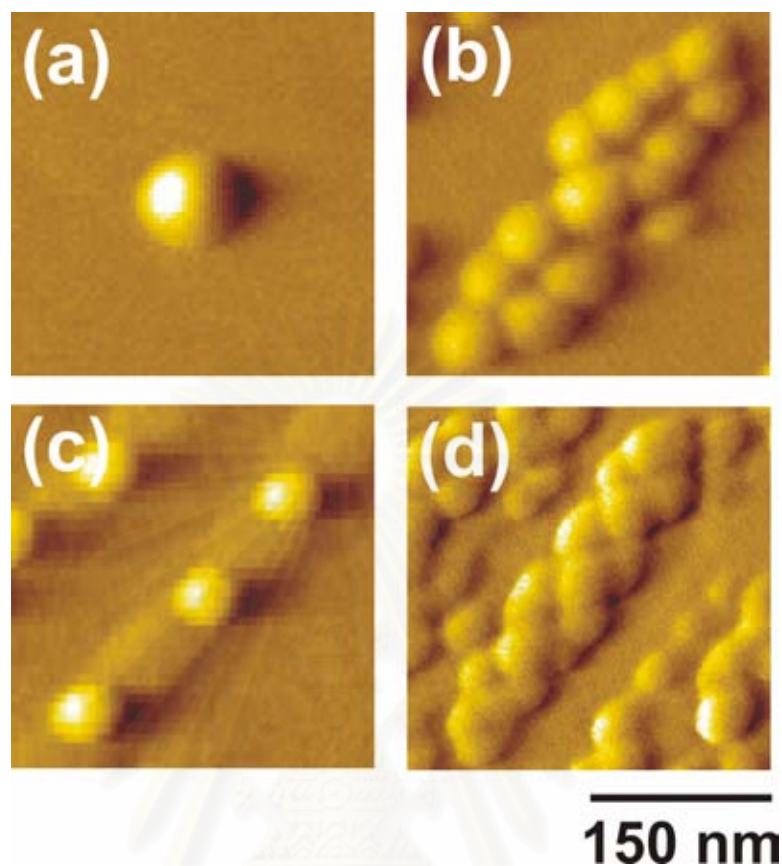


Figure 4.15 QDM (b) originated from as-grown QD (a) by the partial-capping-and-regrowth MBE process. Aligned QDMs (d) are grown from aligned QDs (c) using the partial-capping-and-regrowth process.

#### 4.2.7 Self-assembled elongated nanostructure

After partial capping with 6 ML of GaAs at the temperature of 470°C with the  $\text{As}_4$  flux of  $8 \times 10^{-6}$  Torr, the growth temperature was then ramped up to 550°C while the arsenic pressure was reduced to  $4 \times 10^{-6}$  Torr. Then, the sample was annealed for 30 seconds at 550°C. We found that the self-aligned and reshaped QDs were transformed to elongated nanostructures, as illustrated in figure 4.16. However, in order to create a better and more uniform elongated nanostructure, after the partial capping layer of 6 ML GaAs which leads to the formation of template nanoholes, a regrowth of another InAs QDs was conducted for 1 minute until the RHEED pattern



started to become spotty. These regrown QDs were found to be situated on nanoholes. The critical thickness of templated QD formation is only 0.6 ML compared to 1.8 ML of freely grown QDs, due to the increasing strain field at the nanoholes. The templated QDs were capped by another 6 ML of GaAs layer. The final step was annealing at a temperature of 500°C for 20 seconds. It is revealed that some nanopropeller structures linked with one another into longer chains aligned along the  $\langle 1\bar{1}0 \rangle$  crystallographic direction. Therefore, after the partial capping of nanopropeller-type QDs and then annealing, the longer and uniform elongated nanostructures are realized, as shown in figure 4.17. The RHEED pattern at this final stage shows blurred steaky displays. Figure 4.18 (a), (b), (c), and (d) are RHEED and AFM images at each growth step starting from self-assembled QDs, partial capping of GaAs leading to camel-like structure with nanoholes, regrown QDs of “nanopropeller”, and elongated nanostructure after annealing.

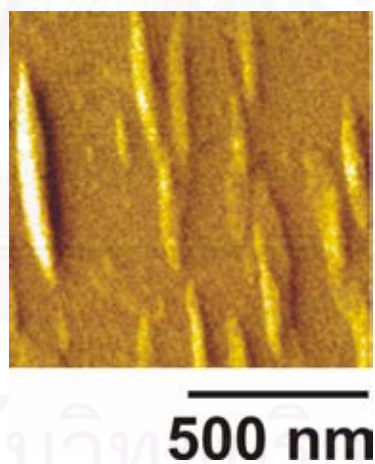


Figure 4.16 AFM images of inhomogeneously self-assembled InAs nanostructure.

The RHEED pattern indicates that the formation of QDs in the second layer occurs earlier than in the first layer. The material in the second layer is directed to local minima of lattice mismatch, which results in a smaller wetting layer (0.6 ML) for the formation of the second layer of QDs. (Schmidt et al., 1999)

The strain fields created by the small islands are overwhelmed by the strain from the neighboring large islands, leading to an annihilation of small islands in the



subsequent layer. This sequence is then repeated for each successive layer, and island spacing and size become progressively more uniform. The explanation for the observed anisotropic lateral alignment is the anisotropic surface kinetics that occurs during GaAs capping of InAs QDs. (Wang et al., 2004)

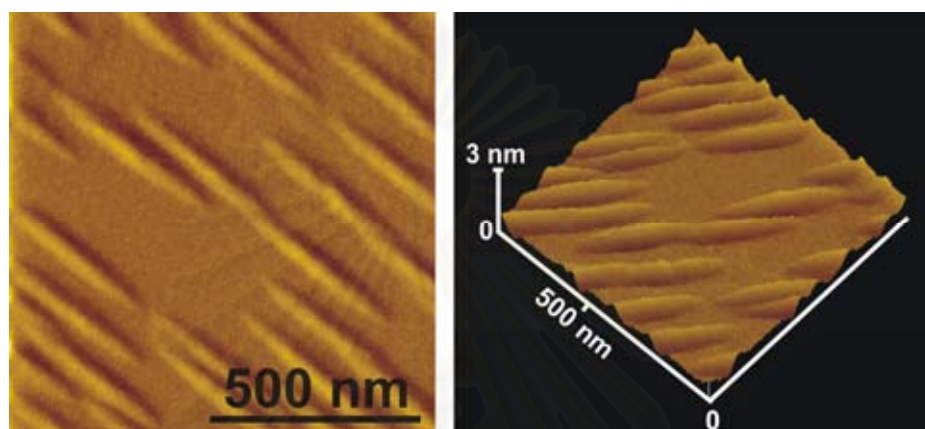


Figure 4.17 AFM images of uniformly self-assembled InAs nanostructure with an average length of 0.5  $\mu\text{m}$ .

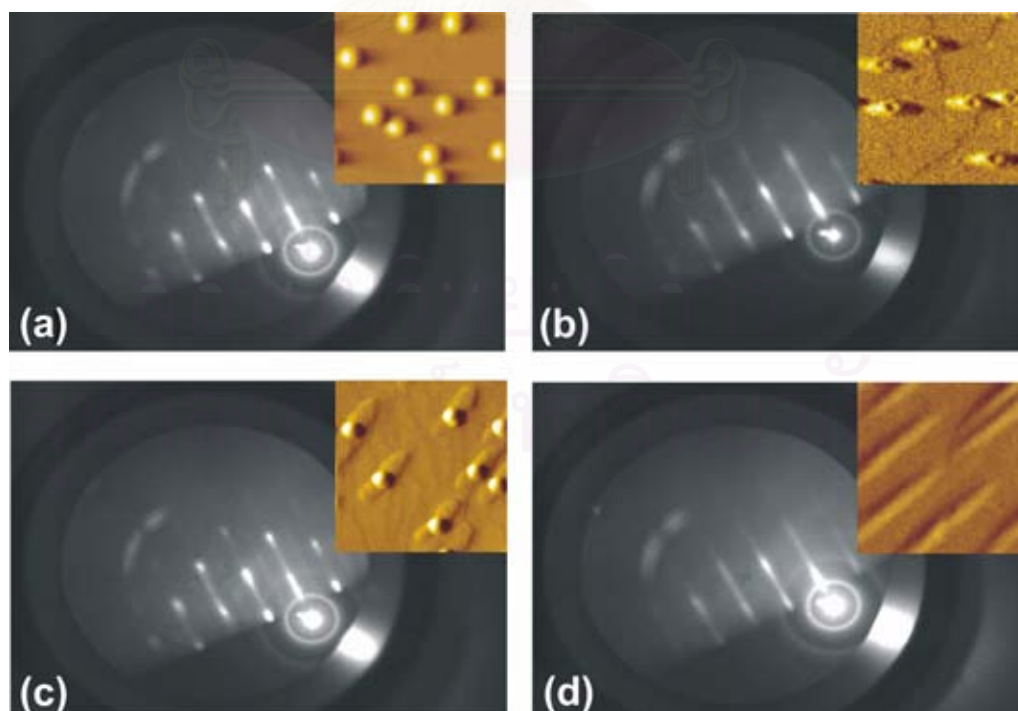


Figure 4.18 RHEED and AFM images at different growth steps.

The anisotropy of In and Ga surface diffusion during capping of QDs is further enhanced by the asymmetry of the QD shape. In particular, the surrounding of the buried (In,Ga)As QDs being an In-rich band along  $\langle 1\bar{1}0 \rangle$  was observed as a result of the redistribution of In due to the high anisotropy of its diffusion characteristics. Especially, when the substrate temperature is increased, the In adatom diffusion is longer leading to the formation of elongated nanostructure. The elongated In-rich band in turn produces an anisotropic strain field in the spacer layer, which enhances nucleation as a template for aligned QDs in the following layer along that specific direction.

Schematic diagrams of transformation mechanism from self-assembled QDs to self-assembled elongated nanostructure are displayed in figure 4.19 for better illustration. The elongated nanostructures or pseudo-quantum wires will have various applications, in particular their polarized nature. However, their basic optical and electronic properties are needed to be well understood for engineering design.

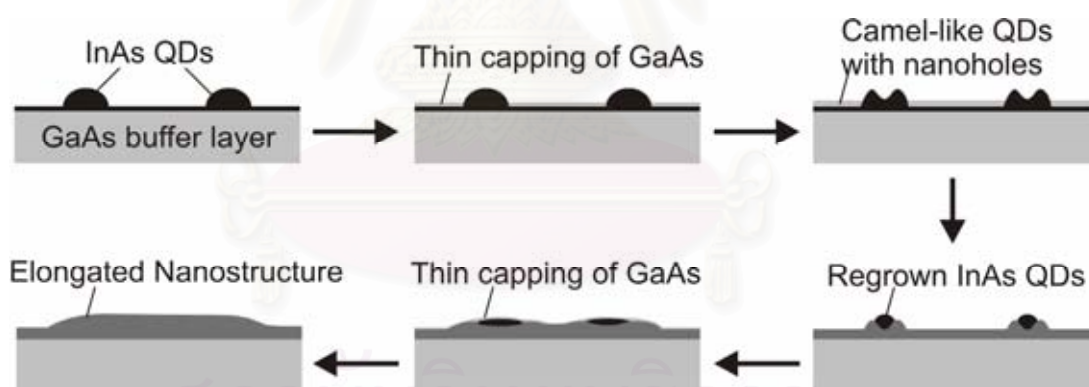


Figure 4.19 The transformation from self-assembled quantum dots to self-assembled elongated nanostructure through thin capping, regrowth of quantum dots on templated nanoholes and annealing process.

#### 4.2.8 Modified growth technique for high dot density

High dot density is a crucial property that is required for fabricating QD solar cells. Hence, in this topic, the growth condition to get high dot density has been investigated. During the growth process of QDMs, when we increase the InAs

thickness from 1.2 ML to 1.5 ML, the number of QDs increases as they begin to cover the whole surface of the sample. We also repeat the partial capping and regrowth process for 5 cycles with regrowth thicknesses of 0.6 ML in the first 4 cycles and 1.5 ML in the last cycle. High dot density covering the whole surface is obtained as shown in figure 4.20. The dot density is now higher than  $6 \times 10^{10} \text{ cm}^{-2}$ . PL data of this sample is also shown in figure 4.21. The PL peak is shifted to 1.04 eV with a broad FWHM of 50 meV.

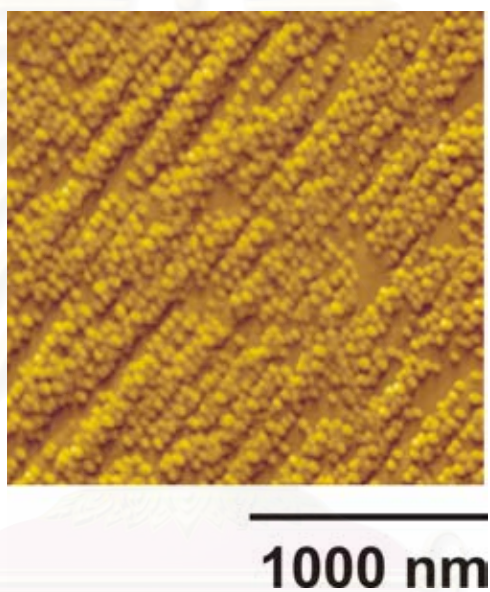


Figure 4.20 AFM image of high dot density QDMs grown by 5 cycles of thin-capping-and-regrowth process with regrowth thickness of 0.6 ML in the first 4 cycles and 1.5 ML in the last cycle.

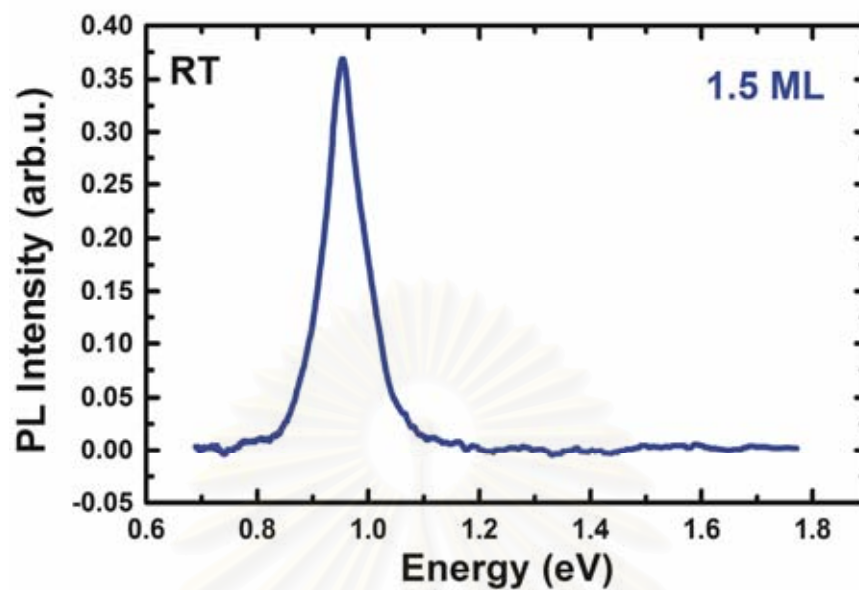


Figure 4.21 PL spectrum of high dot density QDMs from modified growth technique.

## CHAPTER V

### PARTIAL-CAPPING-AND-REGROWTH TECHNIQUE WITH GAS-SOURCE MOLECULAR BEAM EPITAXY

There is significant interest in quantum information processing using QDs. The key building block of a quantum processor is a quantum gate, which is used to entangle the states of two quantum bits (qubits). Quantum gates have been realized using, e.g., ions in traps and nuclear spins in molecules. Recently, a pair of aligned semiconductor QDs has been used as an optically driven quantum gate. In vertically coupled QDs, the upper self-assembled QDs are formed on top of the lower self-assembled QDs due to the strain field around the lower QDs. The vertical separation between the upper and the lower QDs controls the degree of coupling. In principle, however, laterally coupled QDs are preferred because they allow a large number of quantum gates in a two-dimensional array on the surface. An electric field applied between the two QDs can localize individual carriers on the left dot (index zero) or the right dot (index one). The two different dot indices play the same role as the two states of a “spin” (a qubit) and are referred to as “isospin”. When the electric field is turned off, the quantum mechanical tunneling rotates the “isospin” leading to the superposition of two QD states. The quantum gate is built when two different particles, an electron and a hole, are created optically. In the presence of the electric field, the particles are localized on opposite dots.

In this chapter, the formation of InAs double quantum dots (DQDs) is achieved on a GaAs substrate by gas-source MBE under  $\text{As}_2$  overpressure using the partial-capping-and-regrowth technique. Morphological studies by AFM and temperature dependence of DQD optical properties are investigated.



## 5.1 Double QDs

The growth process with the gas-source MBE system uses the same procedure as with the solid-source MBE system except the type of arsenic source used, arsine, which produces  $\text{As}_2$  and hydrogen gas. Under  $\text{As}_2$  overpressure and deposition of 1.8 ML amount of InAs, QDs are formed randomly on the surface at a temperature of  $500^\circ\text{C}$ . Then, the substrate temperature is ramped down to  $470^\circ\text{C}$  and InAs QDs are capped partially with a 6 ML-thick GaAs layer. When 0.6-ML-thick InAs is deposited, DQDs are formed on the partially covered InAs QDs. Then a 150-nm thick GaAs buffer layer is grown and the partial-capping-and-regrowth process is repeated once more. The dot formation is monitored *in-situ* by reflection high-energy-electron diffraction (RHEED).

Figures 5.1(a) and (b) show AFM images of as-grown QDs at a coverage of 1.8 ML and DQDs, respectively. DQDs are oriented along the  $\langle 1\bar{1}0 \rangle$  crystallographic direction. The dot density of as-grown QDs is  $6 \times 10^9 \text{ cm}^{-2}$ , whereas the total QD density in the DQD sample is  $1.1 \times 10^{10} \text{ cm}^{-2}$ , consisting of  $9.4 \times 10^9 \text{ QDs cm}^{-2}$  from  $4.7 \times 10^9 \text{ DQDs cm}^{-2}$ , and  $1.9 \times 10^9 \text{ QDs cm}^{-2}$ . Each as-grown QD is transformed into a quantum ring (QR) after the partial-capping process, as shown in figure 5.1(c). Then, QRs become DQDs after redepositing InAs. The DQD density is, however, lower due to merging of some DQDs into single dots. Figures 5.1(d) and (e) show an AFM image and a dot height histogram obtained from the AFM image of the DQD sample, respectively. Note that the QDs in the DQD sample are largely comprised of smaller dots than as-grown QDs. The histogram in figure 5.2 shows the center-to-center separation of DQDs, and it is fitted with a Gaussian distribution with an average separation of 22 nm. This relatively large separation shows that the PL observed from DQDs, shown below, is from individual QDs in the DQDs.

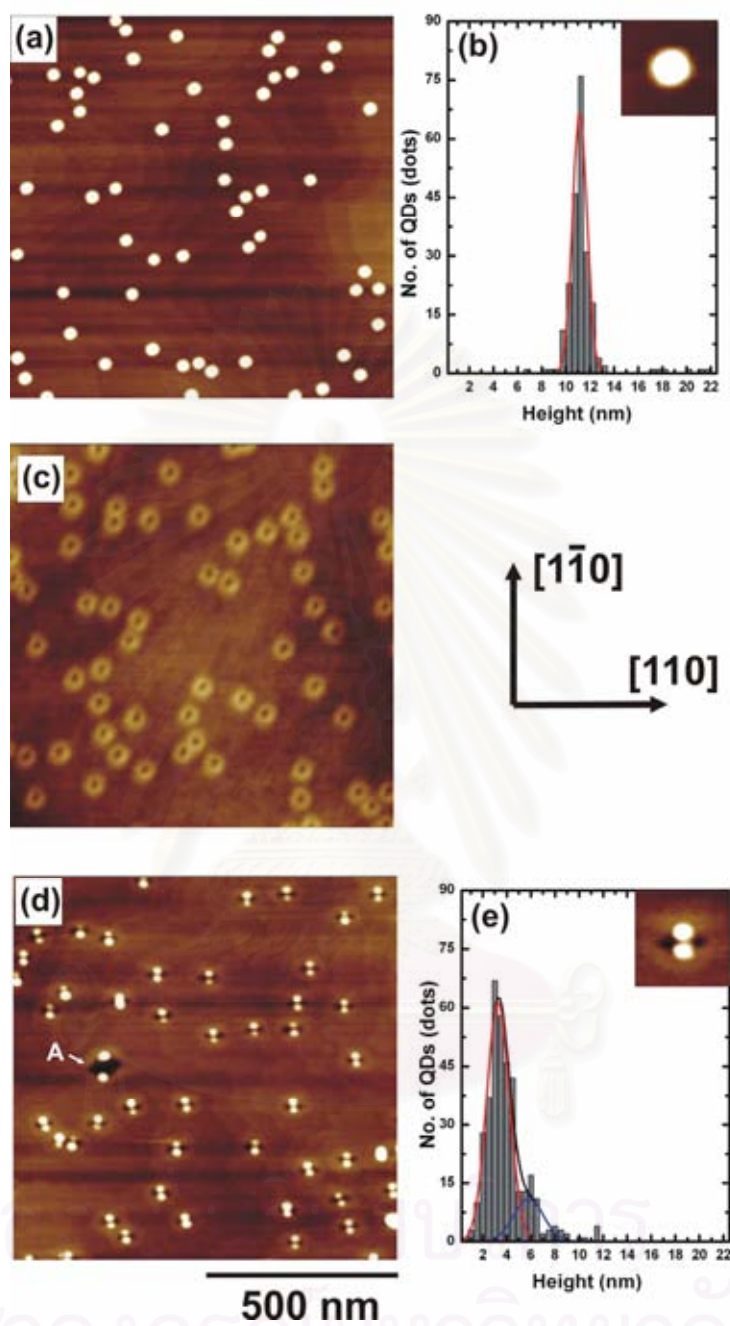


Figure 5.1 (a) AFM image and (b) dot height histogram with Gaussian fit of as-grown QDs; (c) AFM image of QRs, (d) and AFM image and (e) dot height histogram with a Gaussian fit of DQDs.

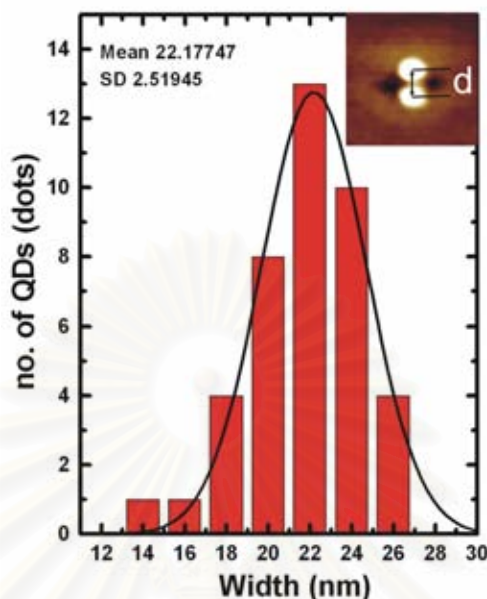


Figure 5.2 Center-to-center width histogram of DQDs with Gaussian fit.

### 5.1.1 Optical properties of DQDs

Figure 5.3 shows PL spectra of as-grown QDs and DQDs at 9 K with excitation power density ranging from 0.13 to 8 kW/cm<sup>2</sup>. The highest peaks of as-grown QDs and DQDs spectra are at 1.08 and 1.195 eV with FWHM of 28 and 60 meV, respectively. The spectrum of the DQDs can be described by two Gaussian curves composed of a higher peak at 1.19 eV and a smaller peak at 1.128 eV. These results confirm the bimodal distribution of dot heights. The PL spectra are normalized to the highest peak. As the incident excitation power increases, the higher energy PL peak of the as-grown QD sample increases relative to the lower-energy PL peak. The low energy peak is saturated when the laser excitation increases. This indicates that the lower-energy peak PL is from ground-state transitions and the higher energy peak is from the first excited states. On the other hand, the relative intensity of the two peaks in DQDs PL remains the same with increasing incident excitation power, indicating that these two peaks are from ground-state transition from QDs with different dot sizes, as shown in figure 5.1(e).

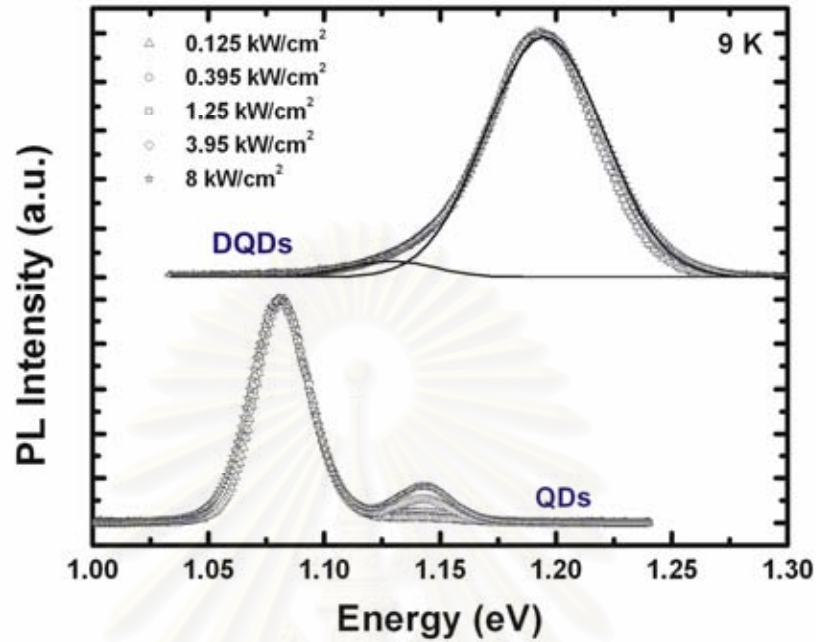


Figure 5.3 PL spectra of as-grown QDs and DQDs at 9 K. The dotted curves for DQDs are the Gaussian components.

Despite a higher dot density, the PL intensity of DQDs is lower than that of QDs. It is attributed to defects such as nanovoids, as shown by “A” in figure 5.1(d), which could affect the optical efficiency due to nonradiative recombination.

Temperature-dependent PL data from 9 to 290 K are also obtained while the incident excitation intensity is held constant at 10 kW/cm<sup>2</sup>. Figure 5.4 shows the temperature dependence of the peak emission energy, which can be fitted by the Varshni model. (Varshni, 1967)

$$E(T) = E_0 - \frac{\alpha T^2}{T + \beta} \quad (5.1)$$

where  $E(T)$  and  $E_0$  are the peak energies at T and 0 K, respectively, and  $\alpha$  and  $\beta$  are constants. The variation of the peak emission energy with temperature can be attributed to the effect of dilation of lattice and electron-lattice interaction. The solid line in Figure 5.4 is the Varshni equation with  $E_0 = 1.083$  eV for as-grown QDs and 1.198 eV for DQDs,  $\alpha = 3.16 \times 10^{-4}$  eV/K and  $\beta = 93$  K for both as-grown QDs and

DQDs. The  $\alpha$  and  $\beta$  values agree with those of InAs. (Varshni, 1967) The maximum red shift of 23 meV in the DQD curve from the Varshni equation is probably due to transfer from smaller dot family (higher energy) to larger dot family (lower energy) within the QDs of the DQD family, but not to the much larger dots in figure 5.3, where the energy difference is much larger,  $\sim 80$  meV. (Polimeni et al., 1999; Mi and Bhattacharya, 2005)

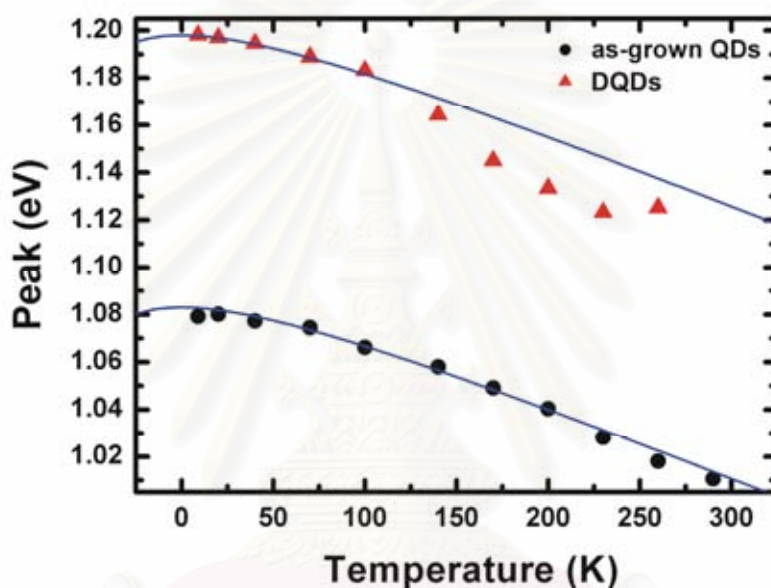


Figure 5.4 The temperature dependent peak emission energy of as-grown QDs and DQDs. The solid lines are calculations from the Varshni equation.

Figure 5.5 shows the PL intensity of as-grown QDs and DQDs versus inverse temperature. As the measurement temperature increases from 9 K, the PL intensity of DQDs remains constant up to 100 K and then rapidly quenches. The solid lines are fitted with an assumption of two thermally activated processes with equation (5.2). (Lambkin et al., 1994; Nishikawa et al., 2004)

$$I(T) = \frac{I(0)}{1 + Ae^{-E_a/kT} + Be^{-E_b/kT}} \quad (5.2)$$



where  $I(T)$  and  $I(0)$  are the PL intensity at  $T$  and  $0$  K, respectively;  $A$  and  $B$  are constants;  $E_a$  and  $E_b$  are thermal activation energies. Activation energy  $E_a$ , derived from the slope of the straight-line portion (150-300K) of the curves, is 45 and 128 meV for as-grown QDs and DQDs, respectively. The smaller energy  $E_b$  is ascribed to

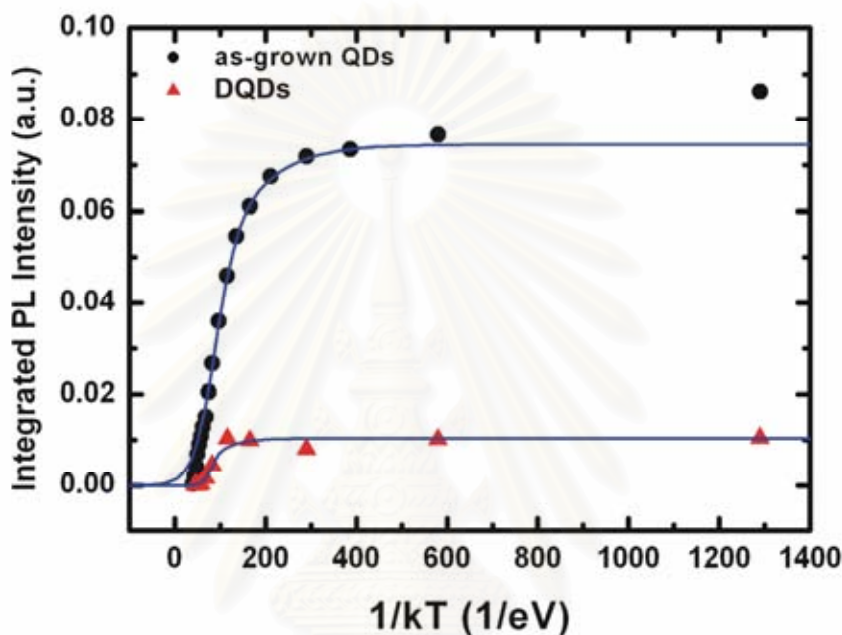


Figure 5.5 The temperature dependence of PL intensity of as-grown QDs and DQDs.

trapped excitons or carriers thermalizing from localized regions resulting from potentials fluctuations due to size distribution of QDs. The larger energy of  $E_a$  corresponds to the difference in energy between the ground state and the wetting layer if there are no localized states.  $E_a$  for DQDs then is expected to be smaller than  $E_a$  for as-grown QDs because of smaller dot size. Our results are contrary to this expectation, indicating the existence of non-radiative recombination centers in DQDs between the QD energy level and the wetting layer energy level.

Since DQDs are grown at relatively lower temperature, rapid thermal annealing (RTA) is used to improve the material quality. The effect of postgrowth RTA, in nitrogen ambient at temperature of 650-850°C for 30s, on the optical

properties of DQDs is investigated. Temperature dependent PL data are measured from 9 to 290 K using 50 mW incident excitation of a solid-state 532 nm laser. The peak emission energy of as-grown DQDs is fitted by the Varshni equation, and the parameters match those of InAs. For samples annealed at 750 and 850°C, the values are in the range between those of InAs and GaAs due to inter-diffusion between Ga and In during the annealing process, as shown in table 4.1.

parameters \ samples	samples		DQDs	DQDs	DQDs	DQDs
	InAs	GaAs	as-grown	annealed 650°C	annealed 750°C	annealed 850°C
$\alpha (\times 10^4 \text{ eV/K})$	3.16	8.87	3.16	3.60	4.35	6.82
$\beta \text{ (K)}$	93	572	93	150	280	420

Table 5.1 The parameters from Vashni equation of as-grown DQDs and annealed DQDs at 650°C, 750°C and 850°C comparing with InAs and GaAs.

When the measurement temperature is lower than 140 K, the PL FWHM are measured to be 42 and 30 meV for RTA samples annealed at 750 and 850°C, respectively. These values are smaller than that of as-grown DQDs (60 meV) indicating better size homogeneity by the annealing effect.

The intensity of PL line shape is fitted with exponentials with activation energy  $E_a$  and  $E_b$ , corresponding to potential fluctuations and deep nonradiative centers, respectively. For the annealed samples at 750°C,  $E_a$  and  $E_b$  are 25 and 81 meV. These values are also smaller than those of as-grown DQD sample (25 and 128 meV respectively) indicating that RTA can improve the DQD material quality.

In addition, DQDs tend to align along  $[1\bar{1}0]$  crystallographic direction. Therefore, polarized PL measurement is investigated at 9 K along  $[1\bar{1}0]$  and  $[110]$  crystallographic directions to determine the linear polarization degree (PD), which is attributed mainly to dot shape anisotropy. The polarization degree can be calculated by

$$PD = \frac{I_{[1\bar{1}0]} - I_{[110]}}{I_{[1\bar{1}0]} + I_{[110]}} \quad (5.3)$$

The PDs of PL emission of as-grown QDs and DQDs are 19% and 8%, respectively. The polarization is attributed mainly to dot shape anisotropy, indicating QDs in DQDs have less size dispersion than QDs. When considering on annealed DQDs samples, the PD of these samples are 2% smaller, indicating not much change in dot shape anisotropy.

## 5.2 The formation of QD rings

By increasing the substrate temperature to 520°C during redeposition of InAs in solids-source MBE, the morphology becomes more like as-grown QDs because of longer surface migration length of In adatoms at higher temperature. On the other hand, in gas-source MBE self-assembled QRs are transformed to QD-rings, as shown in figure 5.6. The distribution of the number of dots per ring is shown in figure 5.7. There are largely comprised of big single QDs. In case of QD ring, there are around 4-6 dots per ring. For the formation of QD rings, this is probably because of the shorter In migration length under As<sub>2</sub> than under As<sub>4</sub> overpressure and higher In concentration. Therefore, larger strain is created on the rim of the QRs than the surrounding area. With redeposition of InAs at high growth temperature, QDs are formed along the rim of QRs. Although the QD-rings are not yet uniformly controlled, these nanostructures are very interesting from the fundamental physics point of view.

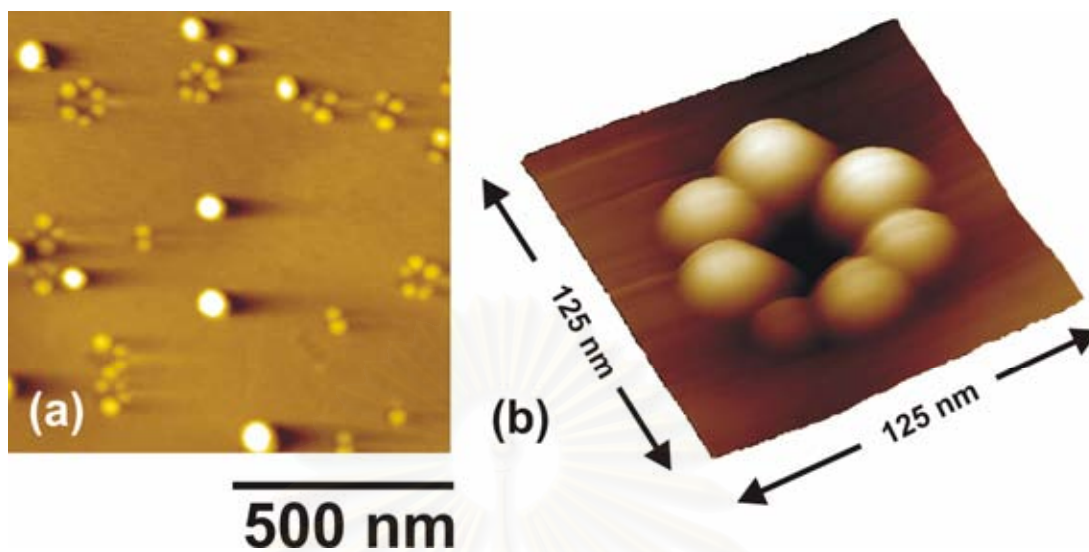


Figure 5.6 Planview (a) and oblique view (b) AFM image of a QD ring.

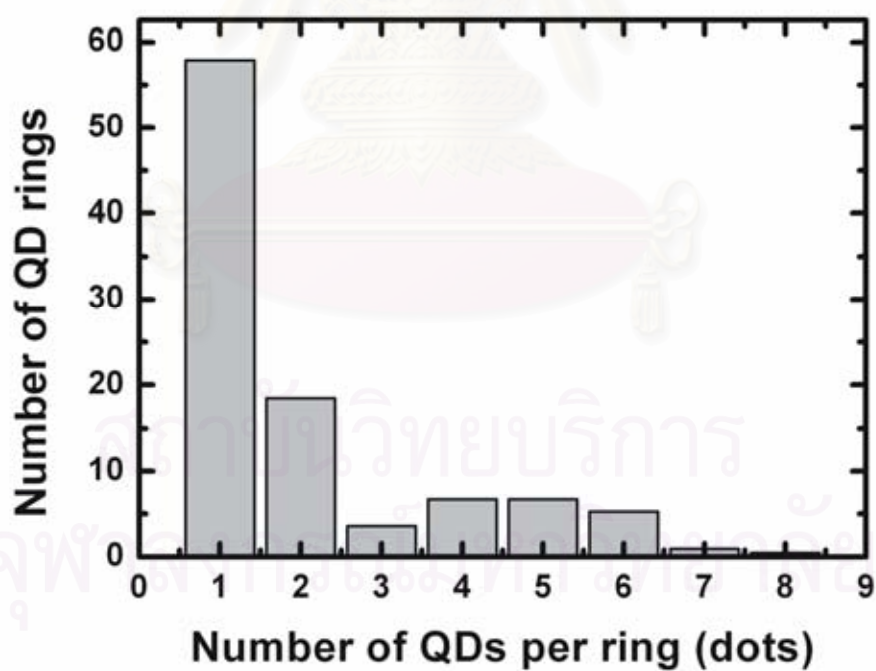


Figure 5.7 The histogram of number of dots per ring.

## CHAPTER VI

### COMPARISON OF NANOSTRUCTURES GROWN BY SOLID-SOURCE MBE AND GAS-SOURCE MBE

Surface morphologies of self-assembled (Ga)InAs nanostructures grown by a partial-capping-and-regrowth technique using gas-source MBE and solid-source MBE are compared. With solid-source MBE under an  $\text{As}_4$  ambient, as-grown QDs change to a camel-like nanostructure after being partially overgrown with GaAs. When additional InAs are deposited, QDMs are created. In comparison, with gas-source MBE under  $\text{As}_2$  overpressure, as-grown QDs are transformed into quantum rings after partial capping with GaAs and then, after regrowth, become double QDs. At higher regrowth temperature, QD rings are formed.

Morphological surfaces and their structural properties of InAs QDs after the initial partial GaAs capping process grown on GaAs (001) have been reported by several groups. The surface morphology after the capping process is affected by several parameters, such as the size of as-grown QDs affecting different initial strain conditions (Joyce et al., 2001) and different capping temperature affecting In-Ga intermixing. (Songmuang et al., 2003) Granados *et al.* found that under  $\text{As}_2$  overpressure, quantum rings (QRs) are formed (Granados et al., 2003), but under  $\text{As}_4$  overpressure, camel-like nanostructures are obtained.

In our work, we take one step further with redepositing InAs (regrowth) after partial GaAs capping. We found self-assembled lateral QDMs and we investigate the effect of arsenic species, i.e.  $\text{As}_2$  from gas-source MBE and  $\text{As}_4$  from solid-source MBE. Dramatically different lateral QDMs are obtained. Morphological studies by AFM are presented and discussed.

Figures 6.1 (a) – (d) show AFM images of as-grown QDs, camel-like nanostructures, nanopropeller-like nanostructures and QDMs grown under  $\text{As}_4$  overpressure in solid-source MBE. When InAs QDs are partially capped with GaAs, anisotropic strain fields modify the initial dots into camel-like nanostructures having



nanoholes on top. After deposition of 0.6 ML amount of InAs, nanopropeller-like nanostructures are formed with two blades aligned along the  $\langle 1\bar{1}0 \rangle$  crystallographic direction. When 1.2 ML amount of InAs is deposited, sets of QDs or QDMs are formed and are aligned along the  $\langle 1\bar{1}0 \rangle$  crystallographic direction.

According to Granados and Garcia, camel-like nanostructures or QRs form only on large QDs (dot height  $> 7$  nm), which presumably are relaxed. (Granados et al., 2003) With partial covering of relaxed InAs QDs by GaAs, the stress produces enough strain energy that QDs undergo phase transition to become liquid and dewetting takes place. InAs flows out of the center, resulting in a hole (depth  $\sim 0.7$  nm) at the center of the QD. At the same time alloying with GaAs takes place. Because In adsorption on As-terminated steps (B steps), perpendicular to the  $\langle 1\bar{1}0 \rangle$  direction, is more than on cation-ion-terminated steps (A steps), perpendicular to the  $\langle 110 \rangle$  direction, a camel-like nanostructure forms along the  $\langle 1\bar{1}0 \rangle$  direction. This structural modification of as-grown QDs after GaAs thin capping (6 ML) at low temperature ( $470^\circ\text{C}$ ) is confirmed by our experimental result as shown in figure 6.1(b).

In the regrowth process with SSMBE, InAs overfills the nanoholes on the camel-like nanostructures, leading to nanopropeller-like formation with two blades as displayed in figure 6.1(c). This could be explained by the shallow hole depth (0.7 nm) and less In-Ga intermixing at low growth temperature ( $470^\circ\text{C}$ ). Because of the longer migration length of In adatoms along the  $\langle 1\bar{1}0 \rangle$  direction and more step kinks on the blades, with further deposition of InAs up to 1.2 ML, QDs preferentially grow at these kinks, due to lower surface energy than on a flat surface. Therefore, QDMs are formed with 10-12 dots per group as typically shown in figure 6.1(d). The span of nanopropellers is a key parameter to control the number of dots per blade. Shorter span is realized by thin capping of as-grown QDs at lower temperature of  $430^\circ\text{C}$ . We can reduce the number of dots per blade to 5-7.

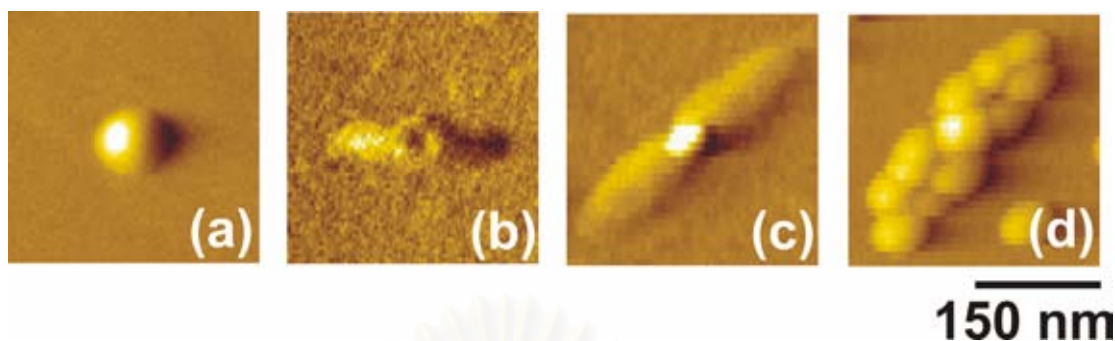


Figure 6.1 AFM images of (a) as-grown QDs, (b) camel-like nanostructures, (c) nanopropeller-like QDs with the regrowth thickness of 0.6 ML and (d) QDMs with the regrowth thickness of 1.2 ML grown under  $\text{As}_4$  overpressure in solid-source MBE.

Figures 6.2 (a) – (c) show AFM images of as-grown QDs, quantum rings and double quantum dots (DQDs) aligned along  $\langle 1\bar{1}0 \rangle$  under  $\text{As}_2$  overpressure in GSMBE. Each as-grown QD is transformed into a quantum ring (QR) after partial-capping with 6 ML GaAs. Typical QR having outer ring diameter of 120 nm and inner ring diameter of 40 nm is shown in figure 6.3(b). When additional 0.6-ML amount of InAs is deposited, QRs are transformed into DQDs. The total QD density in figure 6.2(c) is  $1.1 \times 10^{10} \text{ cm}^{-2}$  consisting of 80% DQDs and 20% single dots, whereas the dot density of as-grown QDs is  $6 \times 10^9 \text{ cm}^{-2}$  as originally shown in figure 6.2(a). The total QD density in the DQD sample is not completely twice of that in the as-grown QD sample due to merging of some DQDs into single dots. The merging DQDs are observed in some particular areas of figure 6.2(c) like at point A where initial merging starts, at point B where a DQD is merging into a single dot, and at point C where a completely merged QD is found. Note that the DQDs are comprised of smaller dots (dot height  $\sim 4$  nm), as compared to as-grown QDs (dot height  $\sim 12$  nm). Typical DQD having good dot symmetry is selected and shown in the figure 6.3(c).

Offermans et al. show that under  $\text{As}_2$  overpressure, the QR structure with a hole depth of 1.2 nm has In-rich  $\text{In}_x\text{Ga}_{1-x}\text{As}$  regions around the rim in the  $\langle 1\bar{1}0 \rangle$  direction (Offermans et al., 2005), resulting in higher strain. When 0.6 ML amount of

InAs is deposited uniformly on QRs, strain becomes higher at these particular parts of QRs along  $\langle 1\bar{1}0 \rangle$  crystallographic direction. When the amount of deposited InAs is increased, the strain in these two regions relaxes, leading to the formation QDs, which become a QD pair or a DQD. This explanation of DQD formation is in agreement with our experimental result conducted in GSMBE where  $\text{As}_2$  is used as a group-V source. Because of the initial strain created by thin capping layer, the amount of InAs material required for DQD formation on QRs is less (0.6 ML) than that required on a flat surface (1.8 ML). This can explain why a DQD is composed of smaller dots than as-grown QD. The difference in QD size is clearly shown in the comparison of figure 6.3(a) and figure 6.3(c).

We conclude here that different outcomes of modified QD structures, i.e. nanopropeller-QDs and DQDs, are obtained at the same regrowth InAs thickness of 0.6 ML after GaAs thin capping at the same growth conditions in solid-source MBE and gas-source MBE, respectively. The origin of the difference in these nanostructures is believed to be the effect of arsenic species, i.e.  $\text{As}_4$  in solid-source MBE and  $\text{As}_2$  in gas-source MBE.

To confirm the crystal quality of these two different nanostructures, photoluminescence (PL) spectra at 9 K of QDRs, DQDs and nanopropeller QDs are presented in figure 6.4. Narrow FWHM of the PL spectrum (25.4 meV) from the nanopropeller QD sample is measured. This is due to the confinement of QDs in nanohole templates of camel-like nanostructures leading to higher dot uniformity than those in the DQD sample. The PL shift to shorter wavelength of the DQD sample confirms that the QD size in DQDs is smaller than that of nanopropeller QDs.

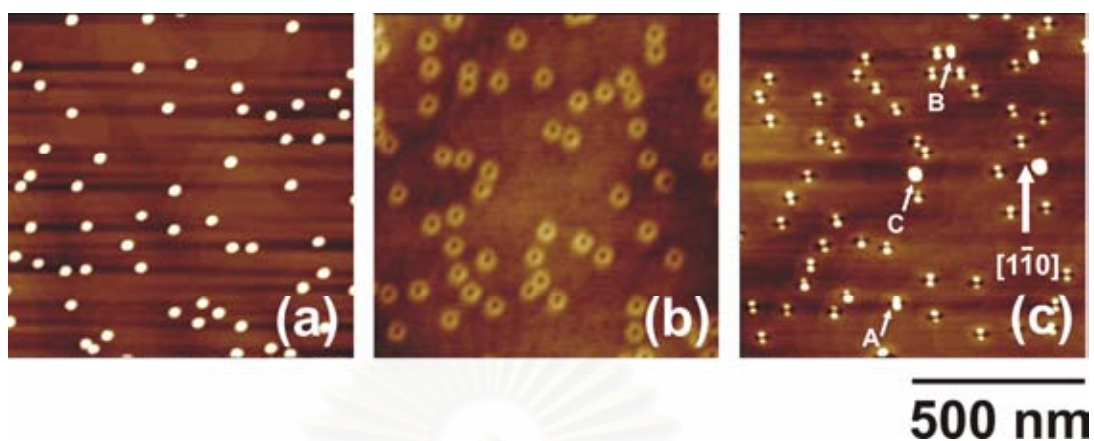


Figure 6.2 AFM images of (a) as-grown QDs, (b) QRs and (c) DQDs with the regrowth thickness of 0.6 ML, grown under  $\text{As}_2$  overpressure in gas-source MBE. In case of DQDs sample (c), at point A where initial merging starts, at point B where a DQD is merging into a single dot, and at point C where a completely merged QD is obtained.

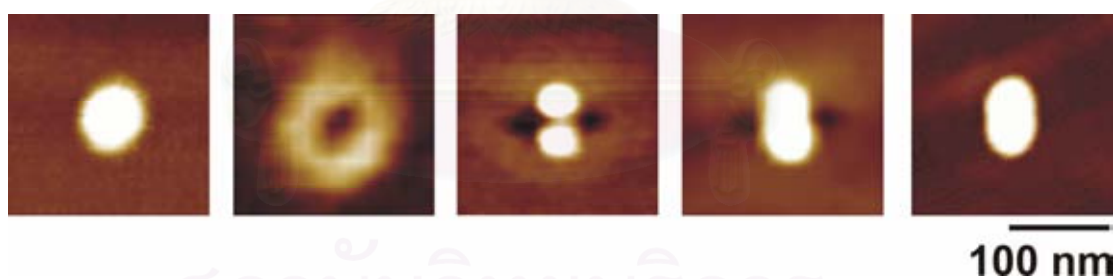


Figure 6.3 Close-up AFM images of (a) an as-grown QD, (b) QR, (c) DQD, (d) initial merging of a DQD and (e) merging into single dot.



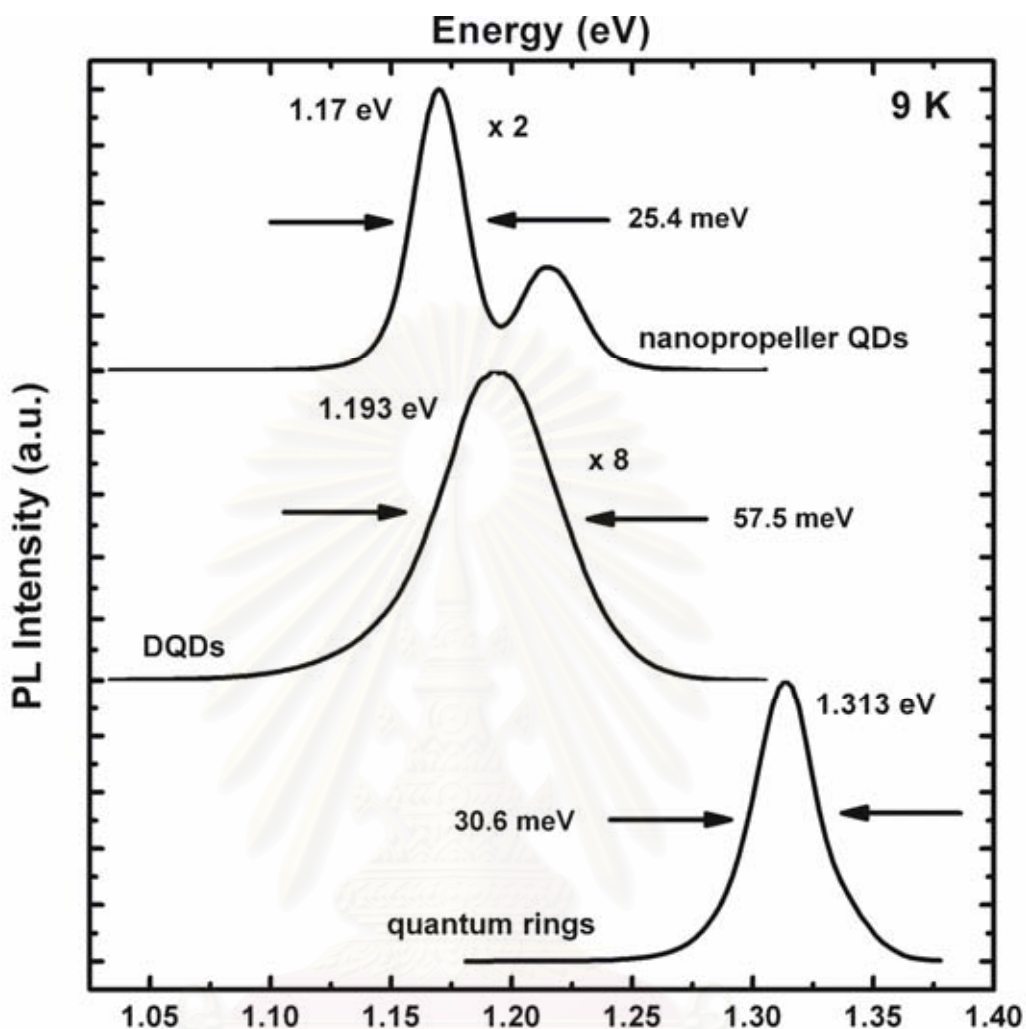


Figure 6.4 Photoluminescence spectra of nanopropeller QDs by solid-source MBE and QRs, DQDs by gas-source MBE at 9 K.

In conclusion, the Arsenic species are the crucial parameter to form different shapes of lateral QDMs in the partial-capping-and-regrowth process. Under  $\text{As}_4$ , the migration length of In adatoms is longer and anisotropic, leading to the formation of elongated camel-like nanostructures and nanopropellers with 10-12 QDs along  $\langle 1\bar{1}0 \rangle$  after partial capping and regrowth, respectively. On the other hand, under  $\text{As}_2$ , the migration length of In adatom is shorter than under  $\text{As}_4$ . The nanostructures grown under  $\text{As}_2$  are less anisotropic than under  $\text{As}_4$ , resulting in QRs after partial capping. The surface migration of In adatoms, however, is anisotropic, leading to higher In concentrations on the two regions of the QR in the  $\langle 1\bar{1}0 \rangle$  direction. With



redeposition of InAs, QDs are formed on these two regions, resulting in a DQD. Therefore, with the partial capping and regrowth technique, As<sub>2</sub> and As<sub>4</sub> result in very different (Ga)InAs nanostructures.



สถาบันวิทยบริการ  
จุฬาลงกรณ์มหาวิทยาลัย

## CHAPTER VII

### CONCLUSIONS

This research work presents a fabrication process to realize the nanostructures such as quantum dots (QDs) and quantum dot molecules (QDMs). Especially, this work emphasizes to use the partial-capping-and-regrowth technique to grow different nanostructures by molecular beam epitaxy (MBE).

This experiment starts with the investigation of the growth parameters and the structural and optical properties of InAs QDMs grown by solid-source MBE. In the first process, self-assembled InAs QDs are grown on a flat GaAs surface using standard MBE procedure. Randomly distributed QDs are obtained. Then, we make use of partial capping over the QDs to produce an anisotropic strain field. The strain field modifies the shape of QDs into nanohole templates for the regrowth of QDs. This nanohole template looks like a camel structure and tends to be aligned along the  $\langle 1\bar{1}0 \rangle$  crystallographic direction. At a regrowth thickness of 0.6 ML, QDs are grown on the nanohole templates, resulting in propeller-like shape QDs. This step has improved dot uniformity leading to narrow PL spectra. With further deposition of InAs QDs, QDMs are formed. The shoulder span of the nanoholes is a key parameter in controlling the number of dots per molecule. At a capping temperature of 470°C, there are 10-12 dots per molecule. QDMs with 4-5 dots per molecule are achieved when the short propeller blades are prepared at a capping temperature of 430°C.

By repeating this partial-capping-and-regrowth process several cycles, aligned QDs and QDMs can be formed. In our specific growth condition, 7 cycles of thin-capping-and-regrowth provides the best condition for QD alignment. We attribute this optimum condition to the pronounced strain field at the center of the underlying nanostructure template. When the number of process cycles exceeds a critical value, random distribution of QDs again results, albeit with a higher dot density comparing to the initial QD layer. We also demonstrate that aligned QDMs can be obtained when aligned QDs are used as templates.

Meanwhile, using partial-capping-and-regrowth technique grown by gas-source MBE, self-assembled InAs lateral DQDs have been achieved under As<sub>2</sub> overpressure. A Gaussian distribution fits dot height histograms from AFM images. The temperature dependence of PL is investigated. The variation of the photon energy with temperature is tentatively attributed to size variation of QDs within the DQDs. Temperature-dependent PL intensities indicate the existence of potential fluctuation due to QD size fluctuation and localized states in the wetting layer.

The different nanostructures between using solid-source MBE and gas-source MBE are discussed. The arsenic species is a crucial parameter to form different shapes of lateral QDMs in the partial-capping-and-regrowth process. Under As<sub>4</sub>, the migration length of In adatoms is longer and anisotropic, leading to the formation of elongated camel-like nanostructures and nanopropellers with 10-12 QDs along  $\langle 1\bar{1}0 \rangle$  after partial capping and regrowth, respectively. On the other hand, under As<sub>2</sub>, the migration length of In adatom is shorter than under As<sub>4</sub>, and the nanostructures grown under As<sub>2</sub> are less anisotropic than under As<sub>4</sub>, resulting in QRs after partial capping. The surface migration of In adatoms, however, is anisotropic, leading to higher In concentrations on the two regions of the QR in the  $\langle 1\bar{1}0 \rangle$  direction. With redeposition of InAs, QDs are formed on these two regions, resulting in a DQD. Therefore, with the partial capping and regrowth technique, As<sub>2</sub> and As<sub>4</sub> result in very different (Ga)InAs nanostructures and QDMs.

The different nanostructures grown by this self-assembly technique using partial-capping-and-regrowth would be useful in various nanoelectronic and nanophotonic applications, such as quantum computing, single electron devices, quantum dot lasers and detectors, and quantum dot solar cells.

## REFERENCES

- Akiyama, Y., and Sakaki, H. 2006. Formation of self-assembled InGaAs quantum dot arrays aligned along quasiperiodic multiatomic steps on vicinal 111B GaAs. Applied Physics Letters 89: 183108.
- Arakawa, Y., and Sakaki, H., 1982. Multi dimensional quantum well laser and temperature dependence of its threshold current. Applied Physics Letters 40:939-941.
- Austing, D.G., Honda, T., Muraki, K., Tokura, Y., and Tarucha, S. 1998. Quantum dot molecules. Physica B 249-251: 206-209.
- Barabási, A.-L. 1997. Self-assembled island formation in heteroepitaxial growth. Applied Physics Letters 70: 2565-2567.
- Bayer, M., Orther, G., Forchel, A., Lyanda-Geller, Y.B., Reinecke, T.L., Hawrylak, P., Fafard, S., and Wasilewski, Z.R. 2003. Fine structure of excitons in InAs/GaAs coupled quantum dots: A sensitive test of electronic coupling. Physical Review Letters 90: 086404.
- Beirne, G. J., Hermannstadter, C., Wang, L., Rastelli, A., Schmidt, O.G., and Michler, P. 2006. Quantum Light Emission of Two Lateral Tunnel-Coupled InGaAs/GaAs Quantum Dots Controlled by a Tunable Static Electric Field. Physical Review Letters 96: 137401.
- Bimberg, D., Grundmann, M., and Ledentsov, N. N. 1999. Quantum dot heterostructures. Chichester: Wiley.
- Chen, Y., and Washburn, J. 1996. Structural Transition in Large-Lattice-Mismatch Heteroepitaxy. Physical Review Letters 77: 4046-4049.
- Craig, J., Taylor, J.M., Lester, E.A., Marcus, C.M., Hanson, M.P., and Gossad, A.C. 2004. Tunable nonlocal spin control in a coupled-quantum dot system. Science 304: 565-567.
- Cullis, A.G., Norris, D.J., Walther, T., Migliorato, M.A., and Hopkinson, M. 2002. Stranski-Krastanow transition and epitaxial island growth. Physical Review B 66: 081305.

- Daruka, I., and Barabási, A. L. 1997. Dislocation-free island formation in heteroepitaxial growth: a study at equilibrium. Physical Review Letters 79: 3708-3711.
- Davies, J. H. 1998. The Physics of low-dimensional semiconductors: An introduction. New York: Cambridge University Press.
- Dobbs, H. T., et al. 1997. Mean-field theory of quantum dot formation. Physical Review Letters 79: 897-900.
- Fitting, L., Ware, M.E., Haywood, J.R., Walter, J.H., and Nemanich, R.J. 2005. Self-organized nanoscale Ge dots and dashes on SiGe/Si superlattices. Journal of Applied Physics 98: 024317.
- Granados, D., García, J.M., Ben, T., and Molina, S.I. 2003. In(Ga)As self-assembled quantum ring formation by molecular beam epitaxy. Applied Physics Letters 82: 2401-2403.
- Grundmann, M. 2000. The present status of quantum dot laser. Physica E: 5 167-184.
- Grundmann, M. 2002. Nano-optoelectronics: Concepts, physics and devices. Berlin: Springer-Verlag.
- Hatano, T., Stopa, M., and Tarucha, S. 2005. Single-electron delocalization in hybrid vertical-lateral coupled quantum dots. Science 309: 268-271.
- Herman, M. A. and Sitter, H. 1989. Molecular beam epitaxy fundamentals and current status. Berlin: Springer-Verlag.
- Houzay, F., Guilie, C., Moison, J.M., Henoc, P., and Barthe, F. 1987. First stages of the MBE growth of InAs on (001) GaAs. Journal of Crystal Growth 81: 67-72.
- Jacobi, K., 2003. Review: Atomic structure of InAs quantum dots on GaAs. Progress in Surface Science 71: 185-215.
- Jaskolski, W., Zielinski, M., and Bryant, G.W. 2003. Electronic properties of quantum-dot molecules. Physica E 17: 40-41.
- Jesson, D. E., et al. 1998. Self-limiting growth of strained faceted islands. Physical Review Letters 80: 5156-5159.
- Jin, G., Liu, J.L., and Wang K.L. 2000. Regimented placement of self-assembled Ge dots on selectively grown Si mesas. Applied Physics Letters 76: 3591-3593.



- Joyce, P. B., Krzyzewski, T. J., Bell, G. R., and Jones, T. S. 2000. Effect of growth rate on the size, composition, and optical properties of InAs/GaAs quantum dots grown by molecular-beam epitaxy. Physical Review B 62: 10891-10895.
- Joyce, P. B., Krzyzewski, T. J., Bell, G. R., and Jones, T. S. 2001. Surface morphology evolution during the overgrowth of large InAs-GaAs quantum dots. Applied Physics Letters 79: 3615-3617.
- Joyce, P.B., Krzyzewski, T.J., Steans, P.H., Bell, G.R., Neave, J.H., and Jones, T.S. 2001. Shape and surface morphology changes during the initial stages of encapsulation of InAs/GaAs quantum dots. Surface Science 492: 345-353.
- Kamiya, I., Tanaka, I., and Sakaki, H. 1998. Optical properties of near surface InAs quantum dots and their formation processes. Physica E 2: 637-642.
- Kiravittaya, S. 2002. Homogeneity improvement of InAs/GaAs self-assembled quantum dots grown by molecular beam epitaxy. Ph.D.'s Thesis. Department of Electrical Engineering, Faculty of Engineering, Chulalongkorn University.
- Kiravittaya, S., Songmuanga, R., Jin-Phillipp, N.Y., Panyakeow, S., and Schmidt, O.G. 2003. Self-assembled nanoholes and lateral QD bi-molecules by molecular beam epitaxy and atomically precise in situ etching. Journal of Crystal Growth 251: 258-263.
- Kiravittaya, S., Heidemeyer, H., and Schmidt, O.G. 2005. Lateral quantum-dot replication in three-dimensional quantum-dot crystal. Applied Physic Letters 86: 263113.
- Kitamura, M., Nishioka, M., Oshinowo, J., Arakawa, Y. 1995. in situ fabrication of self-aligned InGaAs quantum dots on GaAs multiatomic steps by metalorganic chemical vapor deposition. Applied Physics Letters 66: 3663-3665.
- Lambkin, J.D., Considine, L., Walsh, S., O'Connor, G.M., McDonagh, C.J., and Glynn, T.J. 1994. Temperature dependence of the photoluminescence intensity of ordered and disordered  $\text{In}_{0.48}\text{Ga}_{0.52}\text{P}$ . Applied Physics Letters 65: 73-75.

- Ledentsov, N. N., et al. 1996. Direct formation of vertically coupled quantum dots in Stranski-Krastanow growth. Physical Review B 54: 8743-8750.
- Lee, J.-S., Isshiki, H., Sugano, T., Aoyagi, Y. 1998. Surface structure control of GaAs (1 1 1)A vicinal substrates by metal-organic vapor-phase epitaxy. Journal of Crystal Growth 183: 43-48.
- Lee, H. S., Lee, K.H., Park, H.L., Kim, T. W., and Kim, Y.-H. 2005. Effect of thermal annealing on the interband transitions and activation energies of CdTe/ZnTe quantum dots. Journal of Applied Physics 98: 023702.
- Lee, J. H., Wang, Zh. M., Strom, N.W., Mazur, Y.I., and Salamo, G. J. 2006. InGaAs quantum dot molecules around self-assembled GaAs nanomound templates. Applied Physics Letters 89: 202101.
- Lent, C.S., Tougaw, P.D., and Porod, W. 1993. Bistable saturation in coupled quantum dots for quantum cellular automata. Applied Physics Letters 62: 714-716.
- Leonard, D., Krishnamurthy, M., Reaves, C.M., Denbaars, S.P., and Petroff, P.M. 1993. Direct formation of quantum-sized dots from uniform coherent islands of InGaAs on GaAs surfaces. Applied Physics Letters 63: 3203-3205.
- Lewis, B.F. , Lee, T.C., Grunthaner, F.J., Madhukar, A., Fernandez, R., and Maserjian, J. 1984. RHEED oscillation studies of MBE growth kinetics and lattice mismatch strain-induced effects during InGaAs growth on GaAs(100). Journal of Vacuum Science and Technology B 2: 419-421.
- Li, S. S., Xia, J. B., Liu, J. L., Yang, F. H., Niu, Z.C., Feng, S.L., and Zheng H.Z. 2001. InAs/GaAs single-electron quantum dot qubit. Journal of Applied Physics 90: 6151-6155.
- Li, X., Wu, Y., Steel, D., Gammon, D., Stievater, T. H., Katzer, D. S., Park, D., Piermarocchi, C., and Sham, L. J. 2003. An All-Optical Quantum Gate in a Semiconductor Quantum Dot. Science 301:809-811.
- Lippen, T. v., Notzel, R., Hamhuis, G.J., and Wolter J.H. 2004. Self-organized lattice of ordered quantum dot molecules. Applied Physics Letters 85: 118-120.

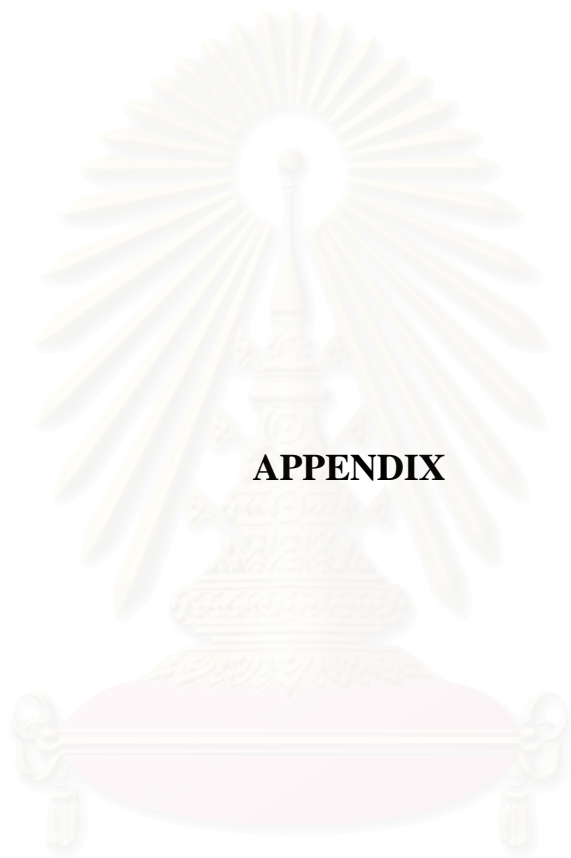
- Lippen, T. v., Notzel, R., Hamhuis, G.J., and Wolter J.H. 2005. Ordered quantum dot molecules and single quantum dots formed by self-organized anisotropic strain engineering. Journal of Applied Physics 97: 044301.
- Madhukar, A., Xie, Q., Chen, P., and Koknar, A. 1994. Nature of strained InAs three-dimensional island formation and distribution on GaAs(100). Applied Physics Letters 77: 2727-2729.
- Mano, T., Notzel, R., Hamhuis, G.J., Eijkemans, T.J., and Wolter, J.H. 2002. Formation of InAs quantum dot arrays on GaAs (100) by self-organized anisotropic strain engineering of a (In,Ga)As superlattice template. Applied Physics Letters 81: 1705-1707.
- Masumoto, Y., and Takagahara, T., 2002. Semiconductor quantum dots. Berlin: Springer-Verlag.
- Medeiros-Ribeiro, G., Maltez, R.L., Bernussi, A.A., Ugarte, D., and Carvalho, W. Jr. 2001. Seeding of InP islands on InAs quantum dot templates. Journal of Applied Physics 89: 6548-6550.
- Mi, Z., and Bhattacharya, P. 2005. Molecular-beam epitaxial growth and characteristics of highly uniform InAs/GaAs quantum dot layers. Journal of Applied Physics 98: 02351.
- Miao, Z.L., Zhang, Y.W., Chua, S.J., Chye, Y.H., Chen, P., and Tripathy, S. 2005. Optical properties of InAs/ GaAs surface quantum dots. Applied Physics Letters 86: 031914.
- Nakata, Y., Sugiyama, Y., Futatsugi, T., Yokoyama, Y. 1997. Self-assembled structures of closely stacked InAs islands grown on GaAs by molecular beam epitaxy. Journal of Crystal Growth 175-176: 713-719.
- Nishikawa, A., Hong, Y.G., and Tu, C.W. 2004. Temperature dependence of optical properties of  $\text{Ga}_{0.3}\text{In}_{0.7}\text{N}_x\text{As}_{1-x}$  quantum dots grown on GaAs (001). Journal of Vacuum Science and Technology B 22: 1515-1517.
- Oulton, R., Tartakovskii, A.I., Ebbens, A., Finley, J.J., Mowbray, D.J., Skolnick, M.S., and Hopkinson, M. 2005. Anomalous Stark shifts in single vertically coupled pairs of InGaAs quantum dots. Physica E 26: 302-307.

- Offermans, P. , Koenraad, P.M., Wolter, J.H., Granados, D., García, J.M., Fomin, V.M., Gladilin, V.N., and Devreese, J. T. 2005. Atomic-scale structure of self-assembled In(Ga)As quantum rings in GaAs Applied Physics Letters 87: 131902.
- Paskov, P.P., Holtz, P.O., Monemar, B., Garcia, J.M., Schoenfeld, W.V., and Petroff, P.M. 2000. Photoluminescence up-conversion in InAs/GaAs self-assembled quantum dots. Applied Physics Letters 77: 812-814.
- Pfannkuche, D., Blick, R.H., Haug, R.J., Klitzing, K.v., and Eberl, K. 1998. Coupled quantum dots: manifestation of an artificial molecule. Superlattices and Microstructures 23: 1255-1264.
- Pistol, M.-E., Carlsson, N., Persson, C., Seifert, W., and Samuelson, L. 1995. Observation of strain effects in semiconductor dots depending on cap layer thickness. Applied Physics Letters 67: 1438-1440.
- Polimeni, A., Patane, A., Henini, M., Eaves, L., and Main, P.C. 1999. Temperature dependence of the optical properties of InAs/Al<sub>y</sub>Ga<sub>1-y</sub>As self-organized quantum dots. Physical Review B 59: 5064-5068.
- Reinhardt, F., Jonsson, J., Zorn, M., Richter, W., Ploska, K., Rumberg, J., and Kurpas, P. 1994. Monolayer growth oscillations and surface structure of GaAs(001) during metalorganic vapor phase epitaxy growth. Journal of Vacuum Science and Technology B 12: 2541-2546.
- Schaffer, W.J. 1983. Nucleation and strain relaxation at the InAs/GaAs(100) heterojunction. Journal of Vacuum Science and Technology B 1: 688-695.
- Schmidt, O.G., Kienzle, O., Hao, Y., Eberl, K., and Ernst, F. 1999. Modified Stranski–Krastanov growth in stacked layers of self-assembled islands. Applied Physics Letters 74: 1272-1274.
- Seifert, W., Carlsson, N., Miller, M., Pistol, M-E., Samuelson, L., and Wallenberg, L. R. 1996. In-situ growth of quantum dot structures by the stranski-Krastranow growth mode. Progress of Crystal Growth and Characterization 33: 423-471.
- Seifert, W., et al. 1999. Continuous and discontinuous metal-organic vapour phase epitaxy of coherent self-assembled islands effects on size homogeneity. Journal of Crystal Growth 197: 19-24.

- Shchukin, V.A., Ledentsov, N. N., Kop'ev, P. S., and Bimberg, D. 1995. Spontaneous ordering of arrays of coherent strained islands. Physical Review Letters 75: 2968-2971.
- Shchukin, V. A., and Bimberg, D. 1999. Spontaneous ordering of nanostructures on crystal surfaces. Reviews of Modern Physics 71: 1125-1171.
- Shchukin, V. A., et al. 2001. Spontaneous formation of nanostructures on crystal surfaces. Physica E 9: 140-148.
- Songmuang, R. 2003. Study on growth and in-situ processing of InAs self-organized quantum dots for long wavelength applications. Ph.D.'s Thesis. Department of Electrical Engineering, Faculty of Engineering, Chulalongkorn University.
- Songmuang, R., Kiravittaya, S., and Schmidt, O.G. 2003. Shape evolution of InAs quantum dots during overgrowth. Journal of Crystal Growth 249: 416-421.
- Songmuang, R., Kiravittaya, S., and Schmidt, O.G. 2003. Formation of lateral quantum dot molecules around self-assembled nanoholes. Applied Physics Letters 82: 2892-2894.
- Srolovitz, D. J., 1989. On the stability of surfaces of stressed solids. Acta Metallurgica 37: 621-625.
- Sugawara, M. 1999. Self-assembled InGaAs/GaAs quantum dots: Semiconductors and semimetals. San Diego: Academic Press.
- Timler, J., and Lent, C. S. 2002. Power gain and dissipation in quantum-dot cellular automata. Journal of Applied Physics 91: 823-831.
- Tu, K.-N., Mayer, J.W., and Feldman, C. 1992. Electronic Thin Film Science. Chapter 7, Mcmillan Publishing Company.
- Varshni, Y.P. 1967. Temperature dependence of the energy gap in semiconductors. Physica 34: 149-154.
- Voigtlander, B. 2001. Fundamental processes in Si/Si and Ge/Si epitaxy studied by scanning tunneling microscopy during growth. Surface Science Reports 43: 127-254.
- Wang, L.G., Kratzer, P., Moll, N., and Scheffler, M. 2001. Size, shape, and stability of InAs quantum dots on the GaAs (001) substrate. Physical Review B 62: 1897-1904.



- Wang, L.G., et al. 2001. Island dissolution during capping layer growth interruption. Applied Physics A 73: 161-165.
- Wang, Zh.M., Churchill, H., George, C.E., and Salamo, G.J. 2004. High anisotropy of lateral alignment in multilayered (In,Ga)As/GaAs (100) quantum dots structures. Journal of Applied Physics 96: 6908-6911
- Woggor, U. 1997. Optical Properties of Semiconductor Quantum Dots. Berlin: Springer-Verlag.
- Xie, Q., Chen, P., and Madhukar, A. 1994. InAs island-induced strain driven adatoms migration during GaAs overlayer growth. Applied Physic Letters 65: 2051-2053.
- Xie, Q., Madhukar, A., Chen. P., Kobayashi, N.P. 1995. Vertically self-organized InAs quantum box islands on GaAs(100). Physical Review Letters 75: 2542-2545.
- Yamauchi, S., Komori, K., Morohashi, I., Goshima, K., and Sugaya, T. 2005. Observation of interdot correlation in single pair of electromagnetically coupled quantum dots. Applied Physics Letters 87: 182103.
- Zhan, H.H., Notzel, R., Hamhuis, G.J., Eijkemans, T.J., and Wolter, J.H. 2003. Self-assembled InAs quantum dots formed by molecular beam epitaxy at low temperature and postgrowth annealing. Journal of Applied Physics 93: 5953-5958.



**APPENDIX**

สถาบันวิทยบริการ  
จุฬาลงกรณ์มหาวิทยาลัย

## List of Publications

### 1. International Publications

1. **Suwaree Suraprapapich**; Supachok Thainoi; Chanin Laliew (Wissawinthanon); Songphol Kanjanachuchai; and Somsak Panyakeow. 2005. Self-Assembled Indium-Arsenide Elongated Nanostructure Grown by Molecular Beam Epitaxy. International Journal of Nanoscience 4: 253-259.
2. **Suwaree Suraprapapich**; Songphol Kanjanachuchai; Supachok Thainoi; and Somsak Panyakeow. 2005. Ordered Quantum Dots Formation on Engineered Template by Molecular Beam Epitaxy. Microelectronic Engineering 78-79: 349-352.
3. **Suwaree Suraprapapich**; Supachok Thainoi; Songphol Kanjanachuchai; and Somsak Panyakeow. 2005. Self-Assembled Quantum Dot Molecules by Molecular-Beam Epitaxy. Journal of Vacuum Science and Technology B 23: 1217-1220.
4. **Suwaree Suraprapapich**; Supachok Thainoi; Songphol Kanjanachuchai; and Somsak Panyakeow. 2006. Regrowth of Self-Assembled InAs Quantum Dots on Nanohole and Stripe Templates. Journal of Microlithography, Microfabrication and Microsystems 5: 011008-1 - 011008-5.
5. **Suwaree Suraprapapich**; Songphol Kanjanachuchai; Supachok Thainoi; and Somsak Panyakeow. 2006. Self-Assembled Lateral InAs Quantum Dot Molecules: Dot Ensemble Control and Polarization-Dependent Photoluminescence. Journal of Microelectronics Engineering 83: 1526-1529.
6. **Suwaree Suraprapapich**; Songphol Kanjanachuchai; Supachok Thainoi; and Somsak Panyakeow. 2006. Self-Assembled InAs Lateral Quantum Dot Molecules Growth on (001) GaAs by Thin-Capping-and-Regrowth MBE Technique. Journal of Solid State Phenomena 121-123: 395-399.

7. **Suwaree Suraprapapich**; Supachok Thainoi; Songphol Kanjanachuchai; and Somsak Panyakeow. 2006. Thin-Capping-and-Regrowth MBE Technique for Quantum Dots and Quantum Dot Molecules. Journal of Vacuum Science and Technology B 24: 1665-1667.
8. **Suwaree Suraprapapich**; Supachok Thainoi; Songphol Kanjanachuchai; and Somsak Panyakeow. 2006. Quantum Dot Integration in Heterostructure Solar Cell. Journal of Solar Energy Materials and Solar Cells 90: 2968-2974.
9. Supachok Thainoi; **Suwaree Suraprapapich**; Songphol Kanjanachuchai; and Somsak Panyakeow. 2006. n-GaAlAs on p-GaAs Heterostructure Solar Cells Grown by Molecular Beam Epitaxy. Journal of Solar Energy Materials and Solar Cells 90: 2989-2994.
10. **Suwaree Suraprapapich**; Y.M. Shen; V.A. Odnoblyudov; Y. Fainman; S. Panyakeow and C.W. Tu. 2007. Self-Assembled Lateral Bi-Quantum-Dot Molecule Formation by Gas-Source Molecular Beam Epitaxy. Journal of Crystal Growth. 301-302: 735-739.
11. Napat Siripitakchai; **Suwaree Suraprapapich**; Supachok Thainoi; Songphol Kanjanachuchai; and Somsak Panyakeow. 2007. Evolution of Self-Assembled Lateral Quantum Dot Molecules. Journal of Crystal Growth. 301-302: 812-816.
12. **Suwaree Suraprapapich**; S. Panyakeow; and C.W. Tu. 2007 The effect of Arsenic species on the formation of (Ga)InAs nanostructures after partial-capping-and-regrowth. Applied Physics Letters. *Accepted under Revision*.

## 2. National publications

1. **Suwaree Suraprapapich**; Supachok Thainoi; Songphol Kanjanachuchai; and Somsak Panyakeow. 2005. Quantum Dot Molecules for Quantum Computing. Khonkaen University Engineering Journal.
2. Napat Siripitakchai; **Suwaree Suraprapapich**; Supachok Thainoi; Songphol Kanjanachuchai and Somsak Panyakeow. 2005. Quantum Dot Molecules for Quantum Cellular Automata: Future Quantum Computer. ECTI, Transactions on Electrical Eng., Electronics, and Communications.

### 3. International Conferences

1. **Suwaree Suraprapapich**; Supachok Thainoi; Songphol Kanjanachuchai and Somsak Panyakeow. 2004. Quantum Dot integration in Heterostructure Solar Cells. Proceedings of the 14th International Photovoltaic Science and Engineering Conference.
2. Supachok Thainoi; **Suwaree Suraprapapich**; Montri Sawadsaringkarn; and Somsak Panyakeow. 2004. n-GaAlAs on p-GaAs Heterostructure Solar Cells Grown by Molecular Beam Epitaxy. Proceedings of the 14th International Photovoltaic Science and Engineering Conference.
3. **Suwaree Suraprapapich**; Supachok Thainoi; Songphol Kanjanachuchai; and Somsak Panyakeow. 2005. Quantum Dot Molecules for Photovoltaic Cell Application. Proceedings of the 31st IEEE Photovoltaic Specialists Conference.
4. **Suwaree Suraprapapich**; Sirichai Ruangdet; Supachok Thainoi; Songphol Kanjanachuchai; and Somsak Panyakeow. 2005. Multi-Stacked High Density Quantum Dot Molecules as PV Active Layer. Proceedings of the 15th International Photovoltaic Science and Engineering Conference.

### 4. National Conferences

1. **Suwaree Suraprapapich**; Supachok Thainoi; Montri Sawadsaringkarn; and Somsak Panyakeow. 2003. AlGaAs/GaAs Heterostructure Solar Cells Grown by Molecular Beam Epitaxy. Proceedings of the 26th Electrical Engineering Conference.
2. **Suwaree Suraprapapich**; Songphol Kanjanachuchai; and Somsak Panyakeow. 2004. Quantum Dot Molecules for Quantum Computing. Proceedings of the 27th Electrical Engineering Conference.
3. Teerasak Panyawanichkul; **Suwaree Suraprapapich**; Supachok Thainoi; Songphol Kanjanachuchai; and Somsak Panyakeow. 2004. Effects of InAs Quantum Dots on Electron Mobility in GaAs. Proceedings of the 27th Electrical Engineering Conference.



4. **Suwaree Suraprapapich**; Supachok Thainoi; and Somsak Panyakeow. 2005. Self Assembled Quantum Dot Molecules by Molecular Beam Epitaxy and Potential Applications. Proceedings of the 6th RGJ Conference.
5. Nan Thidar Chit Swe; **Suwaree Suraprapapich**; Supachok Thainoi; Pornchai Changmoang; Chanin Wissawinthanon; and Somsak Panyakeow. 2005. Polarized Photoluminescence of InAs/GaAs Linearly Aligned Quantum Dots. Proceedings of the 28th Electrical Engineering Conference.
6. Naparat Siripitakchai; **Suwaree Suraprapapich**; Supachok Thainoi; Songphol Kanjanachuchai; and Somsak Panyakeow. 2005. Polarized Photoluminescence of Multi-Stacked Lateral Quantum Dot Molecules by Thin-Capping-and-Regrowth MBE Technique. Proceedings of the 28th Electrical Engineering Conference.
7. Teerasak Panyawanichkul; Suwaree Suraprapapich; Supachok Thainoi; Songphol Kanjanachuchai; and Somsak Panyakeow. 2005. Effects of InAs Quantum Dots on Electron Mobility in GaAs. Proceedings of the 28th Electrical Engineering Conference.

## List of Presentations

### 1. International Presentations

#### *Oral presentation*

**Suwaree Suraprapapich**; Supachok Thainoi; Songphol Kanjanachuchai and Somsak Panyakeow. 2004. Quantum Dot integration in Heterostructure Solar Cells. The 14th International Photovoltaic Science and Engineering Conference. Bangkok, Thailand, Jan 26-30 (2004).

#### *Poster presentation*

Supachok Thainoi; **Suwaree Suraprapapich**; Montri Sawadsaringkarn; and Somsak Panyakeow. 2004. n-GaAlAs on p-GaAs Heterostructure Solar Cells Grown by Molecular Beam Epitaxy. The 14th International Photovoltaic Science and Engineering Conference. Bangkok, Thailand, January 26-30 (2004).

#### *Oral presentation*

Suwaree Suraprapapich; Supachok Thainoi; Chanin Laliew (Wissawinthanon); Songphol Kanjanachuchai; and Somsak Panyakeow. 2004. Self-Assembled Indium Arsenide Elongated Nanostructure by Molecular Beam Epitaxy. The 1st Nano-Engineering and Nano-Science Congress, Singapore, July 7-9 (2004).

#### *Poster presentation*

Suwaree Suraprapapich; Songphol Kanjanachuchi; Supachok Thainoi; and Somsak Panyakeow. 2004. Ordered Quantum Dots Formation on Engineered Template by Molecular Beam Epitaxy. Micro- and Nano- Engineering 2004, Rotterdam, The Netherlands, September 19-22 (2004). (**Best Poster Award**)

*Poster presentation*

**Suwaree Suraprapapich;** Supachok Thainoi; Songphol Kanjanachuchai and Somsak Panyakeow. 2005. Thin-Capping-and-Regrowth MBE Technique for Quantum Dots and Quantum Dot Molecules. The 23rd North America Molecular Beam Epitaxy, Santa Barbara, California, USA., September 11-14 (2005).

*Oral presentation*

**Suwaree Suraprapapich;** Y.M. Shen; Y. Fainman; S. Panyakeow and C.W. Tu. 2006. The Effects of Rapid Thermal Annealing on Bi-Quantum Dot Molecules Grown by Gas-Source Molecular Beam Epitaxy. Electronic Material Conference (EMC) 2006, Pennsylvania State University, Pennsylvania, U.S.A., June 28-30 (2006).



สถาบันวิทยบริการ  
จุฬาลงกรณ์มหาวิทยาลัย

## 2. National Presentations

### *Oral presentation*

**Suwaree Suraprapapich;** Supachok Thainoi; Montri Sawadsaringkarn; and Somsak Panyakeow. 2003. AlGaAs/GaAs Heterostructure Solar Cells Grown by Molecular Beam Epitaxy. The 26th Electrical Engineering Conference. the Goldensand Hotel, Chaum, Thailand, November 6-7 (2003).

### *Oral presentation*

**Suwaree Suraprapapich;** Songphol Kanjanachuchai; and Somsak Panyakeow. 2004. Quantum Dot Molecules for Quantum Computing. The 27th Electrical Engineering Conference, The Sofitel Hotel, Khonkaen, November 11-12 (2004). (*Best Paper Award*)

### *Oral presentation*

**Suwaree Suraprapapich;** Supachok Thainoi; and Somsak Panyakeow. 2005. Self Assembled Quantum Dot Molecules by Molecular Beam Epitaxy and Potential Applications. The 6th RGJ Conference, Chomtien Palm Resort, Pattaya Thailand, April 28-30 (2005).

### *Oral presentation*

**Suwaree Suraprapapich** and Somsak Panyakeow. 2006. The Formation of Self-Assembled Quantum Dot Molecules by Molecular Beam Epitaxy. The 6<sup>th</sup> National Symposium on Graduate Research, Chulalongkorn University, Bangkok, Thailand, October 13-14 (2006). (*Best Dissertation Award*)

## Miscellaneous

### 1. International Presentations

#### *Oral presentation*

Somsak Panyakeow and **Suwaree Suraprapapich**. 2004. Self-Assembled Quantum Dot Molecules by Molecular Beam Epitaxy. The 22nd North American Conference on Molecular Beam Epitaxy, Banff, Alberta, Canada, October 10-14 (2004).

#### *Oral presentation*

**Suwaree Suraprapapich**; Supachok Thainoi; Songphol Kanjanachuchai; and Somsak Panyakeow. 2005. Quantum Dot Molecules for Photovoltaic Cell Application. The 31st IEEE Photovoltaic Specialists Conference, Orlando, Florida, U.S.A., January 3-7 (2005).

#### *Poster presentation*

**Suwaree Suraprapapich**; Sirichai Ruangdet; Teerasak Panyawanichkul; Supachok Thainoi; Songphol Kanjanachuchai; and Somsak Panyakeow. 2005. Multi-Stacked Lateral Quantum Dot Molecules for Photovoltaic Applications. The 20th European Photovoltaic Solar Energy Conference and Exhibition, Barcelona Spain, June 6-10 (2005).

#### *Oral presentation*

**Suwaree Suraprapapich**; Supachok Thainoi; Songphol Kanjanachuchai; and Somsak Panyakeow. 2005. Self-Assembled InAs Lateral Quantum Dot Molecules Growth on (001) GaAs by Thin-Capping-and-Regrowth MBE Technique. China NANO 2005, Beijing, China, June 9-11 (2005).



*Poster presentation*

**Suwaree Suraprapapich**; Songphol Kanjanachuchai; Supachok Thainoi and Somsak Panyakeow. Self-Assembled Lateral InAs Quantum Dot Molecules: Dot Ensemble Control and Polarization-Dependent Photoluminescence. The 31st International Conference on Micro and Nano-Engineering 2005, Vienna, Austria, September 19-22 (2005).

*Oral presentation*

Suwaree Suraprapapich; Sirichai Ruangdet; Supachok Thainoi; Songphol Kanjanachuchai; and Somsak Panyakeow. 2005. Multi-Stacked High Density Quantum Dot Molecules as PV Active Layer. The 15th International Photovoltaic Science and Engineering Conference, Shanghai, China, October 10-15 (2005).

*Oral presentation*

Naparat Siripitakchai; **Suwaree Suraprapapich**; and Somsak Panyakeow. 2005. Quantum Dot Molecules for Quantum Computing. The 2nd Field-Wise Seminar on Nanoelectronics and Photonics, Hanoi University, Vietnam, November 14-15 (2005).

*Oral presentation*

**Suwaree Suraprapapich**; Sirichai Ruangdet; Teerasak Panyawanichkul; Supachok Thainoi; Songphol Kanjanachuchai; and Somsak Panyakeow. 2005. Multi-Stacked High Density Quantum Dot Molecules as PV Active Layer. The 2nd Field-Wise Seminar on Nanoelectronics and Photonics, Hanoi University, Vietnam, November 14-15 (2005).

*Oral presentation*

Naparat Siripitakchai; **Suwaree Suraprapapich**; Supachok Thainoi; Songphol Kanjanachuchai; and Somsak Panyakeow. 2006. Evolution of Self-Assembled Lateral Quantum Dot Molecules. International Conference on Molecular Beam Epitaxy (MBE 2006), Tokyo, Japan, September 3-8 (2006).

*Poster presentation*

**Suwaree Suraprapich;** Naparat Siripitakchai; Sirichai Ruangdet; Nuttawut Budsayaplakorn; Wipakorn Jevasuwan; Pornchai Changmuang; Supachok Thainoi; Songphol Kanjanachuchai; Somchai Ratanathammaphan; Montri Sawadsaringkarn; and Somsak Panyakeow. 2006. Self-Assembled Quantum Dot Molecules for Practical Nanostructure Devices: Bottom-Up Approach. The 32nd International Conference on Micro and Nano-Engineering 2005, Barcelona, Spain, September 17-22 (2006).



สถาบันวิทยบริการ  
จุฬาลงกรณ์มหาวิทยาลัย

## VITAE

Suwaree Suraprapapich was born in Khon Kaen, Thailand on March 24, 1981. In June 1998, she entered Kasetsart University and received the Bachelor of Engineering in Electrical Engineering Program with first class honor in March 2002.

She became the Master degree's student of Engineering in Electrical Engineering Program in June 2002 from the Graduate School of Chulalongkorn University and then transferred her study to be a Ph.D. student in June 2003. She was financial supported by Thailand Research Fund (TRF) through the Royal Golden Jubilee (RGJ) Scholarship since 2003.

Between July 2005 and July 2006, she got an opportunity to work as a visiting student in Department of Electrical and Computer Engineering, Jacob School of Engineering, University of California in San Diego, USA. She received a funding from the RGJ Scholarship for half-year and was also supported by Prof. Charles W. Tu for another half-year during work in San Diego, USA.

สถาบันวิทยบริการ  
จุฬาลงกรณ์มหาวิทยาลัย